Doctoral Dissertation

Comprehensive Evaluation Framework for Resist Process Based on Scanning Electron Microscope Image and Quartz Crystal Microbalance Method

JIN YUQING

June 2025

Graduate School of Engineering,

the University of Osaka

Contents

General Introduction

i. Semiconductor industry and challenges in feature size shrinking

There is a famous principle in the semiconductor industry that predicts the pace of technological advancement. It was proposed by Gordon Moore, a co-founder of Intel, and is known as Moore's Law. According to this empirical observation, the number of transistors on a chip doubles approximately every two years. It's not a scientific law like Newton's laws, but an empirical rule that has been pushing industry forward. This prediction has been realized in practice for decades, which is considered an industrial miracle, made possible by the hard work and intelligence of all the people involved in the industry.

A chip with more transistors gives faster response in calculations, making computation quicker and smoother. One example that can easily relate to is the improvement of smartphones. Apple has continued designing their own chips for mobile products, and the number of transistors is shown by the orange line in Fig. 1. The increasing trend of the orange line shows that the number of transistors used in a phone chip is growing in an exponential way, as shown in Fig. 1. At the same time, as plotted in blue line in Fig. 1, the half-pitch (HP), which represents the feature size (also called critical dimension, CD), is shrinking during this process.[1] As these features shrink, more transistors can be packed onto a single chip. In other words, reducing feature sizes enhances the performance and energy efficiency of electronic devices.

The feature size continues to shrink today. Line-and-space (L/S) patterns and contact holes (CH) are the standard resist structures used to assess the current level of manufacturing capability. Several factors contribute to the continued shrinking of feature sizes, including advances in lithography technologies, materials science, manufacturing processes, design and computational tools, as well as massive investment and the momentum driven by Moore's Law.

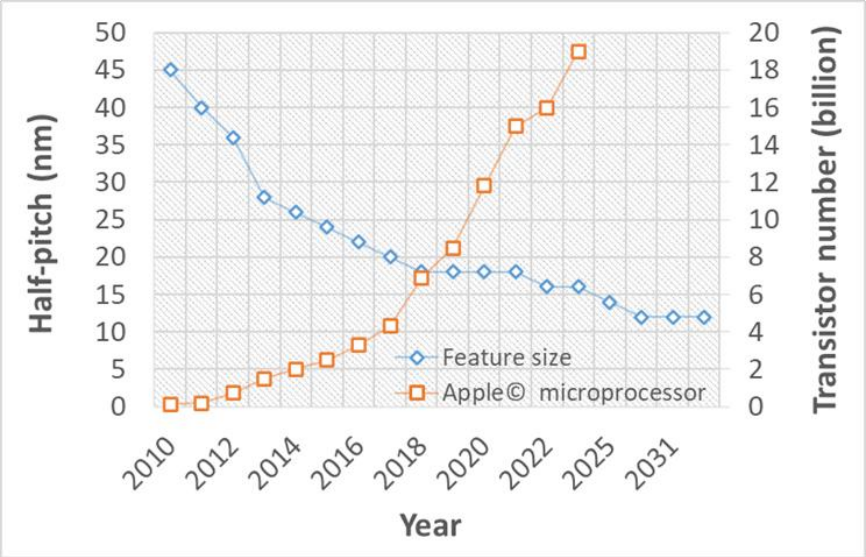

Figure 1 Trends in feature size and Apple's microprocessor products: decreasing feature size (blue) and increasing number of transistors (orange).

The evolution of technologies enables the shrink of the feature sizes. The Rayleigh criterion is a formula used to describe the key parameters involved:

$$\text{Minimum feature size} = \frac{k_1 \cdot \lambda}{NA}, \tag{1}$$

where k_1, NA and λ are process coefficient, numerical aperture of the optics, and the wavelength of light used, respectively. These three parameters can be roughly grouped into two categories: optical factors and non-optical factors.

On the optical side, progress has been significant. The lithography light source evolved from krypton fluoride (KrF, λ = 248 nm) in the 1990s to extreme ultraviolet (EUV, λ = 13.5 nm), which was first adopted in high-volume manufacturing in 2019. The numerical aperture (NA) has also improved, with high-NA EUV (NA = 0.55) moving towards hyper-NA EUV (NA = 0.75) as of last year.

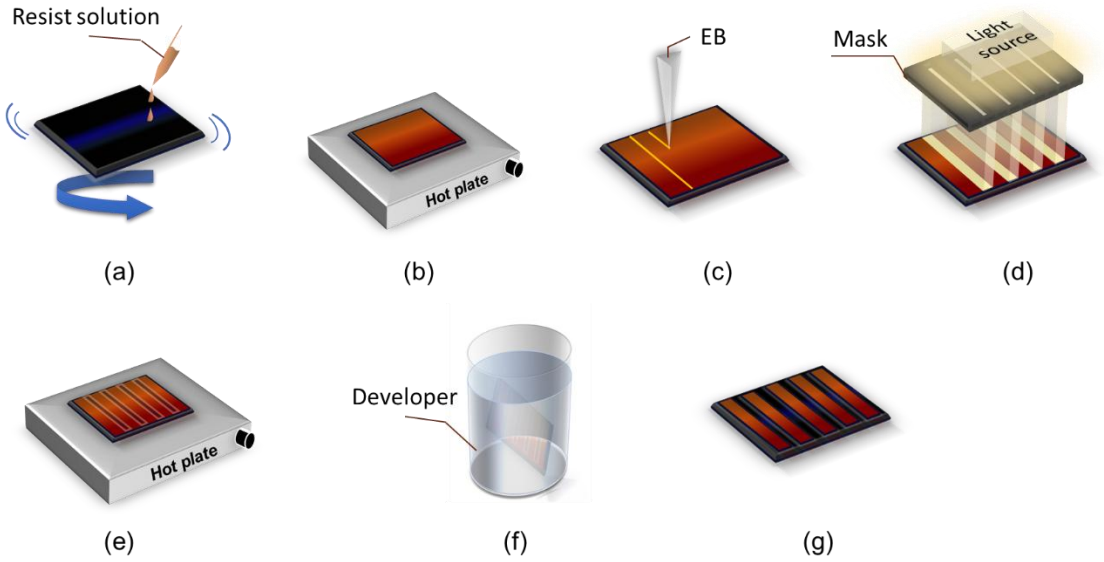

Figure 2 The procedures in a chemically amplified resist pattern fabrication. (a) Spin-coating of resist solution; (b) Prebake/Softbake; (c) EB exposure; (d) Exposed to light source with mask; (e) Post-exposure baking; (f) Development; (g) Line-and-space pattern.

Not only the optical image plays a critical role in lithographic performance, but also the ability of materials and processes to preserve and accurately transfer this information is equally important. On the non-optical side, the process factor k_1 incorporates a range of process innovations, with photoresist systems—comprising resists, developers, and related materials—being a major contributor. For instance, in chemically amplified resist (CAR) systems, pattern formation requires several tightly controlled steps, including spin-coating, prebake, exposure, post-exposure baking (PEB) and development as shown in Fig. 2. Each of these steps is important to the successful transfer of the aerial image into a qualified resist pattern. Moreover, the introduction of EUV lithography presents new challenges.[2,3,4] Even though EUV enables further pattern scaling due to its shorter wavelength, the significantly less photon numbers compared to vacuum ultraviolet (VUV) sources such as ArF excimer lasers introduces additional difficulties in maintaining pattern fidelity.

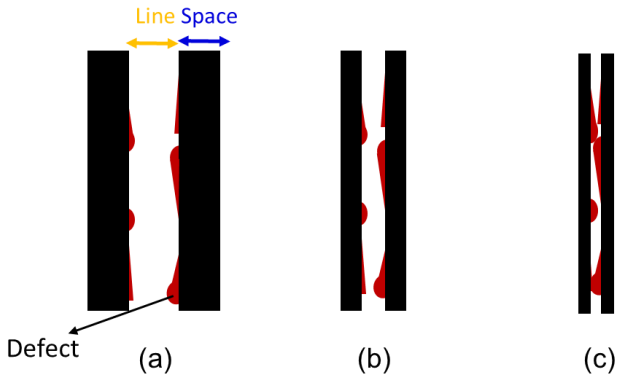

Figure 3 Defects in line/space (L/S) patterns with varying HPs. Red regions highlight defect locations.

In this context, it is important to define what constitutes a "qualified" resist pattern. Patterning performance is primarily evaluated based on three key metrics: resolution, line edge roughness (LER), and sensitivity—collectively referred to as the RLS trade-off.[5] Especially when the feature size decreases, LER becomes more prominent, as illustrated in Fig. 3. The LER observed in a larger HP, shown in Fig. 3(a), can lead to bridging in a smaller HP, as shown in Fig. 3(c), which may further result in circuit disconnection. Ultimately, this can lead to defective products. Previous studies on the resist pattern metrology have reported many factors that can cause LER.[6,7]

To make smaller feature size than possible today, new resists that meet the new need of the EUV light source and the compatible developers are required to meet these three requirements at the same time. It is difficult to satisfy all three RLS at the same time, which opens up space for further discussion and exploration of new resist materials. The fabrication of a resist pattern involves several processes, such as exposure and development, each of which includes many parameters. However, the effects of these steps are often neither directly observable nor easily converted into quantifiable data. Consequently, the traditional process control has relied heavily on empirical methods rather than statistical or data-driven approaches, making the development of new resists time-consuming. To reduce the time and cost of resist exploration, it is essential to analyze the correlation between process parameters and the resulting pattern quality. This involves two key components: (1) the datafication of process

parameters and results, and (2) the development of mathematical models capable of interpreting these correlations.

Emerging artificial intelligence (AI) technologies offer powerful tools for such correlation analysis. Machine learning (ML) techniques—including regression analysis, classification, and deep learning (DL)—have recently been applied successfully in various fields, such as image recognition. This doctoral dissertation aims to establish a framework that applies machine learning methods to the exploration of resist materials and lithography processes, enabling a more efficient and data-driven approach to lithographic process development.

This doctoral dissertation also focuses on the materials and processes involved in resist patterning, with each chapter organized according to specific steps in the lithography process. The machine learning model, and the practical application will be presented in the final chapter. It is worth noting that further parameters might be extracted beyond the scope of this dissertation, as deeper insights into the materials and processes are being discussed. More robust machine learning models are currently being tested to enhance correlation analysis and predictive accuracy.

ii. Chemically amplified resist

Chemically amplified resists (CARs) have been widely used as resists for both EUV and electron beam (EB) lithography. CARs were originally developed for use with KrF excimer lasers, which emit deep ultraviolet (DUV) light at 248 nm, and continue to be utilized with current EUV systems that operate at a wavelength of 13.5 nm. In CARs, insufficient photon energy is compensated for with heat energy.[8] A typical CAR is composed of a photoacid generator (PAG), a base (quencher)[9], and a polymer with side chains partially protected by nonpolar protecting groups such as *tert*-butyloxycarbonyl (*t*-Boc).[8] Upon exposure to a radiation, the acids are generated through the decomposition of a PAG, followed by reaction with the hydrophobic protecting units on the side chain of the polymer. This process is further amplified by post-exposure bake (PEB). Owing to the polarity increase of the polymer, the polymer becomes hydrophilic and thus

dissolvable in an aqueous developer.[10] The resin polymer used in this study was poly(4-hydroxystyrene) (PHS).

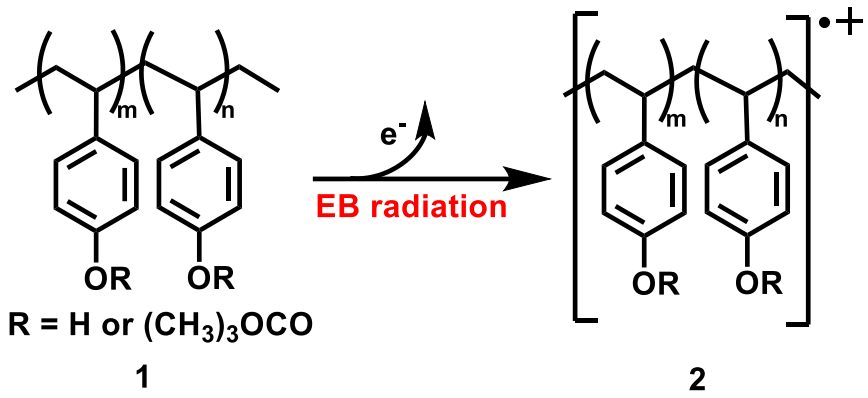

Scheme 1 An electron is ejected from polymer 1 by exposing it to EB radiation. As a product, cation radical 2 is generated.

After spin-coating the resist onto a silicon (Si) substrate and performing pre-exposure baking, the sample is exposed to an EB or other light sources using designed patterns such as L/S patterns with varying HP and exposure doses. As illustrated in Scheme 1, when the resist is exposed to an EB or EUV, primary electrons or EUV photons interact with the polymer, causing the ejection of secondary electrons. These secondary electrons are subsequently thermalized and begin to diffuse within the resist material, triggering further chemical reactions. Additionally, Coulomb forces between the electrons influence their diffusion behavior, which can impact the spatial distribution of the reactions.

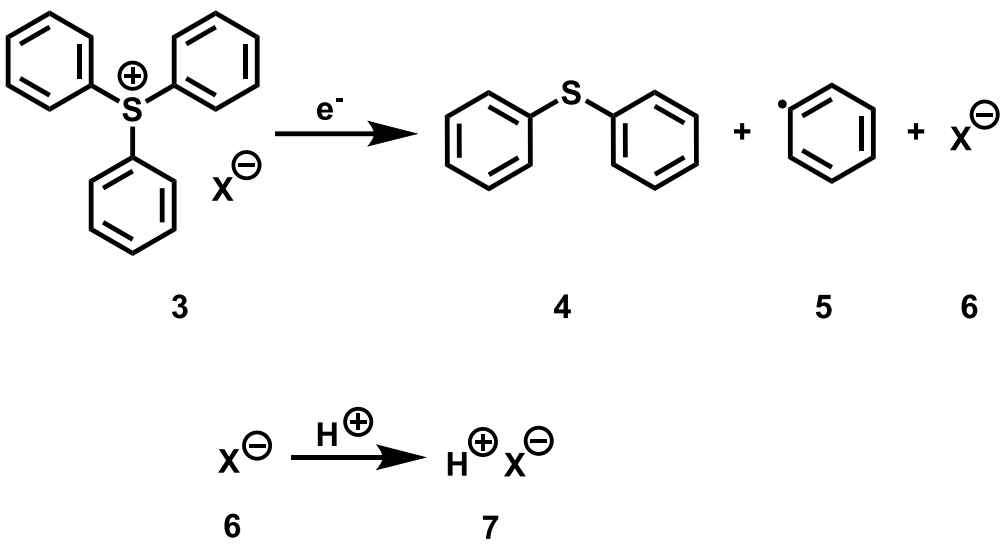

Scheme 2 Decomposition of PAG and generation of acid.

Following electron ejection, the photoacid generator (PAG, substance 3) undergoes decomposition, generating acid species, as illustrated in Scheme 2. During PEB process, the generated acid diffuses in the resist film and catalyzes the deprotection reaction of the polymer side chains.

Patterns are fabricated using CARs, determined by the concentration of protecting units on the side chain of polymer (C_p). The accumulation of the stochastic effects[11] in the formation of patterns finally cause the protected unit fluctuation.[12,13] This is the main factors for the generation of defects such as line edge roughness (LER), on the line-and-space (L/S) pattern which is a typical resist pattern to evaluate the pattern fidelity. On the other hand, the solubility of a polymer in this study was determined by the dissolution threshold (C_{th}). C_p determines whether a polymer is dissolvable (when C_p is smaller than C_{th}) in a hydrophilic developer. One of the critical parameters to suppress LER investigated in the previous study was the effective reaction radius for deprotection reaction (R_p).[14] However, R_p cannot be directly measured by experiments. In chapter 1, the chemical parameters R_p and C_{th} were investigated by utilizing both the simulation and experimental results using a machine learning approach—Bayesian Optimization (BO).[15,16]

iii. Dissolution kinetics

The kinetics of polymer dissolution are more complex than a single parameter like C_{th} can fully describe. In practice, before the polymer film completely dissolves into the developer, it typically undergoes a transition from a rigid layer to a gel-like layer, in which the developer is partially absorbed.[17] Although this transition can occur rapidly, understanding its dynamics is still valuable for gaining insight into the mechanisms behind defect formation. There are problems such as the swelling of the resist, which can lead to defects like the formation of bridges on the resist pattern. It is critical to understand the dissolution kinetics.

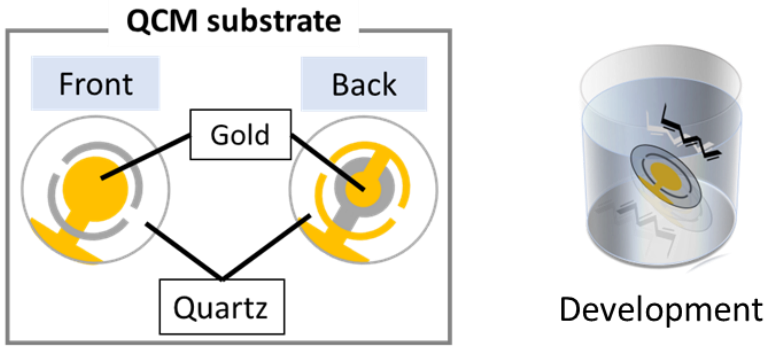

Figure 4 QCM substrate and the illustration of measuring.

Quartz crystal microbalance (QCM) method is an essential technique to understand the dissolution kinetics.[18] It measures the dissolution rate of the resist, a critical aspect of lithographic processing. QCM also tracks changes in impedance (ΔZ), which indicates energy loss during development.[19,20] The QCM substrate and the measuring illustration are shown in Fig. 4. Although QCM provides valuable measurements, the full potential of the impedance data which QCM produces is not fully utilized yet. In chapter 2, I introduce a stratified polymer

dissolution model (SPDM) that simulates the dynamic changes in frequency (Δf) and impedance during the development process, focusing on their relationship with the diffusion of polymer molecules in developers. Reproducing QCM charts have shown that impedance not only offers insights into the rate at which the resist dissolves but also provides information on the viscosity at the interface between the developer and the top layer of the resist. Based on impedance data, which allows for the extraction of key parameters such as the diffusion constant (D) and hydrodynamic radius (R_H) [21] from QCM measurements. Previously reported experimental QCM data for *t*-Boc protected poly(4-hydroxystyrene) (PHS) in an alkaline developer, aqueous tetramethylammonium hydroxide (TMAH) at different resist film thicknesses were analyzed.

iv. Image recognition

The line-and-space (L/S) pattern, as shown in Fig. 5(a), is a typical resist pattern used to evaluate the performance of the lithography process. A pair of line and space forms what is called a pitch, and half of the pitch corresponds to the feature size, also referred to HP. The minimum line width that can be fabricated reflects the industry's patterning capability. It is important to note that this is a periodic pattern used for process evaluation and should not be confused with the so-called technology node commonly referred to today.

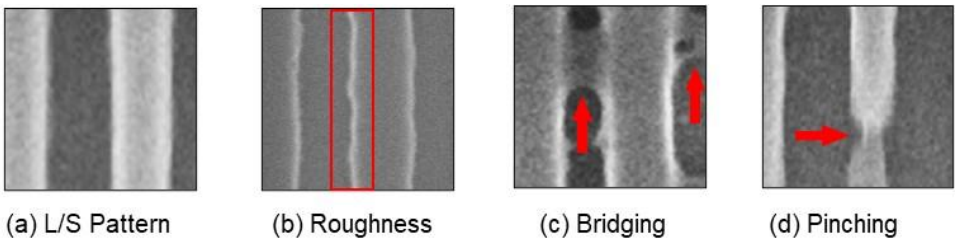

Figure 5 White regions are the polymers, while black regions are the silicon substrate. (a) A fine L/S pattern with clear straight edges. Edges that have (b) roughness (c) bridging defects, that connect two lines, and (d) A pinching defect on the line.

As pattern dimensions shrink, LER, as shown in Fig. 5, becomes more prominent due to the reduced line and space widths. This increases the likelihood of LER-induced bridging defects, as illustrated in Fig. 5(c). These defects occur stochastically, making them difficult to quantify and compare across different instances.

During the materials discovery process, pattern data with failures are obtained more than fine ones. This challenge motivated me to investigate and evaluate defective patterns. In chapter 3, a new method for evaluating L/S resist pattern defects based on an image recognition technology for evaluating massive patterns were demonstrated. L/S patterns with different HPs and exposure doses were printed by an EB writer. Approximately 2500 experimental scanning electron microscopy (SEM) images were automatically evaluated after image preprocessing with a Laplacian of Gaussian (LoG) image filter. This method measures the resist pattern as a whole and evaluates the pattern with integral indexes, especially targeting patterns with severe defects such as the patterns deformed by over dissolution or incomplete dissolving. The SEM images were analyzed using a method based on Hough transform which can detect fundamental geometric shapes such as lines. In the aspect of simulation model, Monte Carlo simulation was used to simulate the distribution of polymers that form resist patterns. As one of the applications of this method, a comparison between experimental and simulation results based on the indexes provided by the developed method and chemical parameters was conducted.

v. Machine learning

Machine learning has recently garnered significant attention in the field of lithography. Deep learning techniques, particularly neural networks, have been applied not only for prediction but also for image classification in optical lithography. Additionally, deep learning has been utilized to analyze defects in SEM images.[22]

Regression analysis offers several key advantages, particularly in understanding and modeling relationships between variables. It provides strong predictive capabilities by establishing mathematical relationships between inputs

and outputs. Unlike some complex machine learning models, regression models are relatively easy to interpret, allowing researchers to clearly understand how each independent variable affects the dependent variable. The method is also flexible, accommodating both linear and nonlinear relationships, and serves as a foundational tool for many advanced analytical techniques. These qualities make regression analysis a valuable approach for both exploratory and predictive data analysis.

Based on the estimated chemical parameters, simulation models to reproduce QCM data and the SEM evaluation results, a regression analysis model based on polynomial kernel was constructed. Polynomial regression extends linear regression by allowing for the modeling of nonlinear relationships between independent and dependent variables. This approach is particularly advantageous when the data exhibits curvature or more complex patterns that cannot be captured by a straight line. It provides greater flexibility in fitting a wide range of data trends while maintaining interpretability. Additionally, polynomial regression is relatively simple to implement and computationally efficient compared to more complex nonlinear models or black-box machine learning methods.

A practical application will demonstrate how these parameters provide valuable guidance for selecting or designing developer formulations that are better suited for next-generation photoresists.

vi. Overview

This thesis presents a comprehensive study of the pattern fabrication process, encompassing electron beam (EB) exposure, post-exposure baking (PEB), development, and final pattern inspection, as illustrated in Fig. 2. From a machine learning perspective, each stage is modeled to extract key chemical parameters as explanatory variables, using simulated data to represent the physical and chemical behavior of the resist material. The initial extraction of chemical parameters such as effective reaction radius was presented in Chapter 1. In Chapter 2, the development process is further analyzed through models calibrated against experimental results obtained via QCM measurements. Chapter 3 introduces a novel evaluation method that quantifies defective patterns, enabling even severely

defective outputs to be digitalized and used as target variables in supervised learning. Collectively, these efforts bridge the gap between physical process modeling and data-driven prediction. In Chapter 4, as a practical application, the relationship between the extracted explanatory variables and the final pattern quality is demonstrated, highlighting the potential of this integrated approach for predictive modeling and optimization in resist patterning.

References

[1] The international roadmap for devices and systems @IEEE

[2] M. Brink, Proc. SPIE **11517**, 1151702 (2020).

[3] J. G. Santaclara, G. Rispens, J. Bekaert, A. Thiam, M. Maslow, R. Hoefnagels, N. Zuurbier, L. Lent-Protasova, and F. C. Yin, Proc. SPIE **11612**, 1161204 (2021).

[4] T. Itani and T. Kozawa, Jpn. J. Appl. Phys. **52**, 010002 (2013).

[5] B. Rathsack, K. Nafus, S. Hatakeyama, Y. Kuwahara, J. Kitano, R. Gronheid, and A.V. Pret, Advances in Resist Materials and Processing Technology XXVI; **7273**, 727347 (2009).

[6] C. A. Mack and G. F. Lorusso, J. Vac. Sci. Technol. B **37**, 062903 (2019).

[7] G. F. Lorusso, V. Rutigliani, F. V. Roey, and C. A. Mack, Microelectronic Eng. **190**, 33 (2018).

[8] H. Ito, Microlithography/Molecular Imprinting Advances in Polymer Science Series (Springer, Heidelberg, 2005) Vol. 172, p. 37.

[9] Y. Kawai, A. Otaka, A. Tanaka, and T. Matsuda, Jpn. J. Appl. Phys. **33**, 7023 (1994).

[10] J. Nakamura, H. Ban, K. Deguchi, and A. Tanaka, Jpn. J. Appl. Phys. **30**, 2619 (1991).

[11] T. Kozawa and S. Tagawa, Jpn. J. Appl. Phys. **49**, 030001 (2010).

[12] T. Kozawa and T. Tamura, Jpn. J. Appl. Phys. **59**, 016503 (2020).

[13] T. Kozawa, J. Photopolym. Sci. Technol. **26**, 643 (2013).

[14] K. Azumagawa and T. Kozawa, Jpn. J. Appl. Phys. **60**, SCCC02 (2021).

[15] B. Shahriari, K. Swersky, Z. Wang, R. P. Adams, and N. D. Freitas, Proc. IEEE, **104**, 148 (2016).

[16] P. I. Frazier and J. Wang, Bayesian optimization for materials design, in *Information Science for Materials Discovery and Design* eds. T. Lookman, F. J. Alexander, and K. Rajan (Springer Nature, Switzerland, 2015) pp. 45-75.

[17] B. A. Miller-Chou, and J. L. Koenig, Prog. Polym. Sci. **28** 1223 (2003).

[18] W. D. Hinsberg, C. G. Willson, and K. K. Kanazawa, J. Electrochem. Soc. **133**, 1448 (1986).

[19] M. Toriumi, T. Itani, J. Yamashita, T. Sekine, and K. Nakatani, Proc. SPIE **4690**, 904 (2002).

[20] A. Sekiguchi, J. Photopolym. Sci. Technol. **23**, 421 (2010).

[21] Structures and physical properties of polymers, ed. Y. Matushita (Koudansha, Tokyo, 2013), pp.135–143.

[22] C. M. Bishop, *Pattern Recognition and Machine Learning* (Springer, New York, 2006).

Chapter 1: Estimating the effective reaction radius in polymer matrix

Chapter Overview

This chapter covers the pattern fabrication procedures of electron beam (EB) exposure, post-exposure baking (PEB), and development, as illustrated in Fig. 2(c), (e), and (f) of the General Introduction chapter. From a machine learning perspective, this chapter also presents simulated models designed to extract chemical parameters from these processes as explanatory variables.

1.1 Introduction

The fabrication of photomasks by electron beam (EB) lithography is the starting point of lithography used for the high-volume production of integrated circuits. There is a strict requirement on the pattern fidelity of photomasks, especially after the emergence of extreme ultraviolet (EUV) lithography in industry. On the other hand, the exposure dose required for the 13.5 nm wavelength of EUV is currently high, which makes the cost of chip manufacturing high in high-volume production lines as well. Hence, the improvement of resist sensitivity is the decisive factor in reducing the exposure dose, and thus, the cost of chip manufacturing.

Chemically amplified resists (CARs) decrease the exposure dose for the patterning by compensating for photon energy with heat energy.[1)] On the other hand, the sensitivity of CARs was found to be strongly related to the chemical gradient, which indicates the defect severity in both EUV[2)] and EB[3)] resists. CARs are generally composed of a photoacid generator (PAG), a quencher[4)], and a polymer with side chains partially protected by nonpolar protecting groups.[1)] The acids generated by photons or EB catalyze deprotection on a side chain of a polymer during postexposure baking (PEB). Owing to the low polarity of the protecting group, the polarity of deprotected polymers changes from low to high. Therefore, the polymer becomes hydrophilic and can be dissolved in an aqueous

developer.[5,6] CARs can meet the desired sensitivity by taking advantage of acid catalyzed deprotection. Thus, CARs are thought to be promising for high-resolution lithography.[7] In particular, the acid reaction–diffusion process during PEB is critical in controlling the feature size of a latent pattern. On the other hand, the processes in latent pattern formation such as the interactions between electrons and materials, secondary electron emission, and chemical reactions are stochastic.[8] The distribution of protected units is directly affected by the accumulation of these stochastic effects. Consequently, the protected unit concentration (C_p) after PEB is uncertain (protected unit fluctuation). Furthermore, C_p determines the solubility of resist films in developers. In other words, C_p determines the dissolution threshold of resist films. Thus, the development process ultimately manifests the protected unit fluctuation as defects, such as line edge roughness (LER), on the resist pattern.

Previously, investigations of stochastic defects suggested that LER can be suppressed by increasing the effective reaction radius for deprotection (R_p),[1,9] which is an essential parameter indicating the efficiency of chemical reactions per unit diffusion length of acids. Thus, R_p is related to both sensitivity and resolution. However, R_p cannot be directly measured by experiments. In this study, by comparing the simulation results with the experimental results R_p was investigated. Line-and-space patterns with different half pitches (HPs) were fabricated at different exposure doses and were utilized as the subject of analysis. An HP denotes the designed line widths in this study. The line width of fabricated resist patterns was measured by scanning electron microscopy (SEM). On the other hand, because the line width of a simulation model depends on the dissolution threshold C_{th}, was also investigated at the same time. In the optimization of R_p and C_{th}, Bayesian optimization (BO) was conducted. BO is a widely used tool for finding solutions in both scientific research and social studies.[10] As a predictive model, BO can capture the underlying relationships among parameters obtained from previous experimental results. Furthermore, because BO is different from the other optimization algorithms based on gradient descent, it provides a global view of optimization and is suitable for multimodal frameworks.[10,11] Hence, as the optimization algorithm, Gaussian process (GP) regression was selected for parameter tests in this study.

1.2 Experimental procedure

A chemically amplified resist was used in this experiment.[1)] The polymer film of the resist was composed of a synthesized copolymers of poly(4-hydroxystyrene) (PHS) and poly[4-(*tert*-butoxycarbonyl)oxy-styrene] (PTBS) (M_w 12700). The *tert*-butoxycarbonyl (*t*-BOC) protecting group (54.6 mol%) was introduced to protect the hydroxyl groups of PHS. That is, the protected unit concentration was 2.26 (units) nm^{-3}. Approximately 3 wt% polymer powder was dissolved in propylene glycol monomethyl ether acetate (PGMEA), to which PAG, triphenylsulfonium nonaflate (TPS-nf), and a quencher, trioctylamine (TOA), were subsequently added. The concentrations of TPS-nf and TOA were adjusted to 0.2 and 0.1 molecules nm^{-3} in a film for spin coating, respectively. Spin coating was then carried out on a Si substrate for 4000 rounds per minute for 30 s, which was followed by prebaking at 90 °C for 90 s. The resist thickness was measured to be 50 nm using an ellipsometer (Meiwafosis FS-1). The spin-coated resist was stored in vacuum at room temperature before EB exposure. It was then exposed to a 125 keV EB (Elionix ELS-100T) at 192, 208, 224, 240, 256, 272, 288, 304, and 320 μC cm^{-2}. The EB current was 100 pA. The pitches of line-and-space patterns were 70, 80, 90, 100, 110, and 120 nm. After exposure of the resist to EB, the resist was subjected to PEB at 110 °C for 1.5 min. Development was carried out by soaking the resist in a 2.38 wt% tetramethylammonium hydroxide (TMAH) aqueous developer (Tokyo Ohka Kogyou NMD-3) at 23 °C for 30 s and rinsed with pure water for 15 s. SEM images of the resist were taken at an acceleration voltage of 4 kV using Hitachi High-Tec. S-5500. The emission currents for the observation of resist patterns ranged from 2700 to 7100 nA. The size of SEM images was 1280 × 960 pixels. The SEM images were captured in the fast-scan mode with 64 frame integration and the scale was 0.98 nm/pixel. The magnification was 100,000. Note that observation by SEM could cause damage, specifically, shrinkage of the resist patterns.[12,13)] The damage can be reduced by decreasing the acceleration voltage and the number of electrons.[12)] The emission current, the frame integration, and acceleration voltage were decreased to the extent in which the images were still observable.

1.3 Simulation model

The simulation model was divided into two parts. The first part simulated the reactions in the resist during EB exposure. As a result, the concentration and distribution of acids after exposure were generated. Note that before PEB, the preneutralization of acids was taken into account.[14,15] The second part simulated the acid diffusion and the deprotection of protected units during PEB. Finally, the distribution of protected units after PEB was obtained.

Table 1-I. Parameters used in simulation.

Acceleration voltage of electron beam (kV)	125
Beam blur (σ_b) (nm)	2.0
Resist thickness (nm)	20
Stopping power (eV nm^{-1}) [16]	0.418
Resist film density (g cm^{-3})[17]	1.2
Thermalization distance (nm) [18]	3.2
PAG concentration (nm^{-3})	0.2
TOA concentration (nm^{-3})	0.1
Reaction radius of PAG (nm) [18]	0.70
Effective reaction radius for neutralization (nm)	0.5
Effective reaction radius for deprotection (nm)	0.02–0.15
Protection ratio (mol%)	54.6
Deprotonation efficiency of proton source[19]	1.0
Deprotonation efficiency of nonproton source[20]	0.59
Acid generation efficiency[20]	0.87
Diffusion constant of acids (nm^2 s^{-1})	1.0

Diffusion constant of quenchers ($nm^2\ s^{-1}$)	1.0
Diffusion constant of protected units ($nm^2\ s^{-1}$)	0.0
PEB time (s)	90
HP (nm)	35–60
Dose ($\mu C\ cm^{-2}$)	192–320

In the EB exposure simulation part, the formation of acid images of line-and-space patterns was calculated on the basis of the sensitization mechanism of chemically amplified EB resists. The beam profile I_b (x: perpendicular to a line pattern) and the exposure pattern width w were defined as

$$I_b(x) = \frac{I_{b0}}{\sqrt{2\pi}\sigma_b} \int a \exp[-\frac{(x-x')^2}{2{\sigma_b}^2}]dx' ,$$

$$a = 1\ (-\frac{w}{2} + np < x' < \frac{w}{2} + np),$$

$$a = 0\ [-\frac{w}{2} + np < x' < \frac{w}{2} + (n+1)p], \quad (1\text{-}1)$$

where I_{b0}, σ_b, p, and n are the exposure dose ($\mu C\ cm^{-2}$), the beam blur, the pitch of the line-and-space pattern, and an integer, respectively. The parameters and their corresponding values used in the first part are summarized in Table 1-I.[16–20] The exposure pattern widths were set to be HP. The beam blur was approximated using the Gaussian function. The beam blur ($1\sigma_b$) was set to 2.0 nm. The acceleration voltage of the electron beam was 125 kV. The calculated area was $p \times 200\ nm^2$. The calculated length in the depth direction was set to be 20 nm to save computational time. The thermalization distance of secondary electrons in PHS has been reported to be 3.2 nm.[18] The deprotonation efficiency of protected unit radical cations was set to 0.59, which was obtained by titration using the acid-sensitive dye Coumarin 6.[20] The acid generation efficiency in 54.6% protected PHS was 0.87.[20] The trajectories of secondary electrons and the reaction of thermalized electrons with PAG were calculated by a Monte Carlo method. The details of the calculation procedure have been reported in a previous paper.[16]

The acids generated after EB exposure were first neutralized by the quencher before PEB. The preneutralized concentration distribution was the initial acid state of PEB. In the PEB process simulation part, the reaction–diffusion equations describing the dynamics of acids and quenchers are as follows[5, 6, 21-23)]

$$\frac{\partial C_{\mathrm{acid}}}{\partial t} = \nabla(D_{\mathrm{acid}}\nabla C_{\mathrm{acid}}) - 4\pi R_{\mathrm{n}}\left(D_{\mathrm{acid}} + D_{\mathrm{q}}\right)C_{\mathrm{acid}}C_{\mathrm{q}}, \tag{1-2}$$

$$\frac{\partial C_{\mathrm{q}}}{\partial t} = \nabla\left(D_{\mathrm{q}}\nabla C_{\mathrm{q}}\right) - 4\pi R_{\mathrm{n}}\left(D_{\mathrm{acid}} + D_{\mathrm{q}}\right)C_{\mathrm{acid}}C_{\mathrm{q}}, \tag{1-3}$$

where C_{acid}, C_{q}, R_{n}, t, D_{acid}, and D_{q} are the concentration of acids and quenchers, the effective reaction radius for neutralization, the time, and the diffusion constants of acids and quenchers, respectively. The acid and quencher dynamics during PEB at a time interval of 0.001 s were calculated by solving Eqs. (1-2) and (1-3). On the other hand, the protected unit concentration was calculated as

$$\frac{\partial C_{\mathrm{p}}}{\partial t} = -4\pi R_{\mathrm{p}}D_{\mathrm{acid}}C_{\mathrm{acid}}C_{\mathrm{p}}, \tag{1-4}$$

where C_{p} and R_{p} represent the concentration of protected units and the effective reaction radius for deprotection, respectively.

1.4 Analytical methods

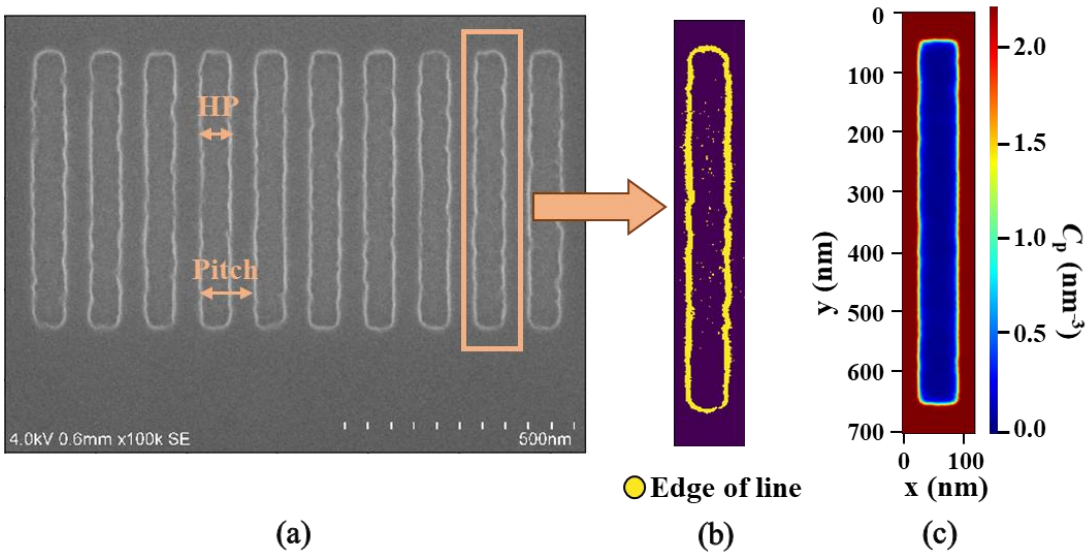

Figure 1-1 SEM image of experimental results. All lines were exposed to EB at 224 μC cm^{-2}. The designed HP was 60 nm. (b) Edges extracted from SEM image using Otsu binarization. The yellow pixels represent the edge of the line. (c) C_p obtained from the simulation under the corresponding experimental condition. The color bar illustrates the protected unit concentration. R_p was 0.06 nm.

The line width was used as a reference in the comparison between experimental results and simulation results. The SEM image shown in Fig. 1-1(a) is a representative example of experimental results. In Fig. 1-1(a), there were 10 lines drawn under the same condition, which means that these 10 lines were designed to have the same HP and irradiated at the same dose. In the case of Fig. 1-1(a), the lines were exposed to EB radiation at 224 μC cm^{-2} dose and the designed HP was 60 nm (Note that the exposed section was defined as the line). Figure 1-1(b) shows the result of edge extraction of a line on the right side of Fig. 1-1(a), by Otsu binarization (Fig. 1-2).[24)]

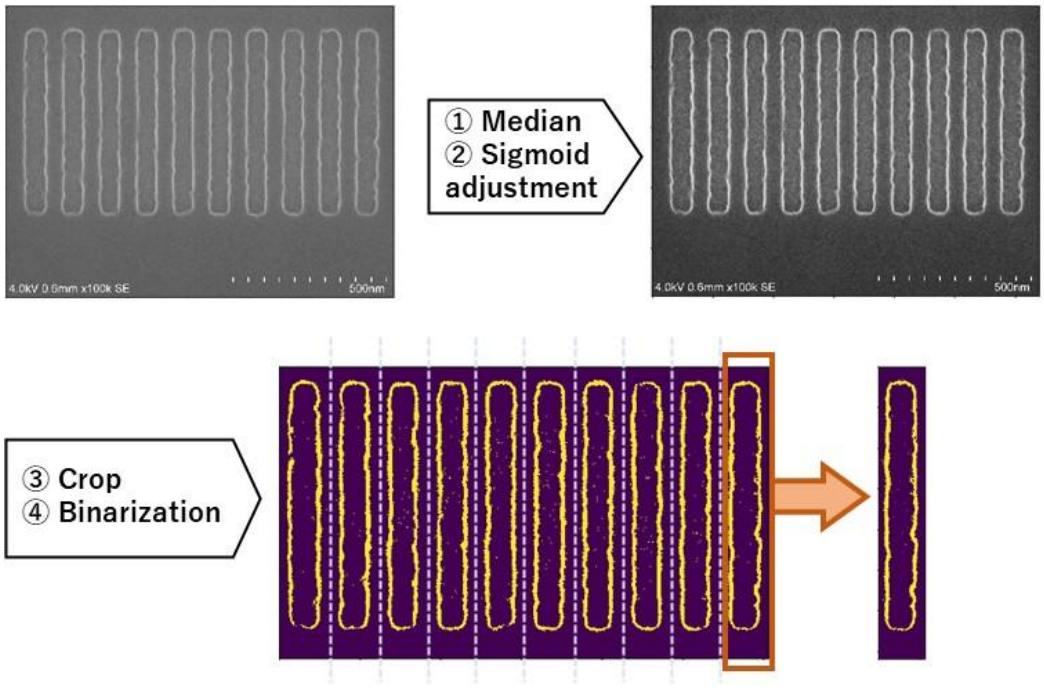

Figure 1-2 Preprocessing of SEM image before measuring HP one by one line. The SEM image demonstrated in this figure is a representative example. The pattern was exposed to EB at 224 μC/cm^2 dose and the HP was 60 nm for one line (Note that the exposed section was defined as line). The SEM image was first filtered with median method to denoise, followed by sigmoid adjustment to increase the contrast. The section including patterns was then cropped out and binarized with Otsu method. Finally, lines were cut out one by one to measure its HP.

The yellow pixels in the SEM image were classified as the edge owing to the high intensity of pixels before classification. After classification, the pixels classified into the edge were set to be 1 and the others were set to be 0. For the resist patterns, HPs were changed from 35 to 60 nm. The lengths of patterns were designed to be 600 nm under all conditions. The line width was measured from two sides. In determining the line width, the integration of the pixel values of four adjacent lines was calculated from the outer side (far from the line pattern) to the inner side (near the line pattern). When the sum of the pixel values of four lines first exceeded three times the designed pattern length (600 nm × 3 = 1800 nm), the line on the most inner side among four lines was seen as the end of the line pattern.

When the line width was smaller than a quarter of the corresponding HP, the line was seen as a severely defective line and discarded.

Figure 1-1(c) shows the C_p distribution before development. The horizontal lengths are the pitches (the double of designed HPs) and the vertical lengths are 700 nm under all conditions. For the pattern, the line widths were designed to be the corresponding HPs, and the lengths of patterns were designed to be 600 nm under all conditions. It was assumed that only at C_p below a certain concentration the deprotected polymers can be dissolved in 2.38 wt% TMAH, namely, the dissolution threshold C_{th}. Hence, the regions whose C_p is below C_{th} were classified as line regions after development. Other regions were classified as space regions. The pixel values in line regions were set to be 1 and those in other regions were set to be 0. The methods of finding edges and evaluating line widths were the same as those used for the experimental results.

Except for the severely defective lines, almost all the 10 lines obtained from the experiment were measured and compared with the simulation results. The root mean square error (RMSE) between experimental and simulation results ($RMSE_{HP}$) was used for evaluation and is defined as

$$RMSE_{\mathrm{HP}} = \sqrt{\frac{\sum_{\mathrm{n}=1}^{\mathrm{m}}(LW_{\mathrm{SEM,n}} - LW_{\mathrm{Simul,n}})^2}{\mathrm{m}}}, \tag{1-5}$$

where m, n, LW_{SEM}, and LW_{Simul} represent the number of lines, an integer, the line width of a line in the SEM image, and the line width of the corresponding simulation result, respectively. The sum of $RMSE_{HP}$ was used as the observation value, to be exact, an acquisition function that determines the sampling site.

GP regression is a typical method for Bayesian inference. In this study, GP regression was utilized in finding the probable values for R_p and C_{th}. The mean function was constant. The GP prior mean was assumed to be zero and the Bayesian credible interval for the posterior probability was set to be 95%. The Matérn covariance function k is defined as[11)]

$$k(x_i, x_j) = \frac{2^{1-\upsilon}}{\Gamma(\nu)}\left(\frac{\sqrt{2\upsilon}}{l}\, d(x_i, x_j)\right)^{\nu} K_{\nu}\left(\frac{\sqrt{2\upsilon}}{l}\, d(x_i, x_j)\right), \tag{1-6}$$

where l, Γ, K_{ν}, and ν are the length scale, gamma function, modified Bessel function, and the parameter that controls the smoothness of function k, respectively.

The distance between x_i and x_j is the Euclidean distance denoted by $d(x_i, x_j)$. In this study, since the expected improvement was a small $RMSE_{HP,}$ the subsequent target was simply decided by the lowest credible bound of the acquisition function.

1.5 Results and discussion

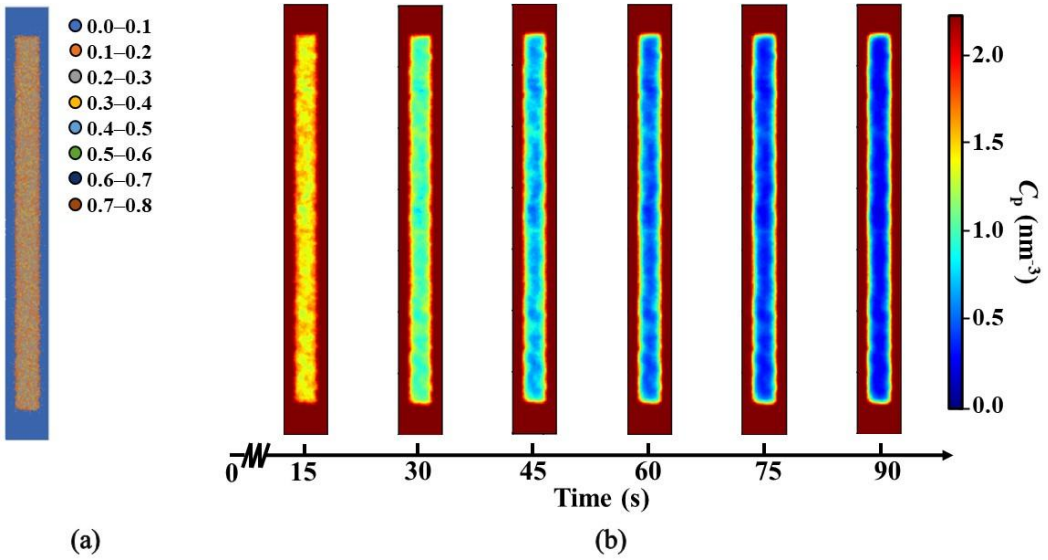

Figure 1-3 (a) Representative simulation result of EB exposure simulation part. Different colors represent different concentrations of PAG decomposed by EB irradiation. The unit is molecules nm^{-3}. (b) C_p changes during PEB obtained by the simulation. The HP and dose were 35 nm and 192 μC cm^{-2}, respectively. R_p was 0.05 nm.

A representative simulation result is shown in Fig. 1-3. The PAG decomposed by EB exposure leads to acid generations. The simulation result of PAG decomposition immediately after EB exposure is shown in Fig. 1-3(a). The simulation results in Fig. 1-3(b) show how C_p changes during PEB. The C_p of 54.6% protected PHS was 2.26 nm^{-3}. Therefore, the initial concentration was 2.26 nm^{-3}, which is shown in dark red.

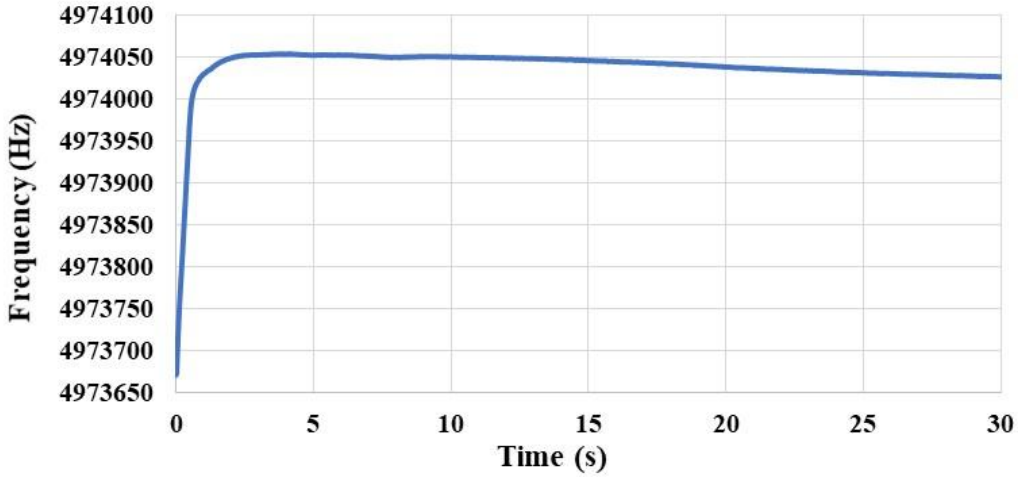

Figure 1-4 Frequency change of 30 mol% protected PHS developed in 100% TMAH measured by QCM.

To search for the probable values of C_{th} and R_p, their possible ranges were estimated beforehand. For C_p, PHS protected by *t*-BOC was observed to dissolve in the 2.38 wt% TMAH aqueous developer when its protection ratio was below 30%, the protected unit concentration of which is 1.44 nm^{-3}, as shown in Fig. 1-4. On the other hand, the initial protected unit concentration was 2.26 nm^{-3}. From these findings, the dissolution threshold was investigated between 1.1 and 2.0 nm^{-3}. In the case of R_p, previous studies showed that the chemically amplified resists including state-of-the-art resists had R_p values ranging from 0.06 to 0.16.[25–31] Judging from these values, the possible R_p range in this study was set at 0.02–0.15 nm.

The line widths were measured using SEM images of resist patterns for six different HPs and nine different doses. A total of 56 SEM images were used, as shown in Fig. 1-5.

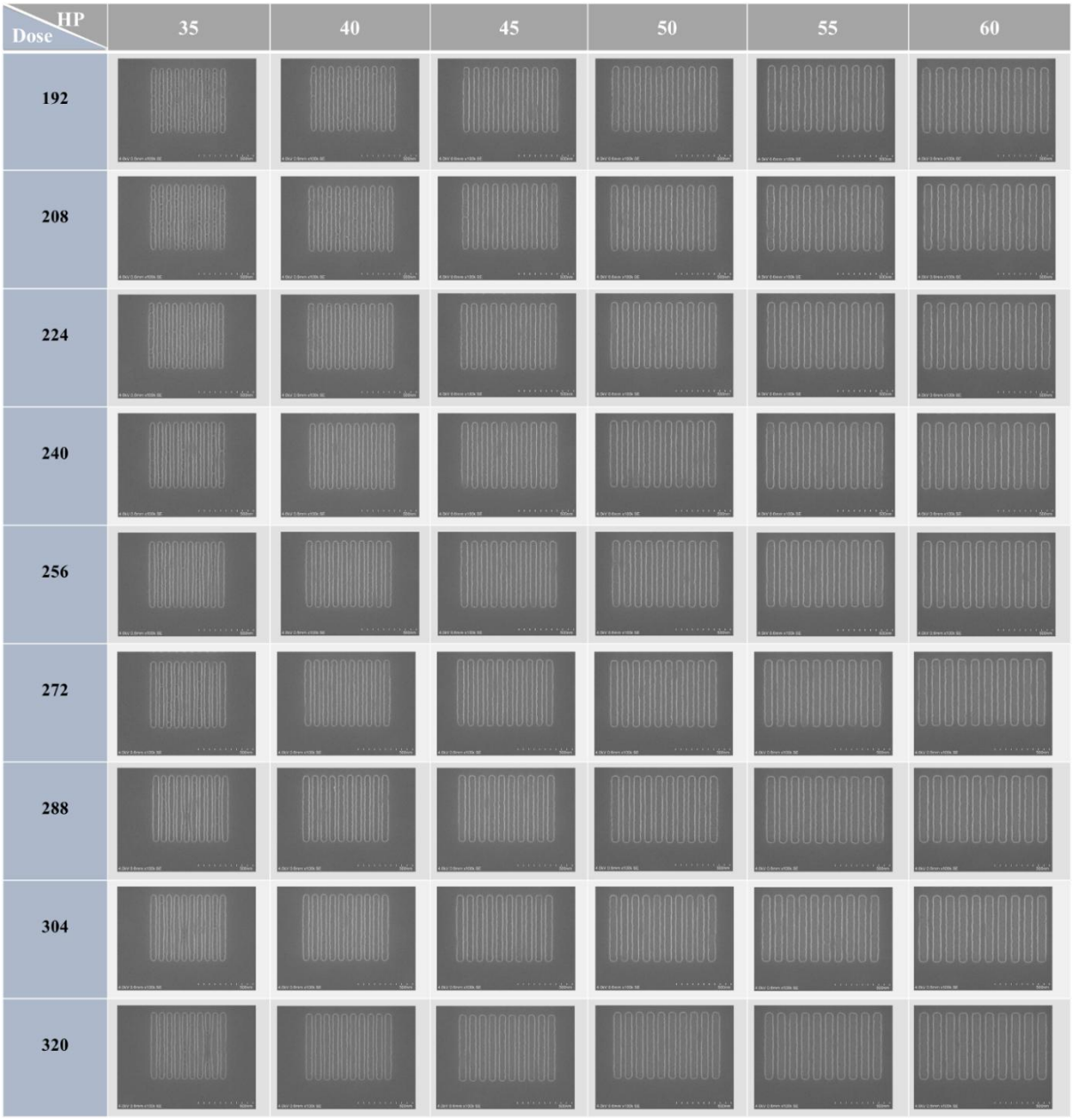

Figure 1-5 SEM images used in this study. The SEM images at different conditions. HP ranges from 35 to 60 nm. Doses range from 192 to 320 μC/cm^2.

Since different R_p and C_{th} values finally lead to different line widths in the simulation process, line widths in the simulation were measured every time when R_p or C_{th} changed. To compare between simulation and experimental results, $RMSE_{HP}$ were calculated for all the SEM images [Eq. (1-5)] and corresponding

simulation results that had the same doses and targeted HPs. Since one set of R_p and C_{th} must be applied to 56 SEM images with different HPs and doses, 56 comparison results ($RMSE_{HP}$) for the corresponding R_p and C_{th} were summed up. A small sum of $RMSE_{HP}$ values means that the R_p and C_{th} used in the simulation were close to the correct solution. The experimental errors (the fluctuation of line width) at 35, 40, 45, 50 ,55, and 60 nm HP were 5.03, 2.30, 1.87, 1.72, 1.70, and 1.67 nm, respectively. The simulation errors caused by the use of the Monte Carlo method for the calculation of acid generation is considered to be smaller than the experimental errors, because the PEB process was simulated by applying not the Monte Carlo method but the probability density model.

Table 1-II. The initial data set used in BO. C_{th} and R_p were the variables, and the sum of $RMSE_{HP}$ values was the target variable.

R_p (nm)	C_{th} (nm^{-3})	Sum of $RMSE_{HP}$ values
0.02	1.1	1684.29
0.02	2.0	341.77
0.15	1.1	375.97
0.15	2.0	771.07
0.08	1.4	341.77

BO was conducted to find the most suitable R_p and C_{th} for the simulation model. The inference kernel used was the Matérn kernel [Eq. (1-6)]. The entire length scale of the Matérn kernel was examined automatically between 0.01 and 100. ν was set to be 1.5 in this study. The resulting fitting score was more than 99.9%. The prediction started from the five data sets shown in Table 1-II. The variable set of these five data included the end values of R_p and C_{th} and another datum roughly estimated (R_p: 0.08 nm; C_{th}: 1.4 nm^{-3}). The method to add a data obeyed the probability distribution. The possibility was set at 95%. The lower credible bound was changed as data were added.

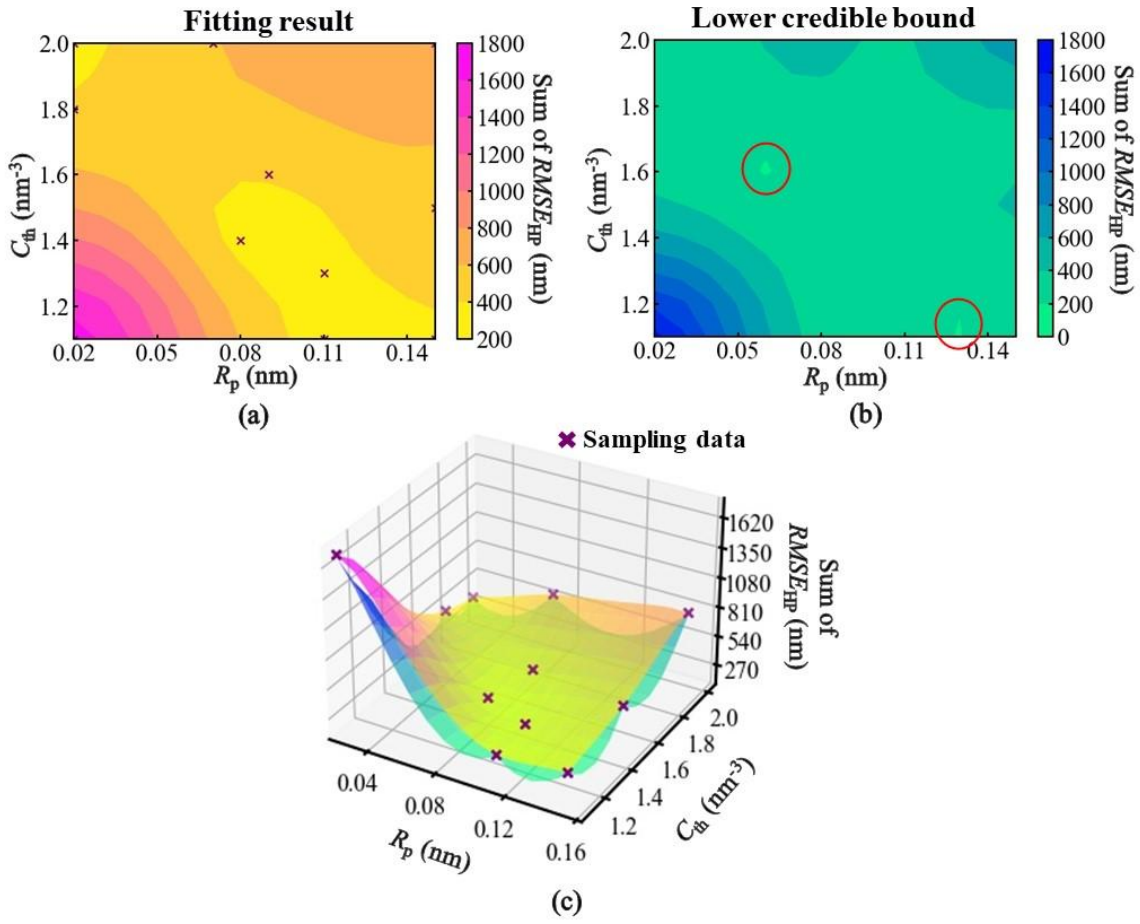

Figure 1-6 Results of BO using Gaussian regression process using 11 training data. (a) Fitting result of GP regression. (b) Lower credible bound distribution obtained by BO. (c) Overlapping contour graph of both fitting results and lower credible bound in a three-dimensional figure.

Figure 1-6 shows an example to illustrate the results of BO. The number of data used was 11. The sum of $RMSE_{HP}$ values is shown in different colors. The yellow-red region in Figs. 1-6(a) and (c) show the fitting results that indicate the correlation of the values and their distribution. The blue-green color region indicates the lower credible bound where the smallest sum of $RMSE_{HP}$ values may appear. The red circles in Fig. 1-6(b) are the lowest position, and their corresponding R_p and C_{th} were used in the following simulation. Furthermore, these variables and their resulting sum of $RMSE_{HP}$ values were added together with

the data set calculated before. It was used as a new data set for the next optimization.

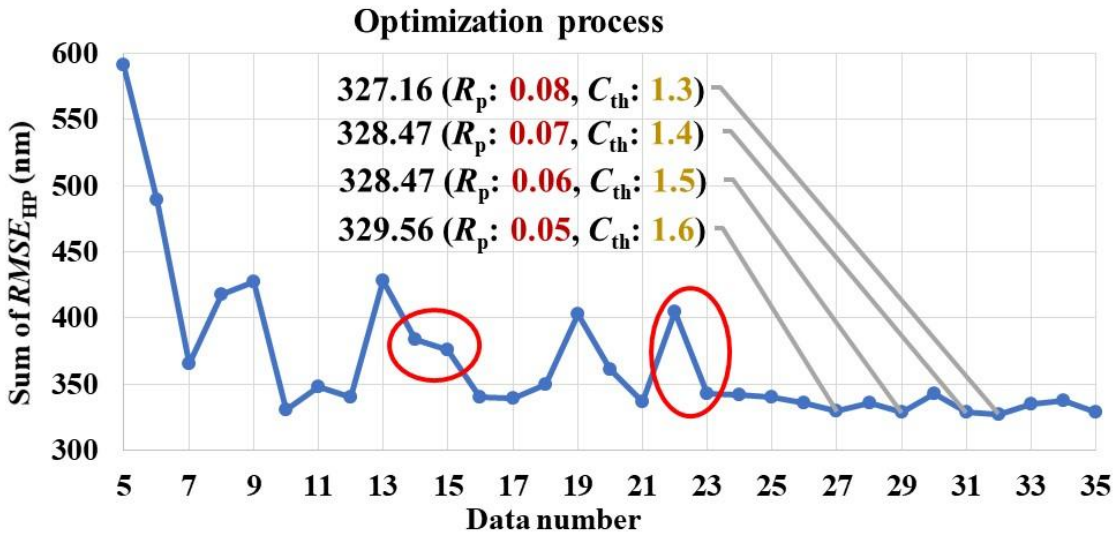

Figure 1-7 Change of calculated sum of $RMSE_{HP}$ values along with data addition. The method of selecting new data for the simulation was described in Sect. 4. The variables with smallest sums of $RMSE_{HP}$ values were labeled with actual values.

As shown in Fig. 1-7, the sum of $RMSE_{HP}$ values gradually became stable with increasing number of data added. Since the variable values predicted using 35 data were the same as those predicted using 29 data (R_p: 0.06 nm; C_{th}: 1.5 nm^{-3}), this suggests that the optimization was coming to the end. From the sum of $RMSE_{HP}$ values determined by calculation, the most probable ranges for R_p and C_{th} are 0.05–0.08 nm and 1.3–1.6 nm^{-3} and, respectively. Generally, before the addition of the 23rd data, the prediction accuracy was not good. Two significant inference changes are encircled in red in Fig. 1-7. The first was observed for the data that increased from 14 to 15 and the second was for the data that increased from 22 to 23. The changes of fitting results are shown in Fig. 1-8.

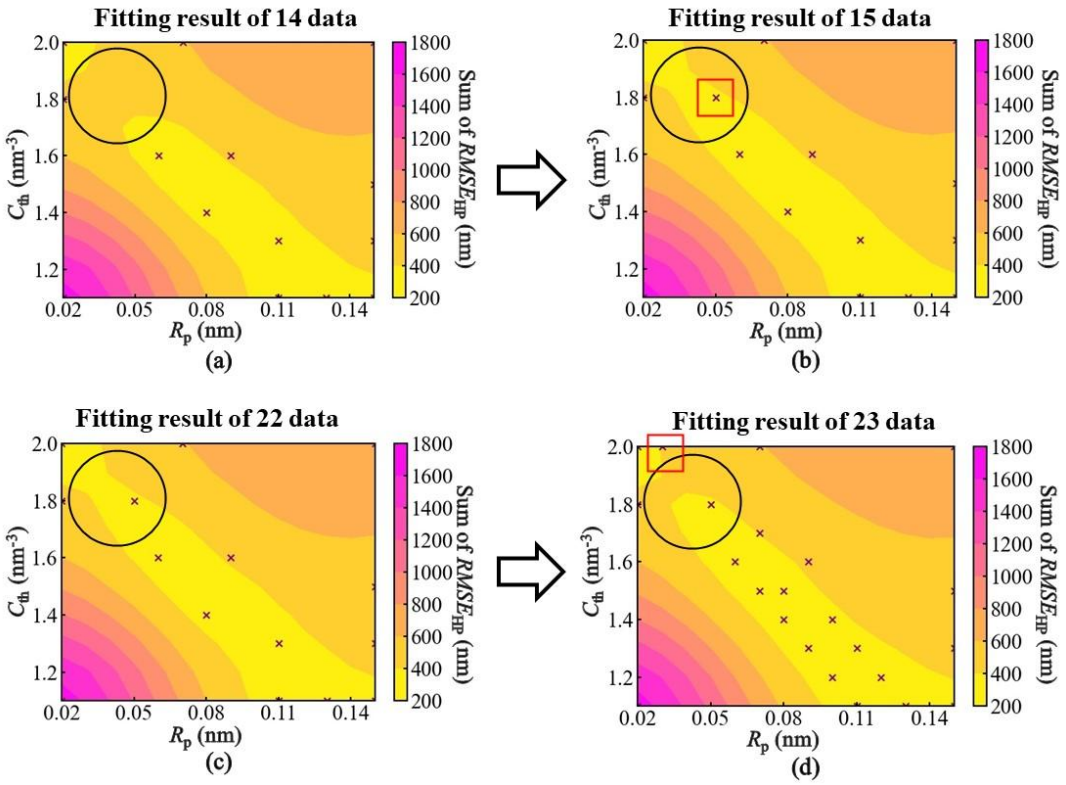

Figure 1-8 From (a) to (b), the color of the region encircled in black changed from orange to yellow after adding the data in the red box shown in (b). From (c) to (d), the color of the region encircled in black changed from yellow to orange after adding the data in the red box shown in (d).

From Figs. 1-8(a) and (b), the region encircled in black was inferred to be possible until the addition of the 14th datum. After the 23rd datum was added [from Figs. 1-8(c) and (d)], the sum of $RMSE_{HP}$ values of the predicted variables increased. The variables in red box in Fig. 1-8(b) were R_p=0.05 nm and C_{th}=1.8 nm^{-3} and those in Fig. 1-8(d) were R_p=0.03 nm and C_{th}=2.0 nm^{-3}. This indicates that, although C_{th} and R_p seem to have an inversely proportional correlation along the diagonal in the C_{th}–R_p plane, R_p is unlikely to be smaller than 0.03 nm.

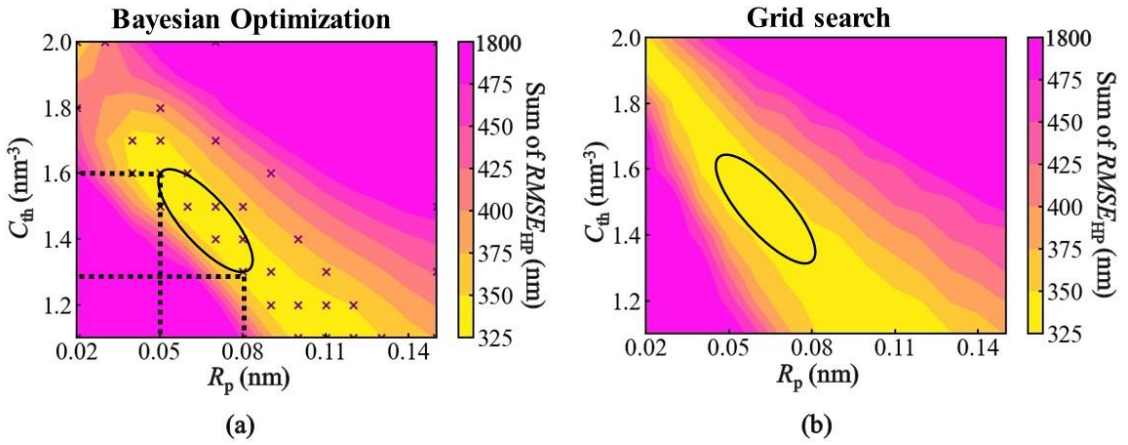

Figure 1-9 Distribution of sum of $RMSE_{HP}$ values in C_{th}–R_p plane. To show the result clearly, the region with the sum of $RMSE_{HP}$ values larger than 500 was merged into the pink area. The area encircled in black is the region where the sum of $RMSE_{HP}$ values is smaller than those in other areas. (a) Result of BO obtained using 35 data. (b) Result of grid search obtained using 140 data.

To verify BO, a grid search was conducted using 140 data. Four smallest sums of $RMSE_{HP}$ values were the same as the results of BO (data labeled with concrete in Fig. 1-7). This confirmed that BO found the best 4 results within 35 data sets, which is far smaller than the number of entire 140 data. Figure 1-9 shows the distribution of the sum of $RMSE_{HP}$ values in the C_{th}–R_p plane. The distribution obtained by BO was similar to that obtained by the grid search. The best-fitted values can also be obtained using the least squares regression with gradient descent with a small number of iterations. However, it does not provide the state around the best-fitted values similarly to that shown in Fig. 1-9. BO clarified the whole view of fitting accuracy in the C_{th}–R_p plane with the small number of iterations. The probable values for C_{th} and R_p were 1.3–1.6 nm^{-3} and 0.05–0.08 nm, respectively. C_{th} is likely to be larger than 1.44 (30 mol% protected PHS), as shown in Fig. 1-9.

Alhough BO and grid search suggested that the combination of R_p of 0.08 nm and C_{th} of 1.3 nm^{-3} was the best fitted values, the combination of R_p of 0.06 nm and C_{th} of 1.5 nm^{-3}, which was suggested by BO, might be closer to the correct solution.

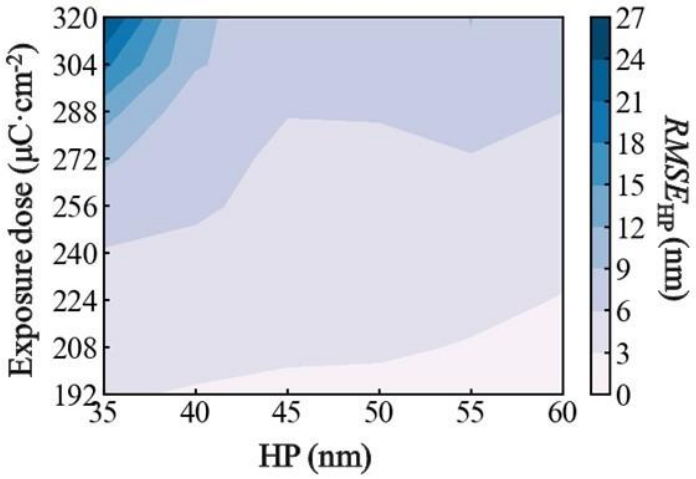

Figure 1-10 $RMSE_{HP}$ distribution when R_p was 0.06 nm and C_{th} was 1.5 nm^{-3}.

The $RMSE_{HP}$ distribution is shown in Fig. 1-10. The experimental results well fitted in the large-HP and low-exposure-dose region. In the large-exposure dose and small-HP regions, the fitting accuracy degraded. This is considered to be due to the fact that the resist patterns were deformed during development and rinsing processes owing to excess chemical reactions during PEB.

1.6 Conclusion

To search for R_p, lithography experiments with line-and-space patterns were conducted at different exposure doses and HPs. The SEM images of resist patterns were used to measure the line width for experimental data. The EB exposure process and acid reaction–diffusion process during PEB were simulated. Since the line width of simulation patterns was significantly affected by the dissolution threshold C_{th}, it had to be evaluated together with R_p.

To find R_p and C_{th}, a comparison was made between experimental and simulation results of the line width. The probable values of R_p and C_{th} were determined by BO. GP regression using the Matérn covariance kernel was used for Bayesian inferrence. BO effectively reduced the number of iterations from 140 to 35. Furthermore, the result was verified by a grid search. The probable values of C_{th} and R_p were 1.3–1.6 nm^{-3} and 0.05–0.08 nm for 54.6 mol% protected PHS resist under the PEB conditions of 110 °C and 1.5 min, respectively.

1.7 Reference

1) T. Kozawa, Jpn. J. Appl. Phys. **63**, 050101 (2024).

2) S. Kanna, H. Inabe, K. Yamamoto, T. Fukuhara, S. Tarutani, H. Kanda, W. Kenji, K. Kodama, and K. Shitabatake, Proc. SPIE **6153**, 615308 (2006).

3) M. Harumoto, J. J. Santillan, C. Nakayama, Y. Tanaka, T. Motono, M. Asai, and T. Itani, J. Photopolym. Sci. Technol. **32**, 321 (2019).

4) A. Sekiguchi, H. Konishi, and M. Isono, J. Photopolym. Sci. Technol. **25**, 467 (2012).

5) T. Itani and J. J. Santillan, J. Vac. Sci. Technol. B **27**, 2986 (2009).

6) Y. Iwashige, Y. T. Ito, T. Kozawa, K. Sakamoto, and M. Muramatsu, Jpn. J. Appl. Phys. **62**, 036502 (2023).

7) H. Betsumiya, Y. Jin, Y. T. Ito, T. Kozawa, K. Sakamoto, and M. Muramatsu, Jpn. J. Appl. Phys. **62**, 066501 (2023).

8) D. Hinsberg, C. G. Willson, and K. K. Kanazawa, J. Electrochem. Soc. **133**, 1448 (1986).

9) K. K. Kanazawa and J. G. Gordon II, Anal. Chem. **57**, 1771 (1985).

10) W. Hinsberg, F. A. Houle, S. W. Lee, H. Ito, and K. Kanazawa, Macromolecules **38**, 1882 (2005).

11) M. Toriumi, T. Ohfuji, M. Endo, and H. Morimoto, J. Photopolym. Sci. Technol. **12**, 545 (1999).

12) H. Ito, IBM J. Res. Dev. **45**, 683 (2001).

13) K. J. Harry, S. Strobel, J. K. W. Yang, H. Duan, and K. K. Berggren, J. Vac. Sci. Technol. B **29**, 06FJ01 (2011).

14) A. Sekiguchi, J. Photopolym. Sci. Technol. **26**, 479 (2013).

15) M. Kasper, L. Traxler, J. Salopek, H. Grabmayr, A. Ebner, and F. Kienberger, Biosensors **6**, 23 (2016).

16) M. Toriumi and T. Itani, Proc. SPIE **4690**, 904 (2002).

17). A. Sekiguchi, J. Photopolym. Sci. Technol. **23**, 421 (2010).

18) C. A. Mack, Modeling Solvent Effects in Optical Lithography (doctor thesis, the University of Texas at Austin, Texas, 1998) pp.40-61.

19) T. Otsuka, Y. Jin, N. Tanaka, and T. Kozawa, Jpn. J. Appl. Phys. **61**, 056503 (2022).

20) C. A. Mack, J. Electrochem. Soc. **134**, 148 (1987).

21) N. L. Thomas and A. H. Windle, Polymer **23**, 529 (1982).

22) B. Hunek and E. L. Cussler, AIChE J. **48**, 661 (2002).

23) C. Y. Hui and K. C. Wu, J. Appl. Phys. **61**, 5129 (1987).

24) C. Y. Hui, K. C. Wu, R. C. Lasky, and E. J. Kramer, J. Appl. Phys. **61**, 5137 (1987).

25) Y. T. Ito, K. Watanabe, Y. Jin, T. Kozawa, K. Sakamoto, and M. Muramatsu, Jpn. J. Appl. Phys. **63**, 018002 (2024).

26) Structures and physical properties of polymers, ed. Y. Matushita (Koudansha, Tokyo, 2013), pp.135-143.

27) Y. T. Ito, H. Betsumiya, T. Kozawa, K. Sakamoto, and M. Muramatsu, Jpn. J. Appl. Phys. **61**, 066506 (2022).

28) H. Betsumiya, Y. T. Ito, T. Kozawa, K. Sakamoto, and M. Muramatsu, Jpn. J. Appl. Phys. **62**, 036503 (2023).

29) T. Fukuyama, T. Kozawa, S. Tagawa, R. Takasu, H. Yukawa, M. Sato, J. Onodera, I. Hirosawa, T. Koganesawa, and K. Horie, Appl. Phys. Express **1**, 065004 (2008).

30) N. Tanaka, K. Matsuoka, T. Kozawa, T. Ikeda, Y. Komuro, and D. Kanawa, Jpn. J. Appl. Phys. **61**, SD1016 (2022).

Chapter 2: Stratified polymer dissolution model based on impedance data from quartz crystal microbalance method

Chapter Overview

This chapter focuses on the pattern fabrication procedure of development, as illustrated in Fig. 2(f) of the *General Introduction* chapter. From a machine learning perspective, it introduces simulated models aimed at reproducing the experimental results obtained via quartz crystal microbalance (QCM) measurements. These models are used to extract chemical parameters from the development process as explanatory variables, providing insight into the underlying mechanisms and their influence on pattern formation.

2.1 Introduction

As feature sizes continue to shrink, the stochastic generation of defects in patterns becomes increasingly a severe problem, leading to reduced product yield and increased manufacturing costs.[1)] Swelling and insufficient dissolution during development are primary causes of bridging defects in patterns.[2,3)] In response, new resists and corresponding developers, such as organic developers, are being explored to improve the fidelity of resist patterns. Previous studies have compared the traditional developer, 2.38 wt% (0.26 N) tetramethylammonium hydroxide (TMAH) aqueous developer, with alternatives such as a tetrabutylammonium hydroxide (TBAH) aqueous developer.[3-7)] Since 1986, the quartz crystal microbalance (QCM) has been used to measure the dissolution rate of the resist.[8)] Changes in frequency, according to the Sauerbrey equation, can monitor resist mass loss due to dissolution.[9-13)] QCM also measures the impedance, which reflect the inductive reactance caused by series resonance losses, indicating energy loss during development.[14,15)] Although the impedance has been measured during development,[16,17)] the dynamic relationship between impedance change and dissolution kinetics, including the viscosity changes in the developer caused by resist polymer dissolution, was previously unclear.

Diffusion model has been applied to the analysis of QCM frequency charts to investigate the solvent diffusion in resist films during prebaking.[18] Previous study indicated that the decrease in impedance after the resist dissolution is related to the polymer diffusion in the developer.[19] In this study, the impedance changes during polymer dissolution were simulated based on the diffusion equations. This study demonstrated that the impedance not only provides insights into the rate of resist dissolution but also offers valuable information on the interaction at the dissolution front by reproducing QCM charts.

The QCM method was used to measure the mass and energy loss with change in frequency and impedance, respectively.[18] The mass loss, based on the Sauerbrey equation, has the relationship with the frequency change as follows[9]:

$$\frac{\Delta f}{f_0} \propto \frac{-\Delta m}{m}, \tag{2-1}$$

where Δf, f_0, m, and Δm are the frequency change, resonant frequency, unloaded resonator mass, and mass change. Although there is a clear relationship between frequency change and resist mass loss during the dissolution process, the change in impedance has not yet been successfully reproduced in a manner that provides physical insights. Many dissolution models of polymer films have been proposed.[19-24] However, the dissolution model that can utilize the QCM impedance chart has not been reported. In previous work, the impedance change was found to be related with the polymer concentration and the viscosity of developer.[25] Based on the Stokes–Einstein–Sutherland equation, the viscosity is further converted to the hydrodynamic radius (R_H) of polymers[26]:

$$R_H = \frac{k_B T}{6\pi\eta_S D}, \tag{2-2}$$

where k_B, T, η_s, and D are the Boltzmann constant, the absolute temperature, the dynamic viscosity, and the diffusion constant of polymer, respectively.

2.2 Simulation

In this study, a stratified polymer dissolution model based on the impedance data was proposed. Thereby, the extraction of feature values such as the D and R_H from QCM charts becomes possible. The reported QCM charts of *tert*-butoxycarbonyl (*t*-BOC) protected poly(4-hydroxystyrene) (PHS) films in alkaline aqueous developers[27,28] were analyzed. Additional QCM charts were also obtained in accordance with the experimental procedures reported in previous work.[27,28] The polymer film density is 1.2 g cm^{-3}.[29] The developer used were 0.26 and 0.17 N TMAH aqueous developers and 0.26 N tetraethylammonium hydroxide (TEAH) aqueous developer, which are named 0.26 N TMAH, 0.17 N TMAH, and 0.26 N TEAH, respectively, in this study for convenience.

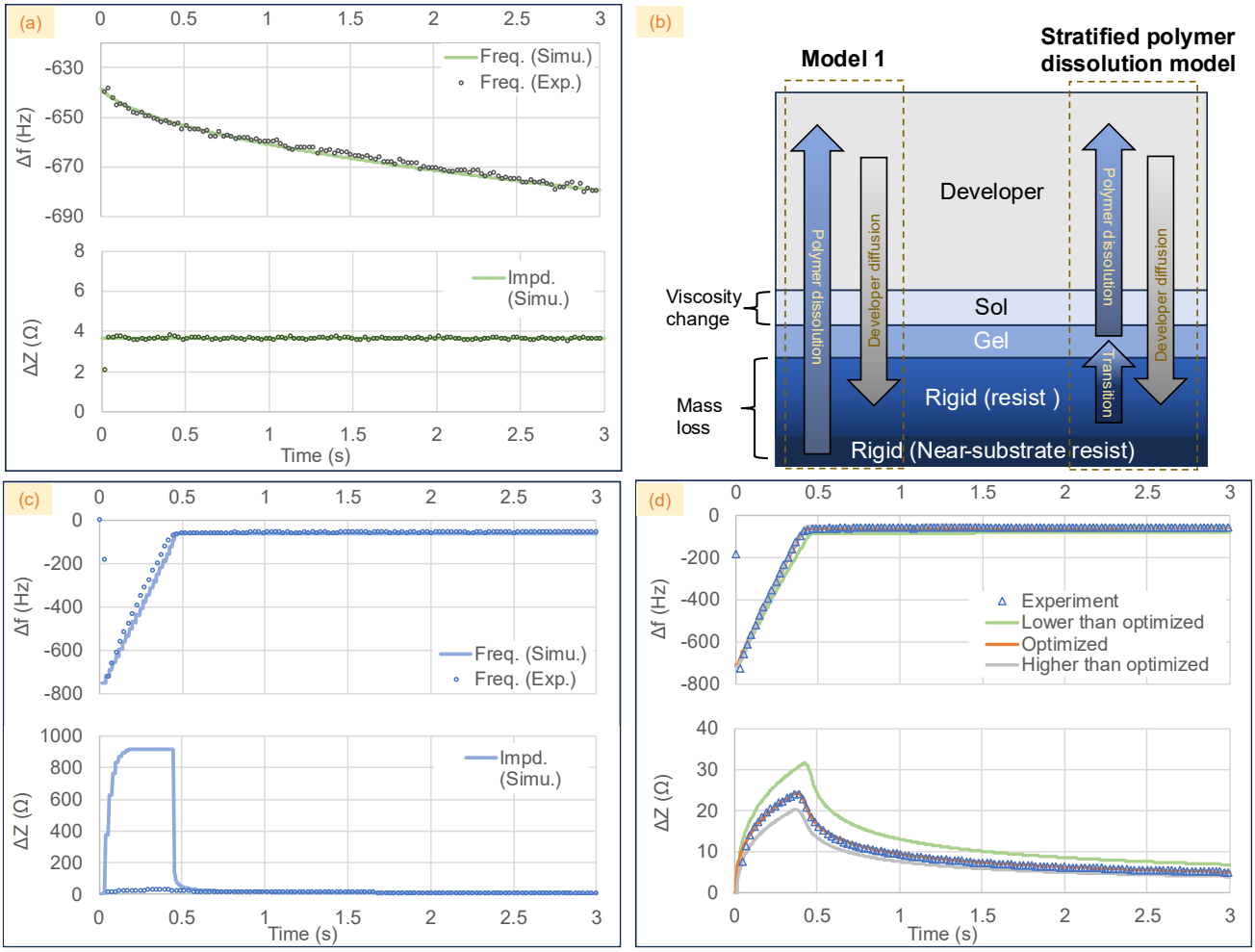

Figure 2-1 (a) QCM chart of 300-nm-thick PHS film immersed in pure water. (b) Schemes of simulation models. (c) QCM chart of 110-nm-thick PHS film immersed in 0.17 N TMAH with simulation result calculated with Model 1. The D_p was 1.2×10^{-10} m^2 s^{-1}. (d) QCM chart of 110-nm-thick PHS film immersed in 0.17 N TMAH with simulation result calculated with SPDM. In (d), the green, orange, and dark gray lines represent the frequency and impedance changes calculated with $D_p = 7\times10^{-11}$, 1.4×10^{-10}, and 2.2×10^{-10} m^2 s^{-1}, respectively. The r_0, β, c_{loss}, and r_{final} were 33 s^{-1}, 3.2 nm^{-3}, 2×10^{-4} s^{-1}, and 1 s^{-1}, respectively. Note that ΔZ represents the impedance change, calculated by subtracting the developer impedance (measured after 60 s, at which the resist polymer is presumed to have fully dissolved) from the impedance measured during development.

For the simulation, the dissolution of polymer was modeled on the basis of diffusion equations. This involves the developer diffusing into the polymer film and the dissolved polymer diffusing into the developer. Detailed simulation models added more parameters are explained in the following sections with Fig. 2-1(b). The dynamics of three components (polymer, water, and alkali) are all simulated based on a diffusion equation:

$$\frac{\partial C}{\partial t} = \frac{\partial}{\partial x}\left(D\frac{\partial C}{\partial x}\right), \tag{2-3}$$

where C and D represent the concentration and diffusion constant of each diffusion component (polymer, water, or alkali). Polymer concentration is expressed in monomer units. t and x are time and the coordinate perpendicular to the surface of QCM substrate. The length of cell for the calculation was set to be 5 nm. The impedance was calculated from the concentration of polymer in the developer, based on the relationship between the viscosity and impedance reported in the previous work in Table 2-I.[25)]

Table 2-I. Solvent viscosity and impedance change measured by inserting QCM substrate to the solvent.[32)]

Solvent	Impedance change (ΔZ; Ω)	Viscosity (mPa s) at 25 °C

Water	255.19	0.890
Methanol	195.35	0.544
Ethanol	276.21	1.074
1-Propanol	377.74	1.945
2-Propanol	386.1	2.04
1-Butanol	451.19	2.54
Ethyl acetate	191.51	0.423
Butyl acetate	233.43	0.685
Amyl acetate	267.9	0.8618
Hexyl acetate	291.88	1.036

The impedances of the developers were plotted, as shown in Fig. 2-2, to calculate the relationship between the viscosity η and impedance change ΔZ. The relationship is given as follows:

$$\eta = 0.0082\,\Delta Z - 1.2104, \tag{2-4}$$

The baseline of the impedance change was the impedance of the QCM substrate in the atmosphere.

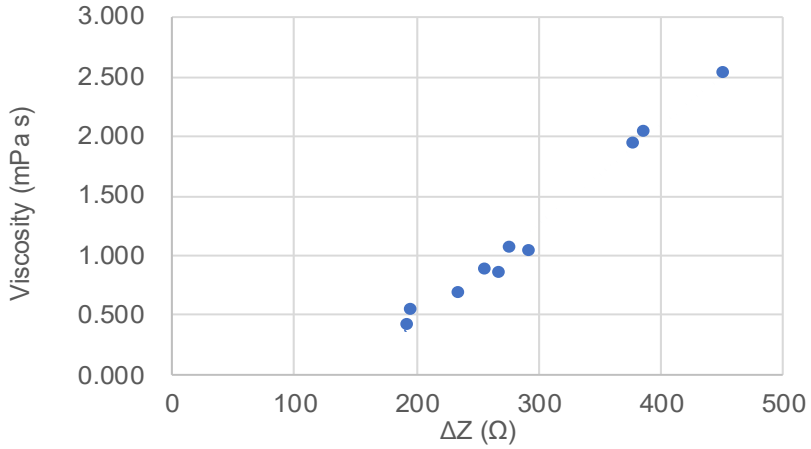

Figure 2-2 The relationship between solvent viscosity and impedance change.

The diffusion constant of developers in the polymer films can be determined by observing the rate in the frequency change at which the resist polymer swells. In this experiment, pure water was used to examine the swelling behavior in a 300-nm-thick polymer film. Figure 2-1(a) illustrates the changes in frequency and impedance within 3 s after the immersion of polymer film in water. The decrease in frequency indicates that water diffused into the polymer. The diffusion constant of water (D_w) was estimated to be 4×10^{-16} m^2 s^{-1}. Meanwhile, there was no significant change in impedance. This indicates that neither film dissolution nor viscosity increase was induced within 3 s after the immersion. The penetration of water only affected the resonance frequency without causing the significant relaxation of polymer matrix. In the following simulation, the diffusion constant of alkali (D_{alk}) in the developer was assumed to be the same as D_w. Note that D_w and D_{alk} were also adjusted from 10^{-16} to 10^{-15} m^2 s^{-1} for each experimental results. D_w tended to increase in the presence of alkali.

2.3 Experiment

Poly(4-hydroxystyrene) (PHS) powder, propylene glycol monomethyl ether (PGME), and tetraethylammonium hydroxide (TEAH) were purchased from Sigma–Aldrich. The 2.38 wt% tetramethylammonium hydroxide (TMAH) developer (NMD-3) was purchased from Tokyo Ohka Kogyo. An RDA-Qz3 (Litho Tech Japan) resist evaluation system, based on the quartz crystal microbalance (QCM) method, was used. The dynamic light scattering (DLS)-based particle size distribution analyzer (nanoPartica SZ-100V2 series, HORIBA) was used. Solutions of polymers (0.05 wt%) in developers were prepared and stored in a refrigerator for approximately one day before measurement using DLS.

The polymer dissolution models are discussed, focusing on understanding how the polymer dissolves into the developer and how the dissolved polymer affects the impedance change. Two types of dissolution models were tested, as illustrated in the schemes shown in Fig. 2-1(b). In Model 1, the resist film was dissolved in accordance with Eq. (2-1). The diffusion constant of polymer in the film was assumed to be the same as that in the developer. The changes in frequency and impedance calculated by assuming Model 1 are illustrated in Fig. 2-1(c).

Although the frequency changes could be roughly approximated, the impedance changes obtained by the simulation were significantly larger than the experimental impedances. This disagreement suggests that the transient swelling layer is thin. The formation of a thick swelling layer would typically result in a sharp increase in impedance. Next, the dissolution model was stratified, with the rigid layer transitioning into the gel layer and then diffusing into the sol layer [Fig. 2-1(b), stratified polymer dissolution model (SPDM)]. The rigid layer represents the solid polymer film that does not affect viscosity change (impedance change) but affects mass change (frequency change). The constant proportionality between frequency and mass changes used in this study is -5.40×10^{18} Hz nm^2 mg^{-1} (Table 2-II).

Table 2-II. Relationship between frequency and mass changes.

TMAH	Thickness	a (Hz nm^2 mg^{-1})
0.26 N	300 nm	-4.46×10^{18}
	100 nm	-4.48×10^{18}
0.17 N	300 nm	-5.22×10^{18}
	100 nm	-5.68×10^{18}

The frequency change depends on the number of polymer molecules in the rigid layer when the transient swelling layer is thin. The following equation is used:

$$\Delta f = a\Delta m, \tag{2-4}$$

where Δf, a, and Δm denote the frequency change, coefficient, and mass change, respectively. The coefficient a was determined from the experimental data relating to the resist thickness and frequency change. To test the frequency change during the dissolution of 100- and 300-nm-thick PHS films, 0.26 and 0.17 N TMAH were used. The coefficient a depended on experimental conditions, ranging from -4.46×10^{18} to -5.68×10^{18} Hz nm^2 mg^{-1}, as shown in Table 2-II. In this study, the average value of -5.40×10^{18} Hz nm^2 mg^{-1} was used.

The gel layer is defined as the resist layer that has absorbed the developer but has not yet dissolved. When the gel layer is thick, it affects the viscosity change. When this layer is thin, it does not affect the viscosity change. The sol layer is the viscous layer that impacts the impedance change during development with thin gel layer. This corresponds to Type 1 dissolution model reported previously.[30] To simulate the rigid layer transitioning into the gel layer, a gelation phase transition rate (r), defined by the number of polymer (monomer unit) converted from rigid phase to gel phase per unit time $\Delta\mathrm{Gel}/\Delta t$ was introduced. The gelation phase transition rate is expressed as

$$r = \frac{\Delta\mathrm{Gel}}{\Delta t} = \frac{r_0}{\beta \cdot C_{\mathrm{gel}} + 1}, \tag{2-5}$$

where r_0, C_{gel}, and β are the initial gelation phase transition rate, the concentration of polymer molecules in gel layer, and a constant. The introduction of $\beta C_{\mathrm{gel}}+1$ is based on a previous observation that the dissolution rate decreased as the polymer continued to dissolve into the developer, due to the increase of viscosity and the decrease in pH near the dissolution interface.[25] With introducing the gelation phase transition rate, SPDM was able to prompt the reproduction of QCM charts, as shown in Fig. 2-1(d), which also demonstrates the effect of polymer diffusion constant (D_{p}). By fitting the simulation kinetics to the experimental impedance chart, D_{p} can be obtained. The impedance charts calculated with the best-fitted D_{p}, along with those calculated with the values larger and smaller than the best fitted D_{p}, were plotted in Fig. 2-1(d). The large D_{p} corresponds to a fast increase in frequency and a low impedance. While this difference was small in the frequency chart, especially when D_{p} was larger than the optimized one, it became clear in the impedance chart.

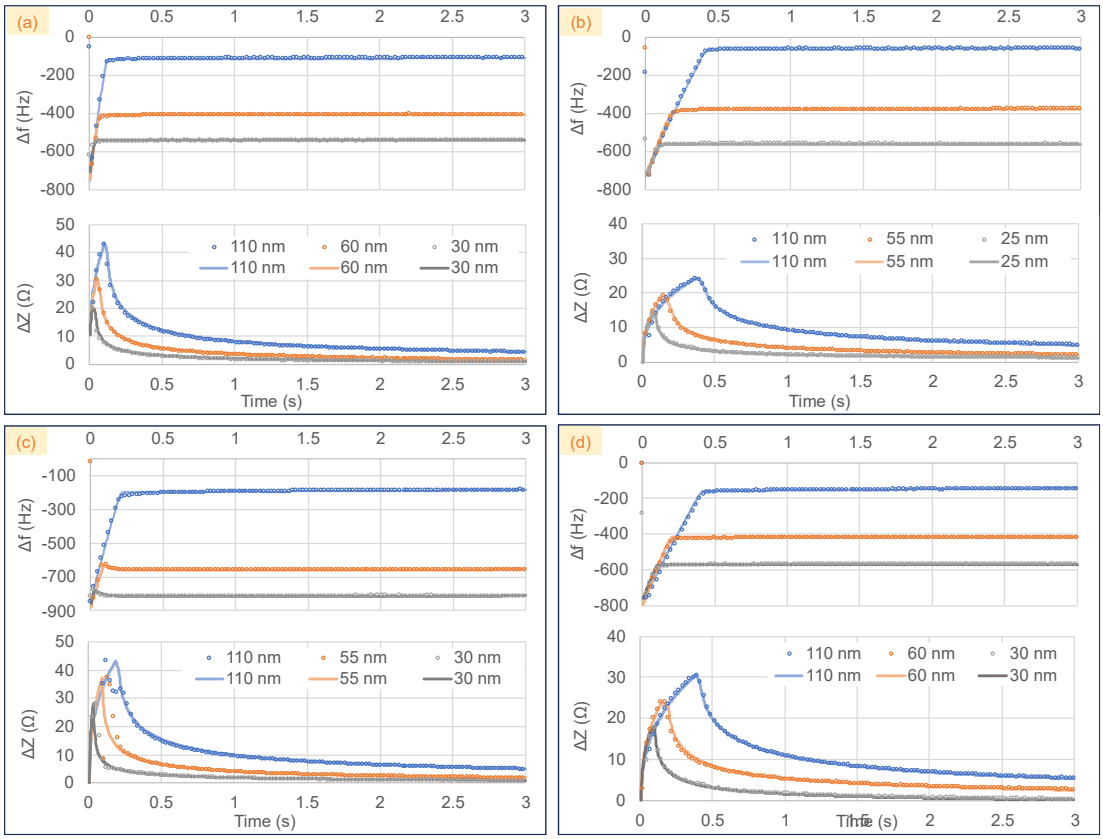

Figure 2-3 QCM charts and fitting results. The experimental data were plotted by dots and simulation data were shown by lines. The development conditions were (a) PHS film in 0.26 N TMAH, (b) PHS film in 0.17 N TMAH, (c) 5 mol% *t*-Boc protected PHS film in 0.26 N TMAH, and (d) PHS film in 0.26 N TEAH.

To investigate how the experimental conditions influence D_p, the effects of polymer, film thickness, and developer were examined. The QCM charts were fitted with SPDM, as shown in Fig. 2-3. An example of dissolution image is shown in Fig. 2-4. Figure 2-4(b) shows a visualization of the simulation results obtained by reproducing the experimental impedance charts shown in Fig. 2-4(a). The dissolution images reflect the state before complete dissolution at 0.08, 0.16, and 0.34 s, and after complete dissolution at 0.6 and 1.0 s. The color change in the sol layer indicates the concentration of the polymer at the dissolution surface, with deeper colors representing a higher polymer concentration.

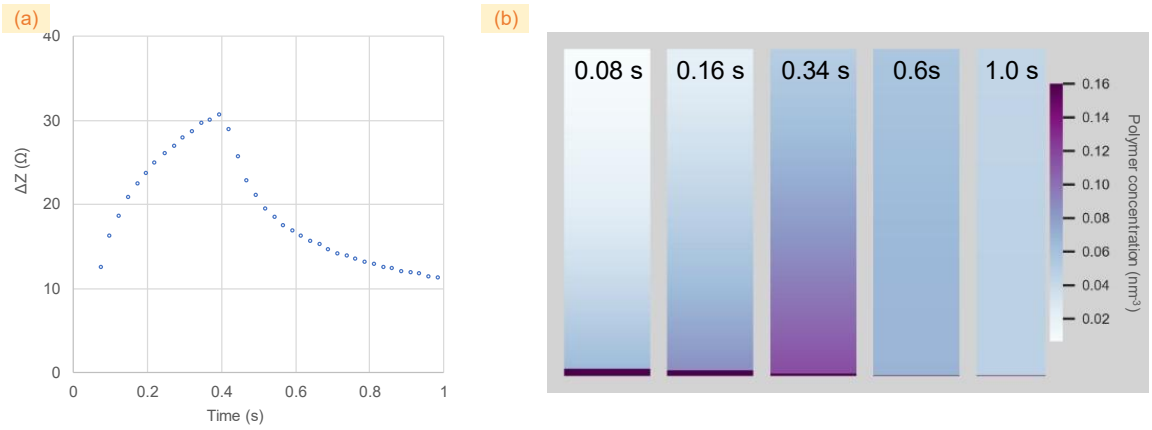

Figure 2-4 (a) Experimental impedance chart obtained during the development of PHS film in 0.26 N TEAH aqueous developer using QCM. (b) Images illustrating the simulated dissolution of polymer molecules. The image depicts polymer distribution within an 800 nm region from the surface of the QCM substrate, while the entire simulated developer region extended to 180 μm. The color bar indicates the concentration of polymer molecules in monomer units.

The best-fitted values are listed in Fig. 2-5. Figure 2-3(a) shows the QCM chart obtained during the development of PHS film using 0.26 N TMAH. When the diluted TMAH (0.17 N) was used, D_p and the impedance reachable during the development significantly decreased, as shown in Figs. 2-5 and 2-3(b), respectively. Close examination of the experimental QCM charts, illustrated in Fig. 2-3(c), reveals that the frequency for the 110-nm-thick film slowly increased after the rapid increase, indicating a decrease in mass. This suggests the existence of a thin layer at the bottom, which was named a near-substrate layer. This unique frequency pattern became remarkable for 55- and 30-nm-thick films shown in Fig. 2-3(c). These observations suggest that after most of the resist film has dissolved, residual polymer molecules remain on the substrate, dissolving at slow rate. To better simulate these phenomena, the model was further refined by incorporating additional parameters: a decrease in the gelation phase transition rate (r_d) that begins approximately 15 nm from the substrate, and a final loss rate (r_{final}). With these adjustments, the model successfully replicated the changes in frequency and impedance shown in Fig. 2-3(c).

Entry (Fig.)	Developer	*t*-Boc (mol%)	Thickness (nm)	D_p (10^{10} m^2 s^{-1})	r_0 (s^{-1})	β (nm^{-3})	r_d (10^3 s^{-1})	r_{final} (s^{-1})	R_H (nm)
1 (2a)	0.26 N TMAH	0	110	1.93	98	1.8	1.45	2	0.97
			60	1.87	98	2.3	1.4	1	1.02
			30	1.84	85	2.6	1.35	1	1.01
2 (2b)	0.17 N TMAH	0	110	1.40	33	3.3	0.2	2	1.40
			55	1.34	32.5	2.1	0.2	2.2	1.49
			25	1.29	30.4	1.5	0.22	2.2	1.56
3 (2c)	0.26 N TMAH	5	110	0.65	59	1.22	8	4.75	2.70
			55	0.425	57.5	1	100	0.75	3.93
			25	0.56	60	1	175	0.5	3.02
4 (2d)	0.26 N TEAH	0	110	0.605	26	1.58	2.6	4.7	3.11
			60	0.71	30.5	1.35	1.7	3.2	2.59
			30	0.593	28.5	1.05	1.05	2	2.97

Figure 2-5 Extracted feature values.

In Fig. 2-5, the extracted feature values are categorized into three ranges: large, middle, and small, highlighted in light green, light purple, and blue colors, respectively. This color coding visualizes the variations across different experimental conditions and their effects on the D_p and r_0. From the data presented, the impact of developers and polymers on D_p and dissolution rates can be observed. Entry 1 shows the fastest dissolution rates, indicated by the highest values of D_p and r_0. When developers are changed while using the same polymer, varied reductions in D_p can be observed. The value of r_0, which indicates the dissolution rate of the polymer, suggests that TEAH developers require more development time. This prolonged development time correlated with a lower impedance change, as evidenced by the comparisons between Figs. 2-5(a) and (d). Entry 3 demonstrates a significant drop in D_p by the *t*-Boc protection, leading directly to the appearance of a bump at the turning point for film thicknesses of 55 and 30 nm.

This bump suggests that a considerable amount of residual polymer remains on the substrate. Moreover, to reproduce the bump at the turning point after most films were dissolved, high values of the loss rate (r_d) were required, suggesting a strong interaction between the polymer and the substrate. Additionally, Entry 4 highlights a decrease in the dissolution rate when the developer was switched to TEAH, indicating the alkali chain of the developer have significant influence on the dissolution kinetics. This comprehensive analysis helps understanding the intricate relationship between polymer and developer and their collective impact on lithographic processing outcomes. Based on Eq. (2-2), the calculated R_H in the TMAH and TEAH solutions was approximately 1–4 nm. R_H of polymers in the developers was also measured using dynamic light scattering (DLS) (Table 2-III) for the validation. R_H and D_p obtained by QCM approximately agreed with those obtained by DLS. According to the DLS data, the R_H of the polymer was approximately 1.3–2.1 nm, and the corresponding D_p was approximately 2.83–1.03 × 10^{-10} m^2 s^{-1}.

Table 2-III. Hydrodynamic radius and diffusion constant of polymers measured by DLS. Polymer concentration was 0.05 wt%.

Developer	*t*-Boc	Viscosity (mPa s) at 23 °C	Hydrodynamic radius (R_H; nm)		Diffusion constant (10^{10} m^2 s^{-1})
			Average	σ	
0.26 N TMAH	0	1.143	1.3	0.75	2.83
0.17 N TMAH	0	1.143	1.6	0.75	1.48
0.26 N TMAH	5	1.143	1.4	0.5	1.11
0.26 N TEAH	0	1.159	2.1	1.0	1.03

2.4 Conclusion

The QCM method, which detects mass loss and swelling of resist polymers, has been extensively used to monitor the dissolution of resist films. The SPDM, based on the diffusion function principles, well reproduced the QCM charts. This layered dissolution kinetic suggests that even when the difference in mass change pattern during dissolution is small, the viscosity near the dissolution interface can differ significantly. This variability in viscosity is critical to understanding the dynamics in dissolution. Furthermore, the simulation model includes feature values that quantify the dissolution characteristics of different developers and polymers, providing physical insights into the dissolution process. Experimental data have revealed residual polymer near the substrate, highlighting the interactions between the polymer and the substrate. The analysis of these residuals helps to estimate the amount of residue and its absorption capacity of the developer. This study enhances the understanding of dissolution kinetics from the perspective of reproducing frequency and impedance charts. It also opens avenues for exploring new developers by providing a methodological framework to study their effectiveness.

2.5 References

1) H. Ito, Microlithography/Molecular Imprinting Advances in Polymer Science Series (Springer, Heidelberg, 2005) Vol. 172, p. 37.

2) K. Azumagawa and T. Kozawa, Jpn. J. Appl. Phys. **59**, 076501 (2020).

3) Y. Jin, T. Kozawa, and T. Tamura, Jpn. J. Appl. Phys. **60**, 076509 (2021).

4) Y. Kawai, A. Otaka, A. Tanaka, and T. Matsuda, Jpn. J. Appl. Phys. **33**, 7023 (1994).

5) J. Nakamura, H. Ban, K. Deguchi, and A. Tanaka, Jpn. J. Appl. Phys. **30**, 2619 (1991).

6) L. Schlegel, T. Ueno, N. Hayashi, and T. Iwayanagi. J. Vac. Sci. Technol. B **9**, 278(1991).

7) P. P. Naulleau, C. N. Anderson, L.-M. Baclea-an, P. Denham, S. George, K. A. Goldberg, G. Jones, B. McClinton, R. Miyakawa, S. Rekawa, and N. Smith, Proc. SPIE **7972**, 797202 (2011).

8) T. Kozawa and S. Tagawa, Jpn. J. Appl. Phys. **49**, 030001 (2010).

9) K. Azumagawa and T. Kozawa, Jpn. J. Appl. Phys. **60**, SCCC02 (2021).

10) B. Shahriari, K. Swersky, Z. Wang, R. P. Adams, and N. D. Freitas, Proc. IEEE, **104**, 148 (2016).

11) P. I. Frazier and J. Wang, Bayesian optimization for materials design, in Information Science for Materials Discovery and Design eds. T. Lookman, F. J. Alexander, and K. Rajan (Springer Nature, Switzerland, 2015) pp. 45-75.

12) T. Ohashi, T. Sekiguchi, A. Yamaguchi, J. Yanaka, and H. Kawada, J. Micro/Nanolith. MEMS MOEMS **14**, 034001 (2015).

13) H. Kawada, T. Kawasaki, J. Kakuta, M. Ikota, and T. Kondo, Proc. SPIE **10585**, 1058526 (2018).

14) K. Natsuda, T. Kozawa, K. Okamoto, and S. Tagawa, Jpn. J. Appl. Phys. **45**, L1256 (2006).

15) K. Natsuda, T. Kozawa, K. Okamoto, and S. Tagawa, Jpn. J. Appl. Phys. **46**, 7285 (2007).

16) T. Kozawa, Jpn. J. Appl. Phys. **54**, 056501 (2015).

17) T. Fukuyama, T. Kozawa, S. Tagawa, R. Takasu, H. Yukawa, M. Sato, J. Onodera, I. Hirosawa, T. Koganesawa, and K. Horie, Appl. Phys. Express **1**, 065004 (2008).

18) T. Kozawa and S. Tagawa, Jpn. J. Appl. Phys. **50**, 030209 (2011).

19) H. Yamamoto, T. Kozawa, A. Nakano, K. Okamoto, Y. Yamamoto, T. Ando, M. Sato, H. Komano, and S. Tagawa, Jpn. J. Appl. Phys. **43**, L848 (2004).

20) Y. Ikari, K. Okamoto, A. Konda, T. Kozawa, and T. Tamura, Jpn. J. Appl. Phys. **59**, 086506 (2020).

21) W. D. Hinsberg, F. A. Houle, M. I. Sanchez, and G. M. Wallraff, IBM J. Res. Dev. **45**, 667 (2001).

22) H. Fukuda, K. Hattori, and T. Hagiwara, Proc. SPIE **4346**, 319 (2001).

23) T. Kozawa, Jpn. J. Appl. Phys. **54**, 016502 (2015).

24) W. Hinsberg, F. A. Houle, S.-W. Lee, and H. Ito, Macromolecules, **38**, 1882 (2005).

25) T. Kozawa, H. Oizumi, T. Itani, and S. Tagawa, Appl. Phys. Express **3**, 036501 (2010).

26) T. Kozawa, H. Oizumi, T. Itani, and S. Tagawa, Jpn. J. Appl. Phys. **49**, 066504 (2010).

27) T. Kozawa, H. Oizumi, T. Itani, and S. Tagawa, Jpn. J. Appl. Phys. **49**, 116505 (2010).

28) T. Kozawa, H. Oizumi, T. Itani, and S. Tagawa, Jpn. J. Appl. Phys. **50**, 076503 (2011).

29) T. Kozawa, H. Oizumi, T. Itani, and S. Tagawa, Jpn. J. Appl. Phys. **50**, 126501 (2011).

30) T. Kozawa, J. J. Santillan, and T. Itani, Appl. Phys. Express **6**, 026502 (2013).

31) T. Kozawa, Jpn. J. Appl. Phys. **55**, 056503 (2016).

32) Y. T. Ito, K. Watanabe, Y. Jin, T. Kozawa, K. Sakamoto, and M. Muramatsu, Jpn. J. Appl. Phys. **63**, 018002 (2024).

Chapter 3: Analysis of resist images with pattern defects by Hough transform

Chapter Overview

This chapter focuses on the inspection of the final resist pattern, as illustrated in Fig. 2(g) of the *General Introduction* chapter. From a machine learning perspective, it introduces a novel evaluation method for quantifying defective patterns, enabling even severely defective ones to be datafied and used as target variables in model training. This approach addresses the challenge of incorporating low-quality pattern data into predictive models, thereby enhancing the robustness and applicability of the machine learning framework. By complementing the chemical parameter extraction methods presented in earlier chapters, this chapter completes the process chain from fabrication to performance assessment, providing a comprehensive foundation for end-to-end modeling of resist pattern formation.

3.1 Introduction

The heart of the semiconductor lies within its manufacturing process, where the critical components are the materials used, and the equipment employed to facilitate production. The introduction of extreme ultraviolet (EUV) light source with a wavelength of 13.5 nm has enabled the manufacturing of features with smaller sizes.[1)] However, this technology has also highlighted challenges brought by smaller feature sizes, namely, the stochastically generated defects on resist patterns.[2-7)] Line-and-space (L/S) patterns are important design features with numerous applications, including the manufacturing of microprocessors and memory chips. Defects can arise on L/S patterns for a variety of reasons during the lithography process.[8)] In order to minimize these defects, it is crucial to optimize and control the lithography process, but it is equally important to focus on the development of resist materials.

Chemically amplified resists (CARs)[9] are promising for high-resolution lithography, with their solubility change primarily influenced by the protection ratio of the polymer matrix following exposure and post-exposure baking (PEB) process. The sensitivity (sizing dose) of CARs is strongly related to the chemical gradient, indicating defect severity in the resist pattern.[8] Previous studies on electron beam (EB)[10] and EUV[8] printing have suggested that various factors during the printing process can cause defects in the CAR-type resist. Consequently, results obtained from patterns with defects are often more informative than those without defects. However, evaluating patterns with severe defects can be difficult due to the stochastic nature of defect generation. Furthermore, comparing different defected patterns is challenging due to the variability of the defects.

On the other hand, the acid-catalyzed deprotection process that occurs during PEB is one of the most crucial processes in controlling the feature size of a resist film. The presence of stochastic effects including interactions between electrons and materials, secondary electron emission, and chemical reactions, that can have an impact on the distribution of protected units, making uniformity a critical factor to consider.[11] When focusing on the underlying chemistry, the issue becomes chemical parameters, such as the effective reaction radius for the deprotection reaction (R_p), which is important but difficult to determine.[12,13] To address the issues mentioned above, this study proposed a novel method for evaluating L/S patterns with defects based on Hough transform. The Hough transform is an image processing technique used for detecting fundamental geometric shapes such as lines and circles within an image.[14] This method evaluates the pattern as a whole and automatically measures the average line width (LW) and interval distance, which is defined later. Further analysis of the measurement enables the description of defectivity in the resist pattern and the distinction between different types of defects. To further apply this method to the insight chemistry, the simulation results were compared with the experimental results by changing the R_p, in order to explore the pattern changes that could be brought about by varying this chemical parameter. In this study, the frequency dependence of line edge roughness (LER) is not discussed, because it is only applicable to fine patterns without defects. The ecellent works for the analysis of frequency dependence in fine patterns have been already reported.[15,16]

3.2 Experiment

In this experiment, a chemically amplified resist[9] was utilized, consisting of a polymer film composed of a synthesized copolymer of poly(4-hydroxystyrene) (PHS) and poly[4-(tert-butoxycarbonyl)oxy-styrene] (PTBS) with a molecular weight of 12700. The hydroxyl groups of PHS were protected with the tert-butoxycarbonyl (t-BOC) group (54.6 mol%), resulting in a protected unit concentration of 2.26 (units)/nm^3 under the film condition. A polymer powder of approximately 3 wt% was dissolved in propylene glycol monomethyl ether acetate (PGMEA), to which triphenylsulfonium nonaflate (TPS-nf) and a quencher, trioctylamine (TOA), were added, with their concentrations adjusted to 0.2 and 0.1 (molecules)/nm^3 under the film condition, respectively. Spin coating was carried out on a 4-inch Si wafer at 1000 rounds per minute (rpm) for 3 s, followed by a gradual increase in speed with a slope of 20 s until reaching 4000 rpm, which was maintained for 30 seconds. Subsequently, the wafer was pre-baked at 90°C for 90 s. The thickness of the resist was measured to be 55 nm using an ellipsometer (Meiwafosis FS-1). The sample was stored in vacuum at room temperature before exposure to a 125 keV EB (Elionix ELS-100T) at doses ranging from 192 to 320 μC/cm^2 with an EB current of 100 pA. L/S patterns with pitches of 70, 80, 90, 100, 110, and 120 nm were used. To examine the reproducibility, a total of 16 chips with the same set of patterns were printed on the same wafer. After EB exposure, the resist was subjected to PEB at 110 °C for 1.5 min. Development was carried out by soaking the resist in a 2.38 wt% tetramethylammonium hydroxide (TMAH) aqueous developer (Tokyo Ohka Kogyou NMD-3) at 23 °C for 30 s, followed by rinsing with pure water for 15 s.

SEM images of the resist were obtained using the Hitachi High-Tech Advanced CD Measurement SEM CS4800 with an acceleration voltage of 800 V and a probe current of 8.0 pA. The images were taken at a magnification of 20,000 and 100,000 at the addressing point and measurement point, respectively. The image size is 512 × 512 pixels. To minimize potential damage to the resist patterns caused by SEM observation, the acceleration voltage and number of electrons were reduced. Specifically, the emission current, frame integration (64), and

acceleration voltage were lowered while still maintaining observable images. It should be noted that SEM observation can cause the shrinkage of the resist patterns.[17,18] To reduce this effect, previous studies have suggested minimizing the number of electrons and acceleration voltage used during SEM imaging.[17] The SEM results for one of the 16 chips were presented in supporting information (Fig. 3-1 and Table 3-I).

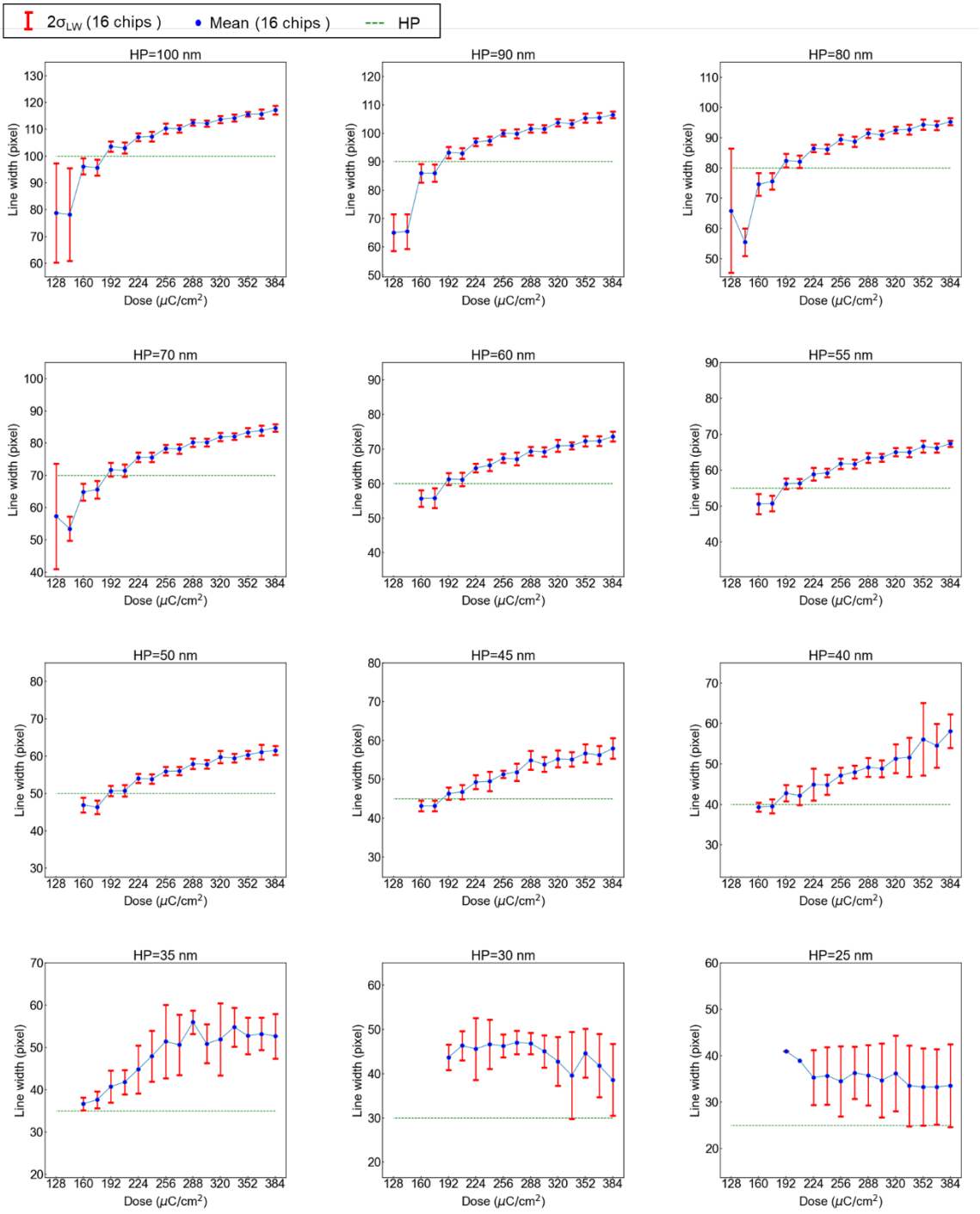

(a)

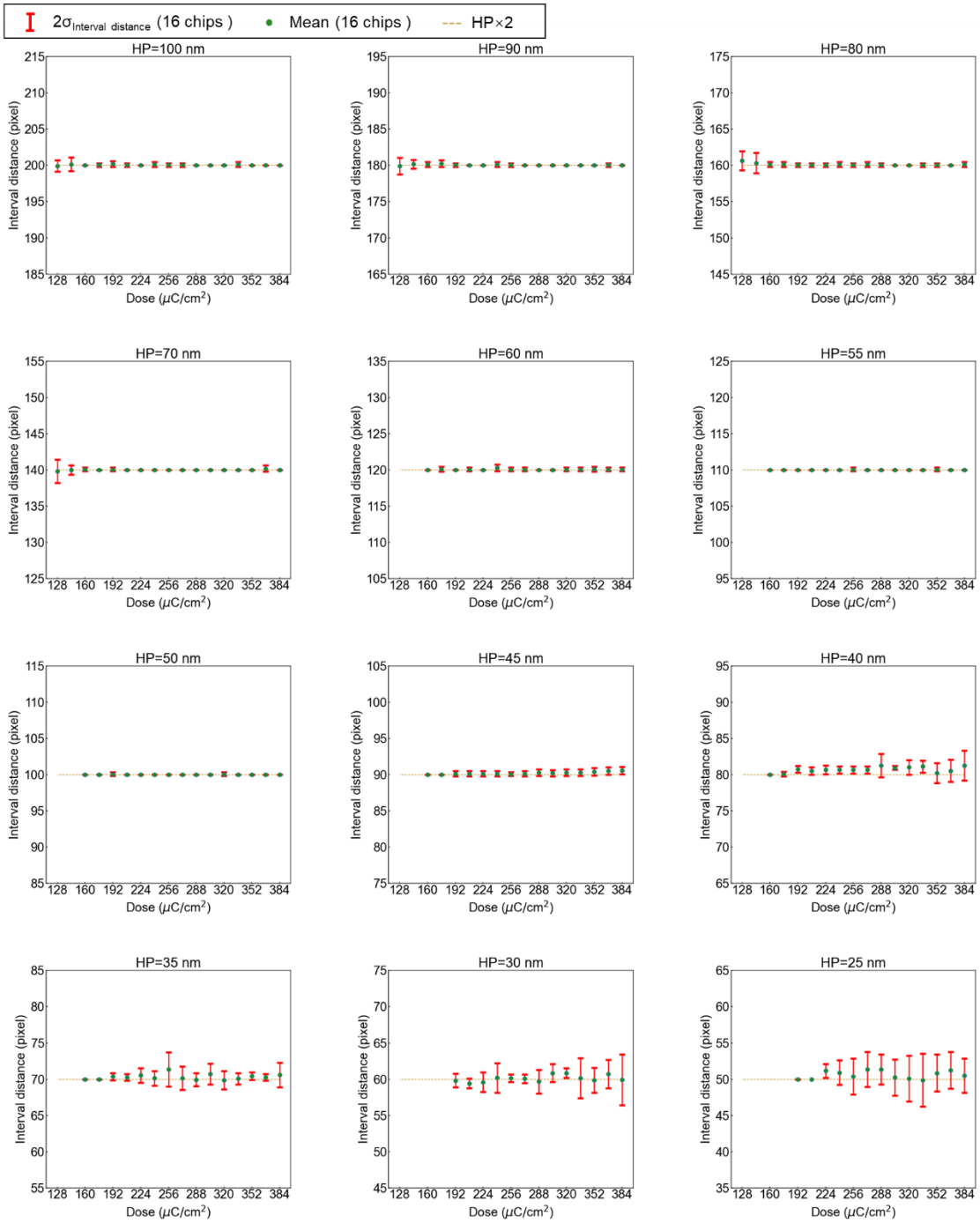

(b)

Figure 3-1 Dose dependence of (a) LW and (b) interval distance. The data were collected from a single wafer consisting of 16 chips with identical pattern sets.

The LW and interval distance were plotted in different graphs for each half-pitch (HP). The LW and interval distance were measured from each SEM image and their mean values and standard deviations were calculated. The LW and interval distance were then plotted against dose. The LW was measured using the Hough transformation followed by analyzing the vote distribution method, where the peak of the distribution plane represents the mean LW value for each pattern from the 16 chips. The green dashed lines in (a) and (b) are the designed HP and interval distance, respectively. The blue dots in (a) represent the mean values, while the red error bars indicate the standard deviations for the 16 chips. Similarly, the interval distance was also measured using the vote distribution method, and the mean values and standard deviations were plotted against dose in (b).

The LW and interval distances were measured using the method described in section 3.5. The length of the error bars indicates the variation among 16 chips under the experimental conditions outlined in the this section. Differences in error bar length between fine and defected patterns can also be observed in Fig. 3-1(b). Defected patterns at low doses (HPs of 70-100 nm) and high doses (HPs of 25-40 nm) exhibit longer error bars than those of fine patterns. Thus, these figures can provide information about pattern stability and resolution (which is 45 nm in this case) based on the length of the error bars for both LW and interval distance measurements. Note that some patterns were not formed due to low dose and small feature size, and unable to be observed by SEM.

Table 3-I. SEM images of resist patterns in chip 1 among 16 chips on the 4-inch wafer. The units of HP and dose are nm and μC/cm^2, respectively.

Dose \ HP	100	90	80	70	60	55
112						
128	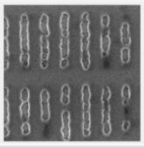	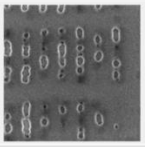				
144	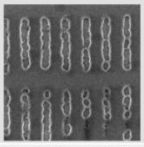	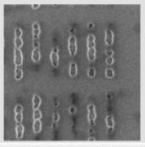				
160	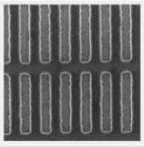	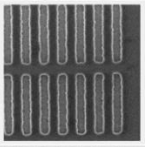	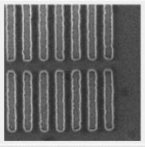	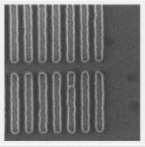	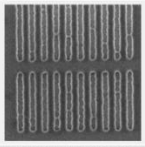	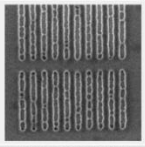
176	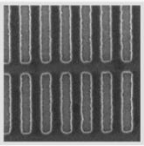	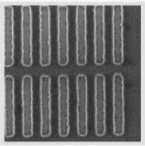	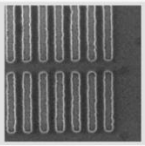	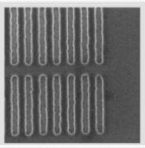	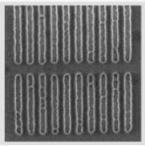	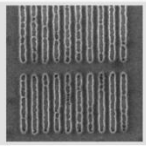
192	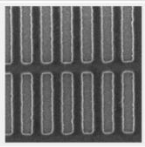	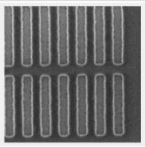	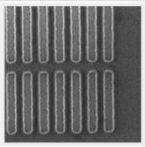	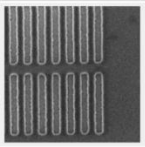	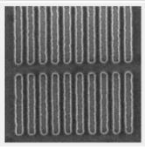	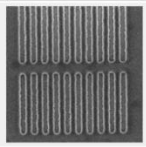
208	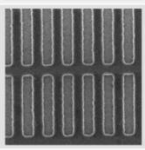	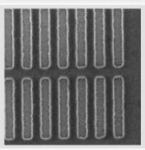	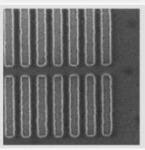	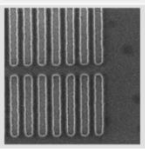	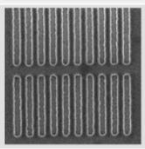	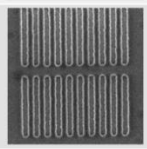
224	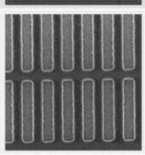	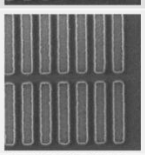	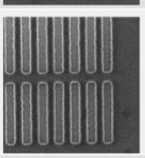	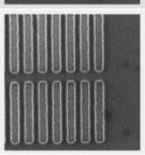	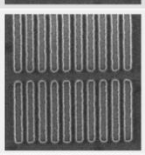	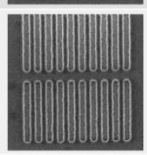
240	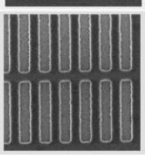	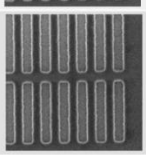	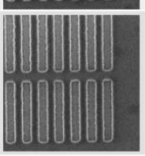	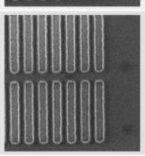	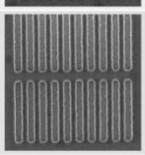	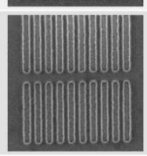

Dose \ HP	100	90	80	70	60	55
256	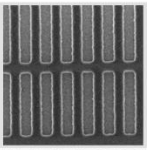	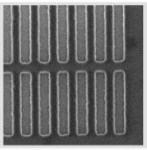	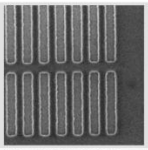	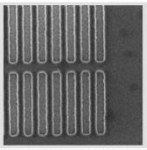	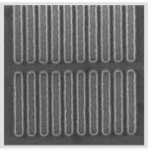	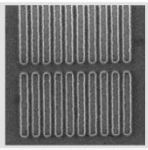
272	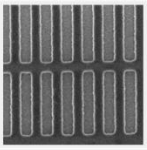	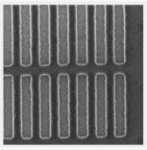	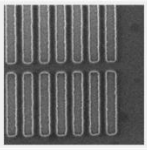	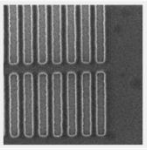	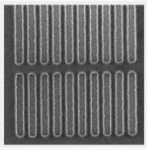	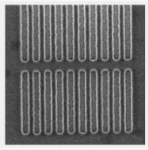
288	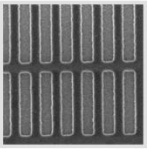	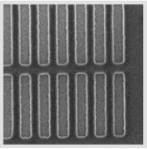	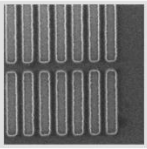	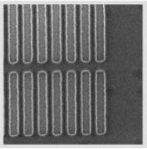	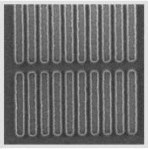	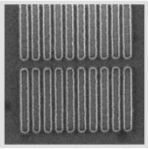
304	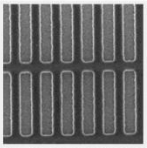	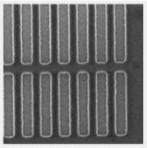	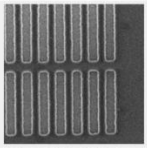	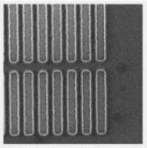	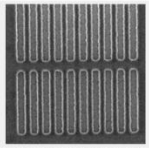	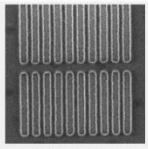
320	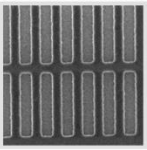	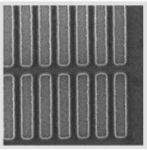	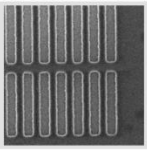	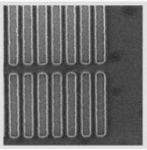	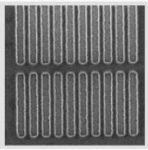	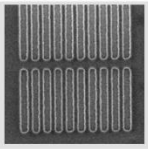
336	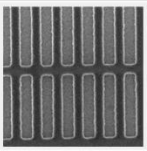	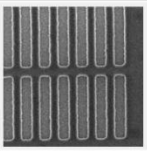	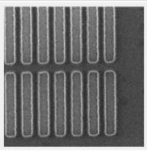	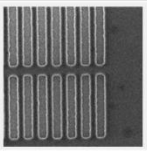	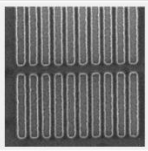	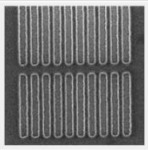
352	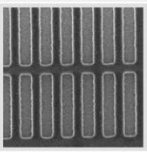	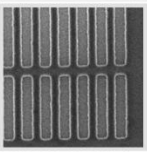	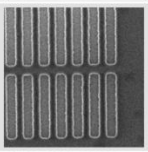	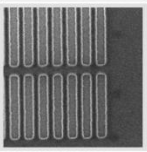	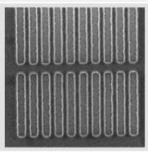	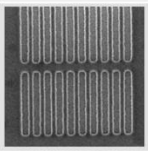
368	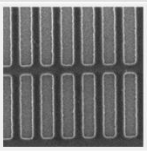	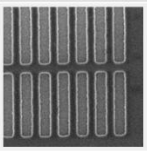	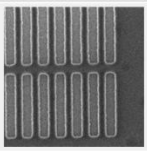	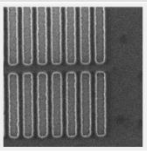	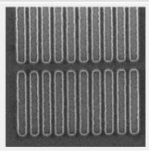	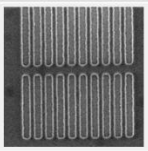
384	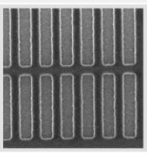	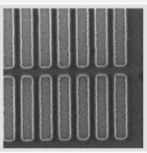	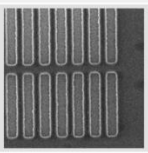	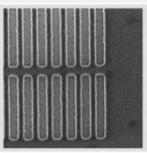	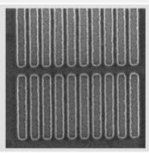	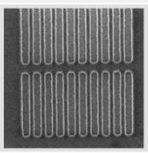

Dose \ HP	50	45	40	35	30	25
112						
128						
144						
160	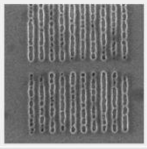	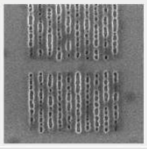				
176	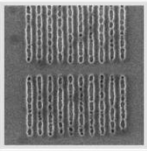	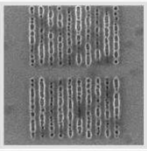				
192	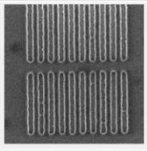	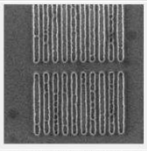	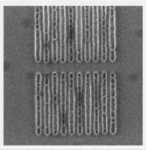	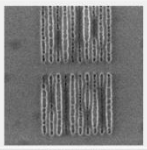		
208	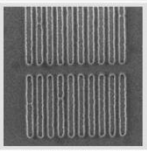	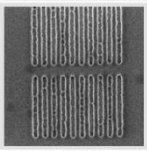	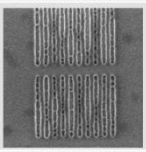	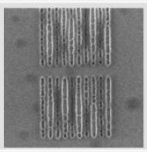		
224	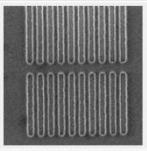	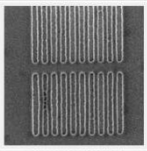	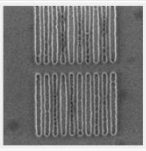	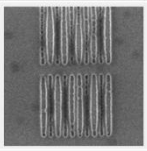	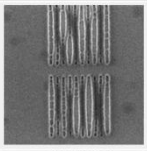	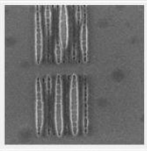
240	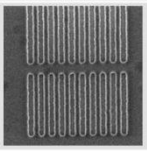	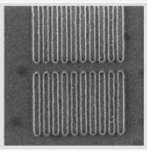	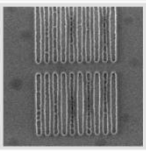	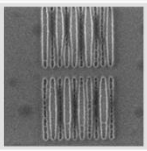	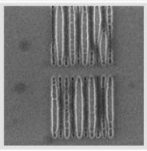	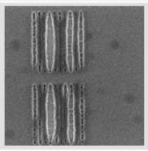

Dose \ HP	50	45	40	35	30	25
256	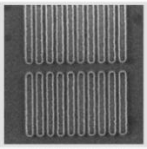	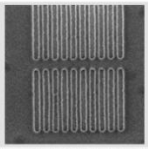	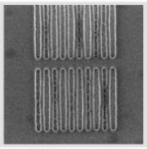	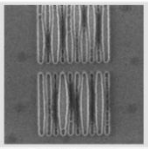	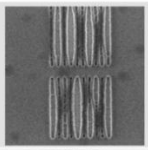	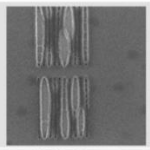
272	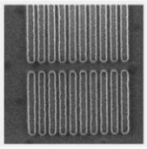	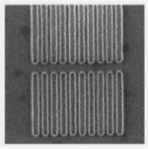	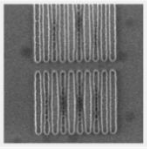	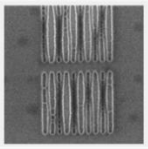	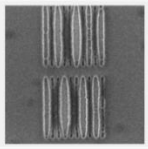	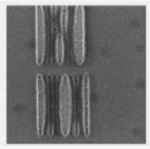
288	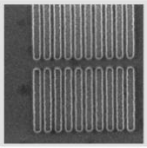	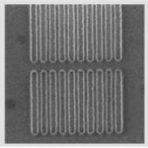	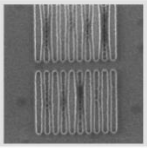	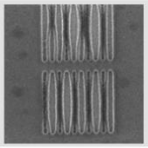	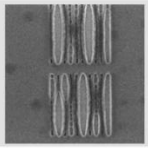	
304	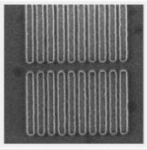	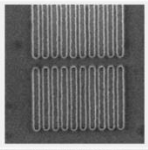	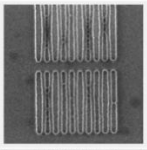	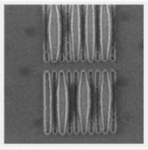	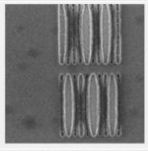	
320	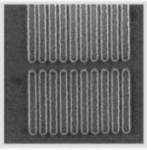	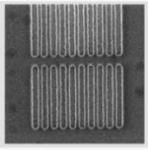	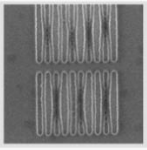	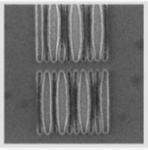	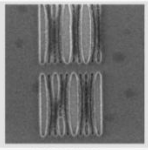	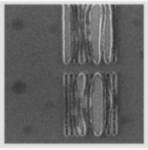
336	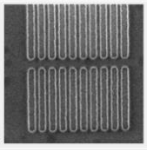	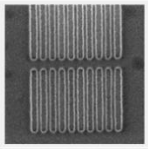	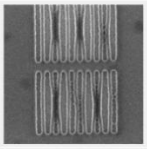	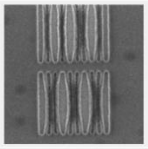	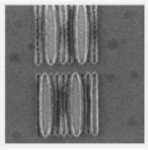	
352	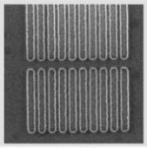	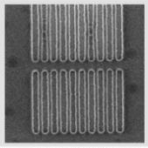	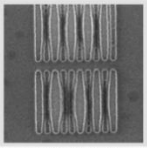	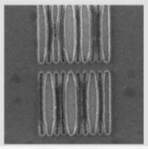	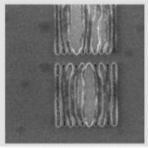	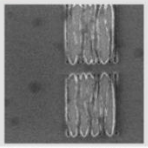
368	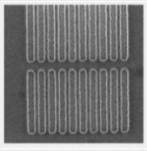	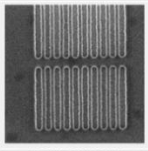	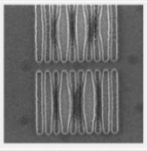	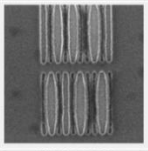	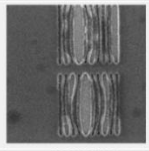	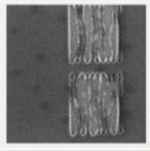
384	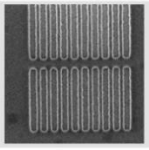	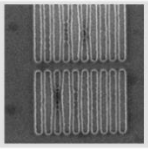	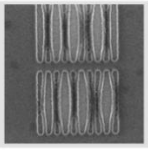	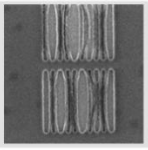	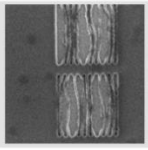	

3.3 Simulation model

The decomposition of TPS-nf and the subsequent deprotection of polymer were simulated by a Monte Carlo method to obtain the distribution of acids and protected units. After simulating TPS-nf decomposition during EB exposure, as described previously, the preneutralization of acids before PEB[19,20] was calculated with the proton migration range of 2.4 nm.[21] Using the acid distribution after the preneutralization as the initial condition, the catalytic chain reaction during PEB was calculated by a Monte Carlo method. The motion of the acid and quencher molecules at each time step dt is given by $\sqrt{6D\mathrm{d}t}$, where D represents the diffusion constant of the acid or quencher molecule. The direction of motion was determined using uniform random variables. During PEB processes, when the acid molecule reached a quencher molecule within the effective reaction radius for neutralization, the acid molecule was regarded to be lost through neutralization. When the acid molecule reached a protected unit of the polymer within the effective reaction radius for deprotection R_p, the acid molecule was regarded to induce the deprotection of the polymer. The other details of simulation method have been described elsewhere.[22,23] The simulation parameters used are listed in Table 3-II.[24-28] To denoise the result drawn from Mote Carlo simulation, a simple model for the polymer aggregation simulation followed by dissolution judgment was simulated.

Table 3-II. Parameters used in simulation.

Acceleration voltage of electron beam (kV)	125
Beam blur (σ_b) (nm)	2.0
Resist thickness (nm)	20
Stopping power (eV/nm)[24]	0.418
Resist film density (g/cm^3)[25]	1.2
Thermalization distance (nm)[26]	3.2
PAG concentration (/nm^3)	0.2
TOA concentration (/nm^3)	0.1

Reaction radius of PAG (nm)[26]	0.70
Effective reaction radius for neutralization (nm)	0.5
R_p (nm)	0.06, 0.16
Protection ratio (mol%)	54.6
Deprotonation efficiency of proton source[27]	1.0
Deprotonation efficiency of nonproton source[28]	0.59
Acid generation efficiency[28]	0.87
Diffusion constant of acids (nm^2/s)	1.0
Diffusion constant of quenchers (nm^2/s)	1.0
Diffusion constant of protected units (nm^2/s)	0.0
PEB time (s)	90
HP (nm)	45
Dose ($\mu C/cm^2$)	192

3.4 Analytical methods

3.4.1. Edge dectection

As the first step toward L/S patterns in resist images, the edges of lines are detected using Laplacian of Gaussian (LoG) filter. The LoG is a type of image enhancement filter that is commonly used in computer vision and image processing applications. It enhances the edges of an image by convolving it with a kernel that is the product of a Laplacian kernel for edge detection and a Gaussian kernel for smoothing. In the LoG kernel, the center of the kernel is defined as the origin which corresponds to an interest in pixel, and then the weight of each pixel, represented by its coordinates x and y, is calculated based on its distance from the center using the following formula:

$$LoG(x,y) = \left(\frac{x^2+y^2-2\sigma^2}{2\pi\sigma^6}\right) e^{-\frac{x^2+y^2}{2\sigma^2}}, \quad (3\text{-}1)$$

where σ represents the standard deviation in Gaussian kernel. The LoG kernel can then be used to convolve with an image.

In this experiment, both SEM images and simulated resist pattern images were processed using LoG filter. However, to detect the edges of the lines, different operations were applied to the SEM images and the simulation results by considering the different properties between them. Because line patterns in the SEM images are observed as thick and blurry line segments (i.e., regions) and they are brighter than the other regions as shown in Fig. 3-3 (a), ridges of the line segments need to be detected. The line segments in the SEM image and the LoG kernel are convex upward and downward in intensity space, respectively, the line segments in the convolved image get convex downward. Therefore, the ridges of the line segments correspond to the local minimum in the convolved images, and hence non-minimum suppression (NMS) was applied to the convolved images to remove unnecessary edges. Specifically, the NMS filters out pixels whose intensity is greater than neighboring pixels' intensities and above a threshold. In order to detect horizontal and vertical line segments, the NMS is applied horizontally and vertically, respectively. On the other hand, line patterns in the simulation results are observed as simple edges, i.e., boundary between bright and dark regions, a conventional edge detection method, i.e., zero-crossing detection on the convolved image with the LoG kernel is employed.

3.4.2. Hough transform

Hough transform is an image processing technique for detecting basic geometric objects, such as circles and lines.[29-32] The Hough transform for straight line detection converts pixel coordinate (x, y) of the detected edges in an image to a straight-line parameter space (ρ, θ) using the following equation.

$$\rho = x\cos\theta + \mathrm{y}\sin\theta \tag{3-2}$$

In Eq. (3-2), ρ denotes the perpendicular distance from the origin to the straight line, and θ represents the angle between the x-axis and the perpendicular line that connects the origin to the straight line. This parameter space is commonly referred to as Hough space.

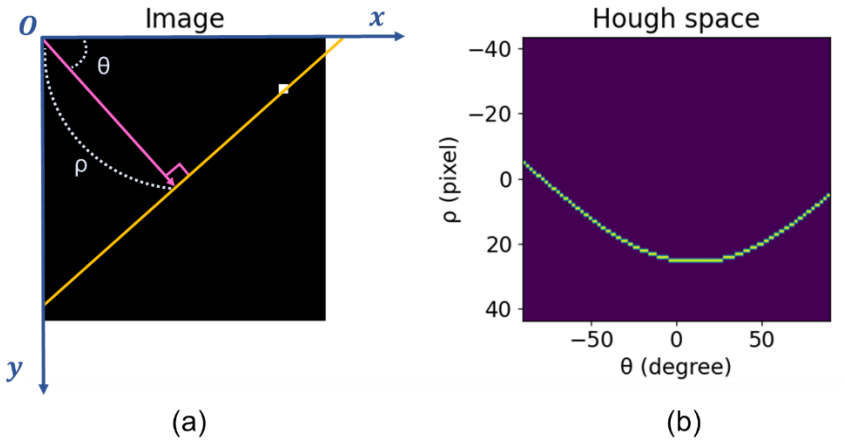

Figure 3-2 (a) Image represented in a coordinate system with its origin at the top left corner and (b) Hough space derived from Eq. (3-2), which corresponds to the white pixel in (a). The image in (a) contains a white pixel, and a yellow straight line passes through it. A pink arrow, starting from the origin, is drawn perpendicular to the yellow line. The length of the pink arrow is denoted by ρ, while the angle between the pink arrow and the x-axis is represented by θ. On the coordinate plane in (b), the horizontal axis represents θ (in degrees) while the vertical axis represents ρ (in pixels). The range of θ is calculated from 90° to -90°.

Figure 3-2(a) illustrates an example of a straight line passing through a pixel in an image, which can be represented by a pair of ρ and θ. Multiple straight lines can pass through the same pixel, and each of these lines can be represented by a unique pair of ρ and θ. Therefore, based on Eq. (3-2), each pixel in the image can be converted into a trigonometric function curve. In this particular case, the white pixel in Fig. 3-2(a) was converted to the Hough space shown in Fig. 3-2(b).

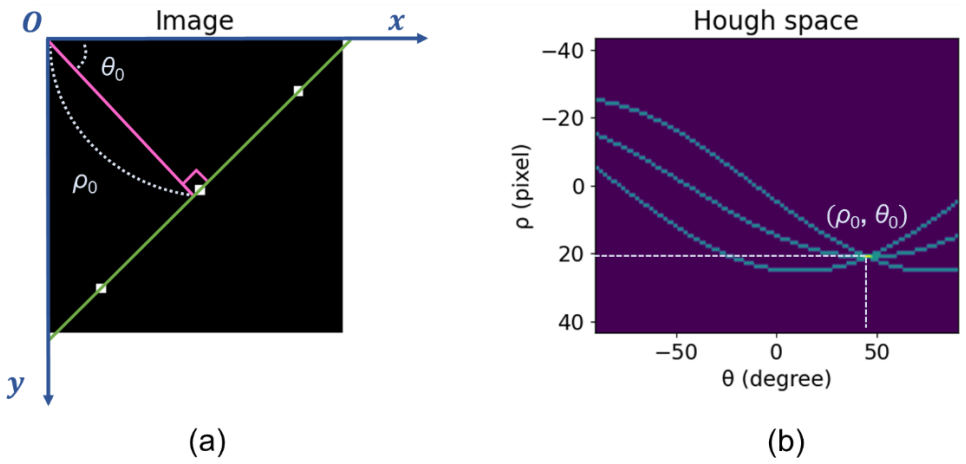

Figure 3-3 (a) Image represented in a coordinate system with its origin at the top left corner and (b) Hough space derived from Eq. (2), which corresponds to the white pixels in (a). The image in (a) contains three white pixels. A green straight line passes through all the three pixels. A pink arrow, starting from the origin, is drawn perpendicular to the green line. The length of the pink arrow is denoted by ρ_0, while the angle between the pink arrow and the x-axis is represented by θ_0. On the coordinate plane in (b), the horizontal axis represents θ (in degrees), while the vertical axis represents ρ (in pixels). The range of θ is calculated from 90° to -90°.

In Hough space, a "vote" refers to a value assigned to a pair of ρ and θ, which denotes a specific geometric shape. The greater the number of pixels that a line traverses, the more votes it can accumulate. The accumulation of votes allows for the detection of geometric shapes or patterns in an image. In Fig. 3-3(a), three pixels are converted into three curves in Fig. 3-3(b). The point where these three curves intersect is represented by the combination of ρ_0 and θ_0, which has the highest number of votes compared to other pairs of ρ and θ on the curves. Therefore, the combination of ρ_0 and θ_0 indicates the only line that passes through these pixels, corresponding to the green line in Fig. 3-3(a). By identifying the point with the highest number of votes in the corresponding Hough space, this approach can detect lines present in an image.

3.4.3. Image filtering and Hough transform

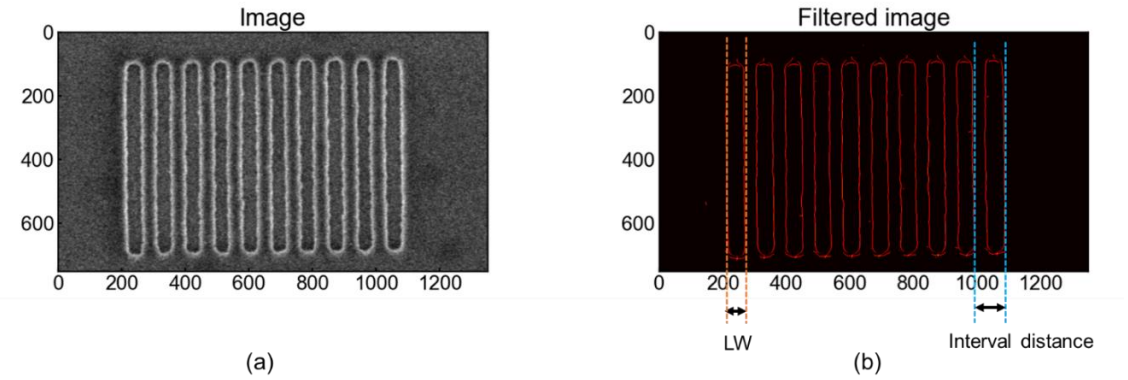

Figure 3-4 (a) SEM image of resist L/S patterns and (b) filtered image resulting from the image preprocessing to image (a). The HP of the pattern was 45 nm. The exposure dose was 272 μC/cm^2. The edges of patterns were shown in red in (b). These red pixels in the image have a value of 1, while the black background is made up of pixels with a value of 0. The line width (LW) is exemplified in (b) with a pair of orange dashed lines, while the interval distance is demonstrated using two blue dashed lines in the same image.

Figure 3-4(a) depicts an SEM image of resist L/S patterns with a HP of 45 nm, which was exposed to EB radiation at a dose of 272 μC/cm^2. HP means not an actual line width but a designed line width (a target line width). The image was resized to a scale of 1 pixel for 1 nm. To extract the pattern edges, the SEM image was preprocessed with the method mentioned in section 3.4.1 [Eq. (3-1)] and then converted into a binary image. The σ in Eq. (3-1) in this filter was 10.5. It should be noted that the term "line" in this context refers to the region that is exposed to EB and subsequently dissolved by the developer. The "line width (LW)" refers to the average width of all the lines that are included in the SEM images. On the other hand, the "interval distance" refers to the distance between the right (or left) edge of a pattern and the corresponding right (or left) edge of the adjacent pattern. The LW and interval distance were shown by a pair of orange and blue dashed lines in Fig. 3-4(b), respectively.

During the Hough transform of pixels composing edges, the accumulation of votes in the Hough space was determined by the number of pixels that a straight line can pass through. While this method can effectively locate every edge in the vertical direction of the image, it may fail to detect edges in patterns that are

severely defected, deformed or lack clear edges. In contrast to the traditional straight line detection in the lithography field, this study adopted a different approach by determining LW and interval distance for the resist patterns as a whole, instead of evaluating patterns individually.

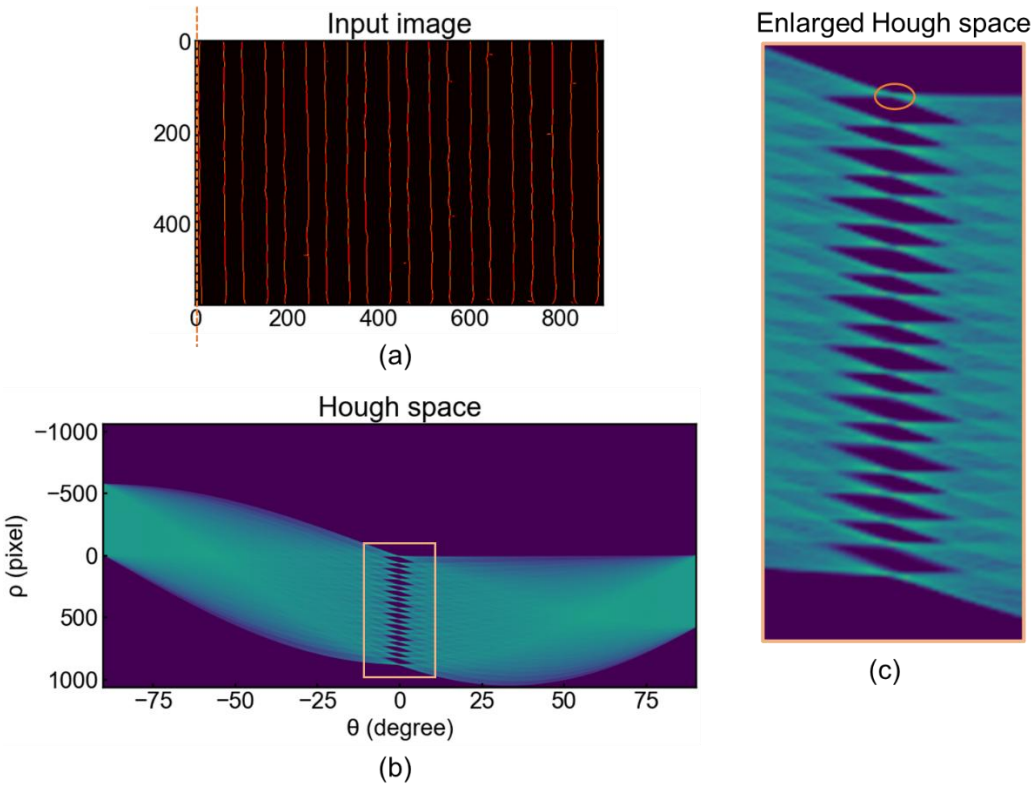

Figure 3-5 (a) Input image for Hough transform, (b) Hough space of the filtered image of (a), and (c) the enlarged view of (b). The HP of resist patterns in (a) was 45 nm and the exposure dose was 272 μC/cm^2. (a) depicts a cropped version of Fig. 3-4(b), in which the residual blank area surrounding the resist patterns and the top and bottom edges of the resist patterns have been removed. The orange dashed line in (a) corresponds to the orange circle in (c). The enlarged view of the profiles approximately 0° [marked by the yellow box in (b)] is shown in (c). The orange circle in (c) represents the first overlapping point of the trigonometric function curves, which corresponds to the first red line in (a).

Before going into the detailed determination process, to focus on the pattern of interest, the blank area surrounding the resist patterns and the upper and

lower edges were cropped out, as illustrated in Fig. 3-5(a). After detecting edges and applying Hough transform [Eq. (3-2)], the Hough space displayed in Fig. 3-5(b) was obtained, where the degree θ is represented on the horizontal axis and the distance ρ is on the vertical axis. As the lines are mostly vertical, the number of votes get larger in the area near 0°, as shown in zoomed-in Fig. 3-5(c). As an example, the first overlapped votes circled in orange in Fig. 3-5(c) indicates a pair of ρ and θ that represent the line passing through the leftmost edge overlapped by a dash orange line in Fig. 3-5(a). Since there are a total of 20 edge lines in Fig. 3-5(a), 20 sets of overlapped points can be observed in Fig. 3-5(c) at approximately 0°.

Understanding the feature of the input image is important for determining the detection range of degrees and distances (LW and interval distance). The degree of edges was initially determined for lines in the Hough space. After determining the common angle, the votes at the same degree with different distance ρ were discussed. More specifically, the line-to-space pattern of the resist image is represented by four parameters: LW w; interval distance d; a common angle for multiple parallel lines θ_{com}; and distance ρ_0 between the image origin and the first line. Given the number of votes in Hough space as $v(\rho, \theta)$, the likelihood of the four parameters $L(w, d, \theta_{\mathrm{com}}, \rho_0)$, i.e., the degree how well the four parameters describe the observed resist image, is then computed by summation of the votes for all the lines by the following equation

$$L(w, d, \theta_{\mathrm{com}}, \rho_0) = \sum_{i=1}^{N} \big(v(\rho_0 + id, \theta_{\mathrm{com}}) + v(\rho_0 + w + id, \theta_{\mathrm{com}}) \big), \quad (3\text{-}3)$$

where N is the number of line pairs (i.e., left and right sides of lithography). The optimal four parameters which describe the resist image the best are then obtained by

$$(w^*, d^*, \theta_{\mathrm{com}}^*, \rho_0^*) = \underset{w, d, \theta_{\mathrm{com}}, \rho_0}{\operatorname{argmax}} \; L(w, d, \theta_{\mathrm{com}}, \rho_0). \quad (3\text{-}4)$$

By taking into account the impact of LER, the search range of w was set to be larger than LER and smaller than twofold HP. On the other hand, regarding the stability of d, as observed during the analysis, its search range was set to be ±20% HP from twofold HP. For the θ_{com}, the search range was set to be from -1.0° to 1.0°. Additionally, since the pattern interested was automatically cropped out from the original image, the search range of ρ_0 was set to be from 0 to 20 pixels.

3.5 Results and discussion

3.5.1. LW and interval distance measurement

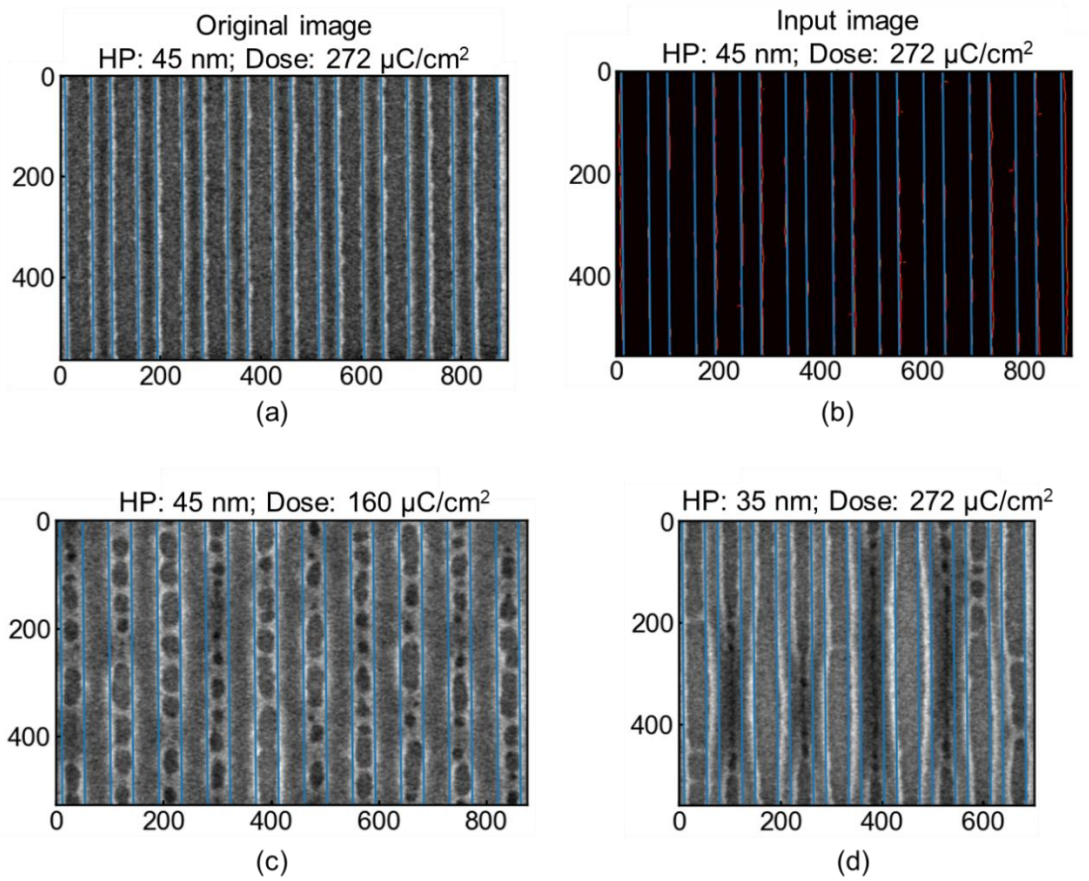

Figure 3-6 (a) SEM image with 45 nm HP and 272 μC/cm^2 exposure dose, (b) the preprocessed input image of (a), (c) SEM image with 45 nm HP and 160 μC/cm^2 exposure dose, and (d) SEM image with 35 nm HP and 272 μC/cm^2 exposure dose. Straight blue lines on all the figures were plotted with the most appropriate LW and interval distance that obtained the highest number of votes. The angle of all of the aligned blue lines in these figures was -0.5°, determined on the basis of the LW and interval distance pair with the highest number of votes. (a) is a cropped original SEM image, while (b) shows the input image [the same as Fig. 3-5(a)]. (c) represents a severely defected pattern that barely dissolved. On the other hand, (d) exemplifies a deformed pattern.

The meaning of covering the edge pixels is further explained, using examples shown in Fig. 3-6. Figures 3-6(a) and (b) are the cropped patterns of Figs. 3-4(a) and (b), respectively. The average pixel number of detected edges highlighted in red in Fig. 3-6(b) was 559. The blue lines, which overlay the red lines, represent the ideal edges with no defects. The pixel count of an ideal edge line was 556. In the case of a fine pattern, the pixel count for the edges is similar. The overlap between the ideal and real edges consisted of 115 pixels (the highest number of votes). The deviation of the real edges from the ideal edges was approximately 2.2 nm.

Based on Eqs. (3-3) and (3-4), the optimal w, d, θ_{com}, and ρ_0 for the case shown in Fig. 5(a) were 52 nm, 90 nm, -0.5°, and 9 nm, respectively. This indicates that, as shown by the blue lines in Fig. 3-6(b), lines aligned at -0.5° with the combination of 52 nm LW and 90 nm interval distance can cover the highest number of edge pixels in the input image. This conclusion was confirmed by overlapping the calculated line edges with the cropped original image, as shown in Fig. 3-6(a).

The measurement of deformed patterns is difficult due to several reasons. Firstly, at low doses, patterns are formed sparsely, making it challenging to determine the edges. Secondly, at high doses, the edges of lines are detached from the Si substrate due to over-dissolution, causing them to move far from their original position and making analysis difficult. With the proposed method, it becomes possible to determine the average LW and interval distance of the resist pattern. As shown in Fig. 3-6(c), the pattern was exposed at a low dose, resulting in numerous bridges and broken edges. However, by measuring the pattern as a whole instead of pitch by pitch, the random cuts or stochastic defects on the edges can be compensated by other pitches. The w, d, θ_{com}, and ρ_0 for the case shown in Fig. 3-6(c) were measured to be 42 nm, 90 nm, -0.5° and 7 nm, respectively. The average pixel count for the ideal edge was 518, while it was 568 for the real edge. This difference was brought by the bridging defect between the lines. The number of overlapped pixels was 72. In contrast, Fig. 3-6(d) shows a pattern exposed at a high dose, leading to a deformed pattern that is difficult to determine the edges and line widths. Nevertheless, the straight lines that pass through the highest number of pixels can still evaluate this kind of pattern, based on Eq. (3-4).

As a result, the w, d, θ_{com}, and ρ_0 for the case shown in Fig. 3-6(d) were measured to be 45 nm, 70 nm, -0.5° and 5 nm, respectively. The average pixel count for the ideal edge was 551, whereas it was 408 for the real edge. This difference in count was attributed to over-dissolution, where the edges become stuck together and cannot be individually detected. The number of overlapped pixels was 50, indicating that the edges were significantly displaced from their intended positions. It is important to mention that the evaluation of patterns with unclear edges may not be as consistent as those with clear edges. Nevertheless, the vote distribution for such patterns exhibits unique characteristics that are worth discussing.

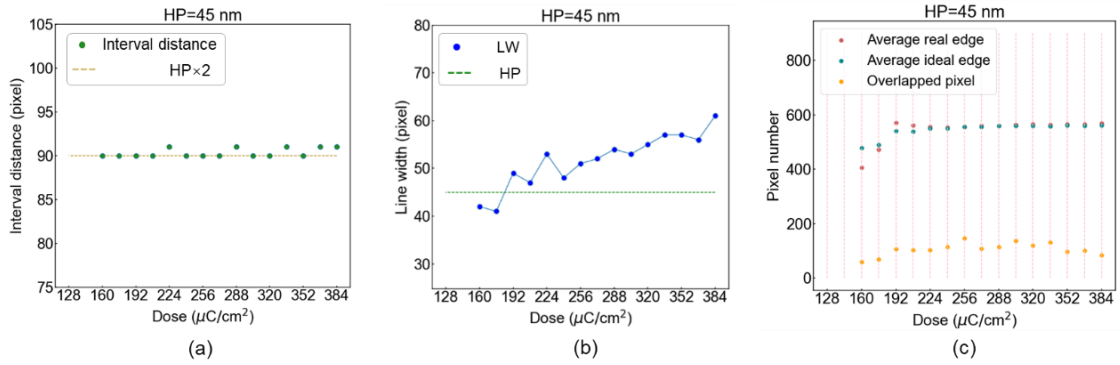

Figure 3-7 (a) Estimated interval distance, (b) estimated LW and (c) pixel counts for the average number of ideal and real edges, as well as the number of overlapped pixels for the samples with HP of 45 nm. The LW and interval distance are plotted against the dose. The interval distances are denoted by green dots in (a), where the brown dashed line indicates the pitch (the reference for interval distance) which is twice the HP. In (b), the green dashed line represents HP (the reference for LW). In (c), the pink dashed lines in the vertical direction serve as references for the doses. The red, green, and orange dots correspond to the pixel count for the real edge, the ideal edge, and the overlapped edge, respectively.

Upon analyzing hundreds of resist patterns on the wafer, it was discovered that the profile with -0.5° rotation had the highest votes in the most cases. This indicates that the wafer was tilted at -0.5°. Therefore, hereafter, the analysis was conducted based on the -0.5° files for all the images. As a representative results,

Figs. 3-7(a) and 3-7(b) demonstrate the dose dependence of interval distance and LW of the samples with 45 nm HP. The original SEM images for all the samples are provided in Table 2-I. The measured results of LW and interval distance for other HPs are included in Fig. 3-1. By examining the interval distance against changing dose, it was evident that the interval distances remain relatively stable. This observation suggests that patterns with interval distances significantly deviating from twice the HP correspond to the deformed patterns. Except for the deformed patterns, LW was found to increase with increasing dose, while the interval distance remained stable despite the changes in LW.

In terms of pixel count, as depicted in Fig. 3-7(c), it is evident that when the ideal and real edges are in close proximity, their pixel counts are also similar. In cases where the pattern contains bridges within the lines, the pixel count tends to exceed the ideal number [doses of 192 and 208 $\mu C/cm^2$ in Fig. 3-7(c)]. Conversely, when the pattern is distorted due to over-dissolution or incomplete dissolution, resulting in incomplete formation of the pattern, the pixel count tends to be lower than the ideal count [doses of 160 and 176 $\mu C/cm^2$ in Fig. 3-7(c)]. Additionally, the number of overlapped pixels reflects the deviation between the real edges and the ideal edges. As a result, a closer match between the overlapped pixel count, ideal pixel count, and real pixel count indicates a lower LER. This can also be viewed from the magnified Hough space shown in Fig. 3-5(c) that the overlapping points were often not a single point. Therefore, LWs and interval distances that are close to the most appropriate ones tend to have similar vote numbers. This has motivated me to explore further the votes obtained from different assumed LWs and interval distances. The vote results for Fig. 3-5(b) at -0.5° were plotted into contour maps and three-dimensional figures shown in the following section.

3.5.2. Evaluation by vote distribution

Upon analyzing the measurement results of approximately 200 patterns, no single index could fully reflect the overall characteristics of the patterns was observed. However, several indexes that captured the specific aspects of the pattern's features were identified. The following discussion presents a selection of analysis results that provide insights into the pattern's characteristics.

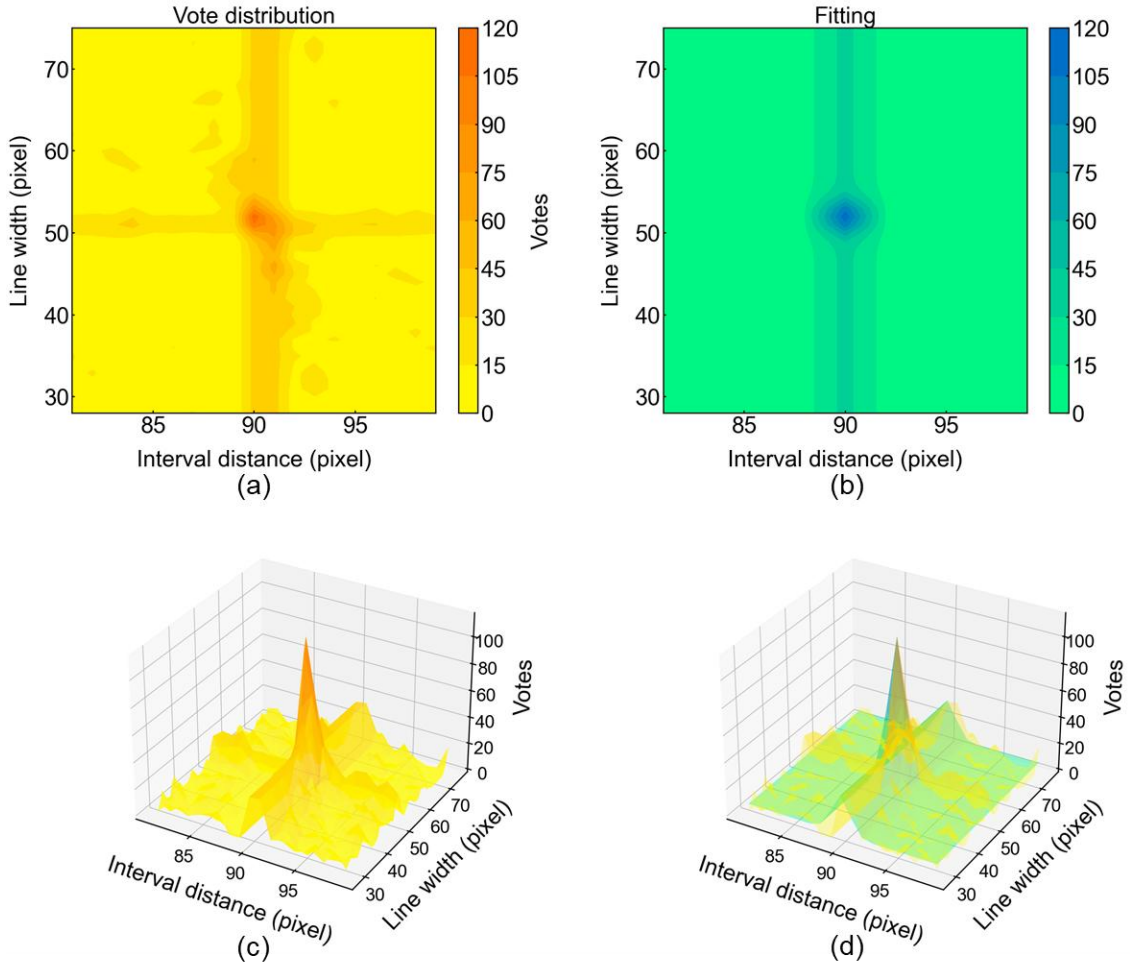

Figure 3-8 (a) Contour plot illustrates the distribution of votes for different assumed LW and interval distances with a yellow-red color bar shown on the right. (b) Fitting result for the vote distribution (a) with a green-blue color bar on the right. (c) 3D plot of (a). (d) 3D plot of (b) overlapped with (c). The original SEM image is shown in Fig. 3-6(a).

The accumulated vote distribution is presented in Fig. 3-8(a) for various combinations of LW and interval distance with interval distance on the horizontal axis and LW on the vertical axis with the optimal θ^*_{com} and ρ^*_0, i.e., two-dimensional vote distribution $L_2(w,d) = L(w,d,\theta^*_{\mathrm{com}},\rho^*_0)$. The peak coordinates of the vote distribution correspond to the measured LW and interval distance obtained from the SEM image. The LW and interval distance of the SEM image

in Fig. 3-4(a) were determined to be 52 nm and 90 nm, respectively, based on the combination that received the highest number of votes [the peak in Fig. 3-8(a)]. This vote distribution map is an example indicating the stability of the interval distance. More specifically, the interval distance was found to be consistent at a value of twice the HP, independently of LW. From the perspective of the accumulation process of votes, when the interval distance is set to the most suitable width, the pixels on the left edge of all line patterns can consistently be accumulated. Consequently, the votes at the interval distance of twice the HP experience a significant increase. On the other hand, while an appropriate LW ensures the accumulation of edge pixels for the first line pattern, it may not guarantee the same for subsequent lines. Thus, in comparison to LW, variations in the interval distance provide information about the outline of the pattern's characteristics. Based on the stability of the interval distance, it was considered as a feature in the evaluation of the vote distribution. The distribution was fitted using a specific distribution, which is defined as

$$f(x) = A\left(\exp\left(-\frac{(x-x_0)^2}{2\sigma_x^2}\right)\right)\left(\exp\left(-\frac{(y-y_0)^2}{2\sigma_y^2}\right) + b\right) + c,$$

$$\int_{y_{min}}^{y_{max}} \int_{x_{min}}^{x_{max}} f(x)dxdy = 1 \tag{3-5}$$

where A represents the amplitude, x and y denote the pixel coordinates, x_0 and y_0 denote the coordinates of the peak that has the highest number of votes in the vote distribution plane, and b and c are constants. The measured range of interval distance and LW are denoted by x_{max}, x_{min}, y_{max}, and y_{min}, respectively. The standard deviations of the vote distribution of interval distance and LW were represented by σ_x and σ_y. The constant c contributes to the whole distribution. Constant b contributes to the interval distance distribution. The integral of the Gaussian function was normalized to 1. Therefore, the constant c was normalized by dividing it by the sum of the total votes. The fitting results are depicted in Figs. 3-8(b) and (d). Another index is defined as below.

$$\sigma_{vote} = \sqrt{\sigma_x^2 + \sigma_y^2} \tag{3-6}$$

The value of σ_{vote} was derived based on σ_x and σ_y. The evaluation of the vote distribution was based on σ_x, σ_y, σ_{vote}, and normalized constant c which is denoted by C_{vote}. The original distribution was well fitted by Eq. (3-5) as shown in

Fig. 3-8(d). By employing this approach, σ_x and σ_y were measured to be 0.84 and 1.47 nm, respectively. The σ_{vote} of the whole distribution was 1.70 nm. To further analyze the characteristics of the vote distribution and describe the defects in terms of interval distance stability, the vote distribution map was horizontally divided into two halves at the peak and then concatenated with its mirror image. This process is illustrated in Figs. 3-9(a) and (c).

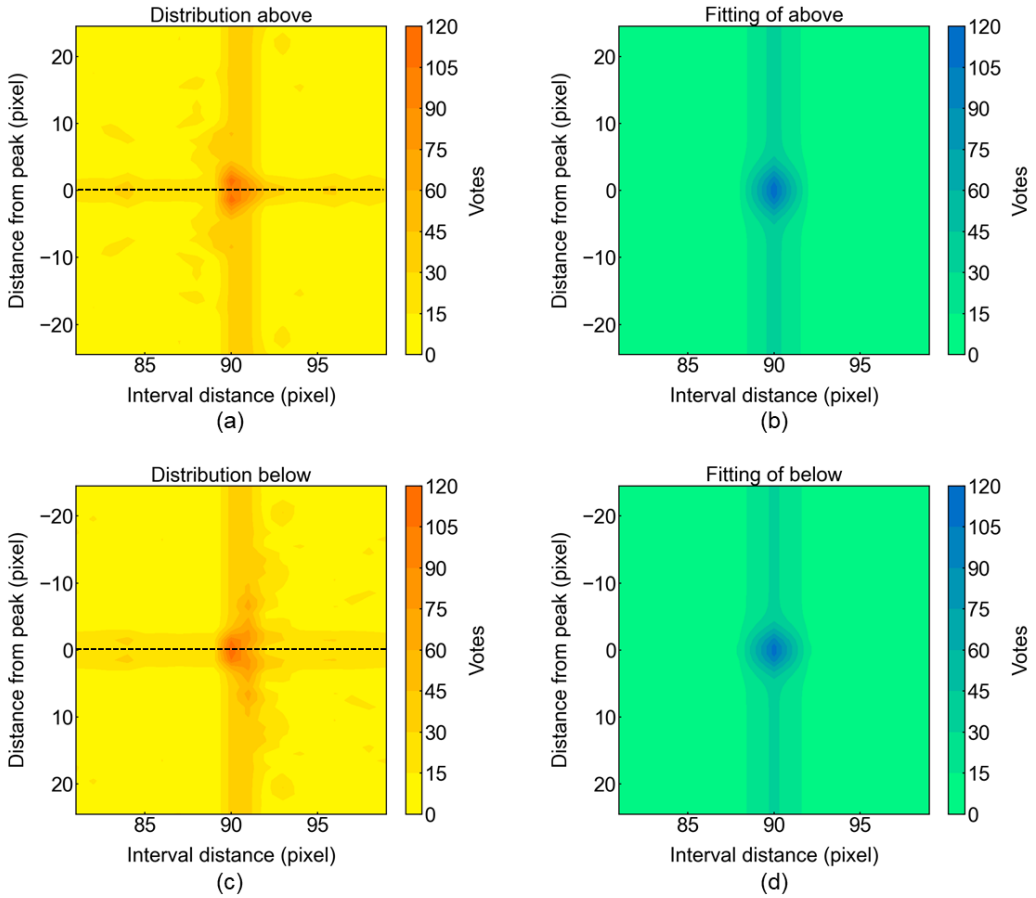

Figure 3-9 Counter plots of vote distributions. The upper half of (a) above the dashed line displays the vote distribution above the peak of Fig. 3-8(a). The lower half is the mirror image of the upper half. The fitting result to (a) was presented in (b). The lower half of (c) below the dashed line is the vote distribution below the peak of Fig. 3-8(a). The lower half is the mirror image of the upper half. The fitting result to (c) was presented in (d). Note that the coordinates of mirror images were negative.

The vote distribution above the peak of Fig. 3-8(a) was reflected across the horizontal dashed line and combined with the original distribution to generate Fig. 3-9(a). Similarly, the vote distribution below the peak was reflected across the dashed line and combined with the original to create Fig. 3-9(c). The above and below distributions were separately fitted by Eq. (3-5). The fitting results for the distributions in Figs. 3-9(a) and (c) are shown in Figs. 3-9(b) and (d), respectively. Since the image was divided in half based on the LW, the standard deviation in the LW direction (y-axis) could not accurately represent the above and below vote distribution. The distribution above corresponds to the range of LW larger than HP. It reflects variations in defects outside the line, which are typically caused by over-dissolution. On the other hand, the distribution below corresponds to the range of LW smaller than HP. It reflects variations in defects within the line, which are typically caused by incomplete dissolution.

The standard deviation on the interval distance direction (x-axis) was denoted as $\sigma_{\text{above\_x}}$ and $\sigma_{\text{below\_x}}$ for the distributions above and below the peak, respectively. Similarly to σ_{x}, a small value of $\sigma_{\text{above\_x}}$ or $\sigma_{\text{below\_x}}$ indicates a pattern with few defects. According to the fitting results, $\sigma_{\text{above\_x}}$ and $\sigma_{\text{below\_x}}$ were 0.82 and 0.88 nm for the pattern with 45 nm HP, exposed to 272 μC/cm^2 EB, respectively. The constant c of the above and below distributions, denoted as C_{above} and C_{below} were 1.76 and 1.81, respectively. The result of subtraction C_{above} from C_{below} was 0.06.

Similarly, the vote distribution was also divided into left and right halves. The standard deviations in the LW direction (y-axis) were denoted as $\sigma_{\text{left\_y}}$ and $\sigma_{\text{right\_y}}$ for the distributions on the left and right of the peak, respectively. The variation along LW direction was computed in the same manner as the interval distance directions. For the pattern with a 45 nm HP, exposed with a dose of 272 μC/cm^2, the fitting results for $\sigma_{\text{left\_y}}$ and $\sigma_{\text{right\_y}}$ were 1.67 and 1.04 nm, respectively.

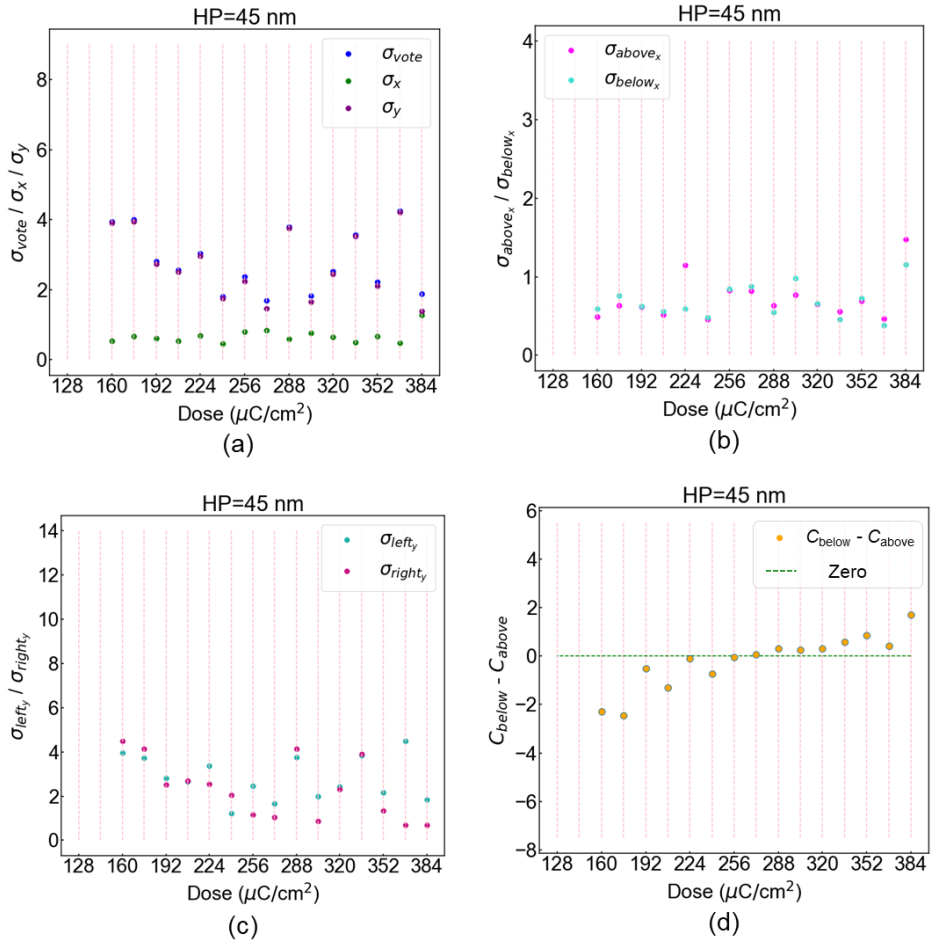

Figure 3-10 Standard deviations and C_{below}-C_{above} of L/S patterns with 45 nm HP. (a) σ_{vote}, σ_x, and σ_y for the full vote distribution. (b) σ_{above_x} for the above half and σ_{below_x} for the below half on the interval distance direction. (c) σ_{left_y} for the left half and σ_{right_y} for the right half on the LW direction. (d) C_{below}-C_{above}.

Figure 3-10 displays the evaluation indexes, which reveal features of the patterns. In this study, the defected or deformed patterns typically have σ_{vote} larger than 2.5 nm. The σ_{vote} is mainly affected by σ_y that indicates the variation of LW. The variation in the interval distance is represented by σ_x shown in Fig. 3-10(a) by green dots. σ_x for all samples with 45 nm HP was approximately 1 nm, which corresponds to the findings in Fig. 3-7(a) where the interval distance remained stable even though the LW increased. The patterns having σ_x larger than 1 nm are considered to be deformed. Following σ_x, σ_{above_x} and σ_{below_x} for fine patterns were also found to be approximately 1 nm as shown in Fig. 3-10(b). It was observed that patterns with a difference between σ_{above_x} and σ_{below_x} are larger than 1 nm indicate

a deformed pattern without a clear interval distance. The variation of LW is represented by σ_y shown in Fig. 3-10(a) by dark purple dots. Poor patterns generally lead to high σ_y value. Similarly to σ_y, the σ_{right_y} and σ_{left_y} tend to be small in fine patterns. However, some deformed patterns were found to have small σ_{vote} values. This is because the constant c in Eq. (3-5) is related to the disordered vote distribution. To be exact, due to the expansion of the lines, the edges are far from their original position. The pixels composed of such edges are also counted as a vote in Hough space. Consequently, the accumulated votes are spread out rather than concentrated within a specific interval distance and LW. The spread vote distribution increases C_{vote} to account for this wide distribution. Hence, further investigation was conducted on the constant c. It was discovered that the difference between C_{above} and C_{below} shows a significant correlation with pattern defectiveness. Figure 3-10(d) illustrates that fine patterns generally exhibit similar values for C_{above} and C_{below}. In summary, this method allows for the assessment of resist pattern defects based on several effective indexes. It should be noted that the threshold used to differentiate between fine and defective patterns in this case is specific to the patterns in this study and may differ for other patterns. First, in this case, when the difference in edge pixel count between the real pattern and the ideal pattern is greater than 50, the pattern is considered to be defective. Second, when the measured interval distances deviate larger than 1 nm from twice HP, the pattern is considered deformed. Third, when the σ_{vote} is larger than 2.5 nm, the pattern is defected, especially by bridges between lines. Fourth, when σ_x, σ_{above_x} and σ_{below_x} are greater than 1 nm, the pattern is regarded as having significant defects that cause the pattern deformation. Finally, the closer the values of C_{above} and C_{below} are to each other, the better the pattern quality.

3.5.3. Application for chemical parameter estimation

One of the applications of this method and evaluation criteria is to compare defected patterns with simulation results. This allows for the evaluation method to be used for the discussion of chemical parameters included in the simulation model with the criteria.

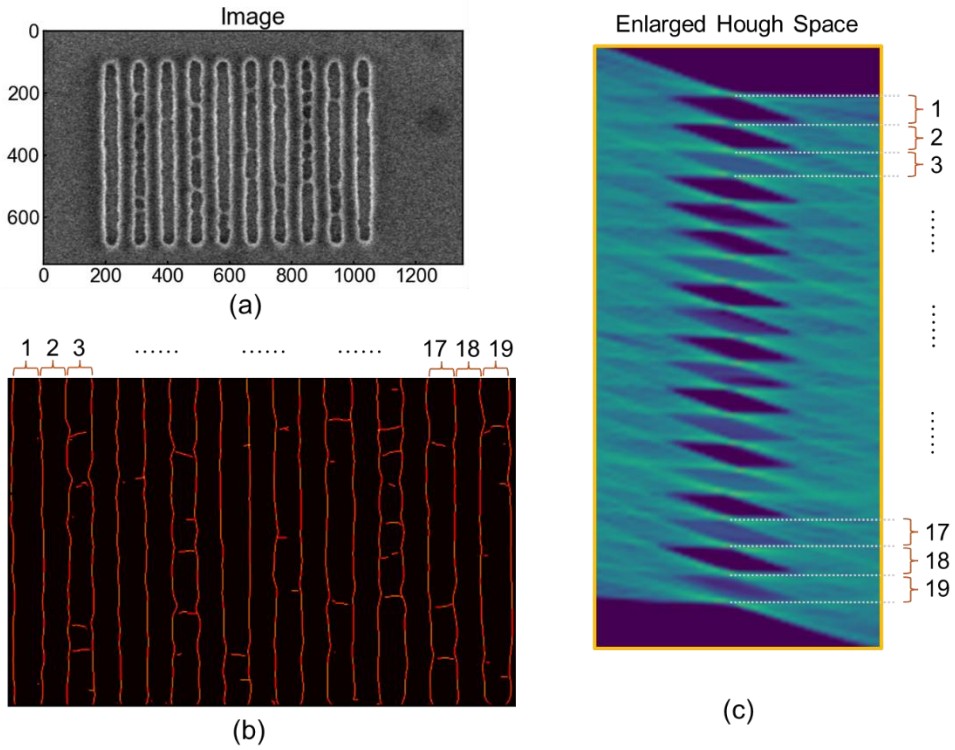

Figure 3-11 (a) SEM image of L/S pattern with multiple bridges in the lines. (b) Preprocessed SEM image of (a). (c) Enlarged Hough space of (b). HP was 45 nm. The exposure dose was 192 μC/cm^2. In (c), the labeled spaces correspond to the labeled spaces in (b).

Figure 3-11(a) depicts an SEM image of a resist L/S pattern with 45 nm HP that was exposed to EB radiation at a dose of 192 μC/cm^2. The filtered image is shown in Fig. 3-11(b). The pattern contains 10 pitches, which results in 20 edge lines after cropping. Figure 3-11(c) displays an enlarged version of the Hough space, which was calculated based on Fig. 3-11(b) and is presented in Fig. 3-11(b). There are 19 spaces within 20 edges, including both the lines and spaces in the L/S pattern. The 1st, 2nd, and 3rd spaces, as well as the 17th, 18th, and 19th, are labeled as examples. These spaces in Fig. 3-11(b) correspond to the intervals between overlapped points that are labeled in the same manner in Fig. 3-11(c). Bridges are clearly visible at the 3rd, 17th, and 19th spaces, and the corresponding intervals in the Hough space show the same votes. In contrast, since there are no bridges in the 1st, 2nd, and 18th spaces, there are no votes in the corresponding intervals. As a result, the vote distribution for the pattern with defects is different from the ones

without defects. The vote distribution [Fig. 3-13(a)] was calculated and compared with the simulation results. All the measured results were summarized in Table 3-II.

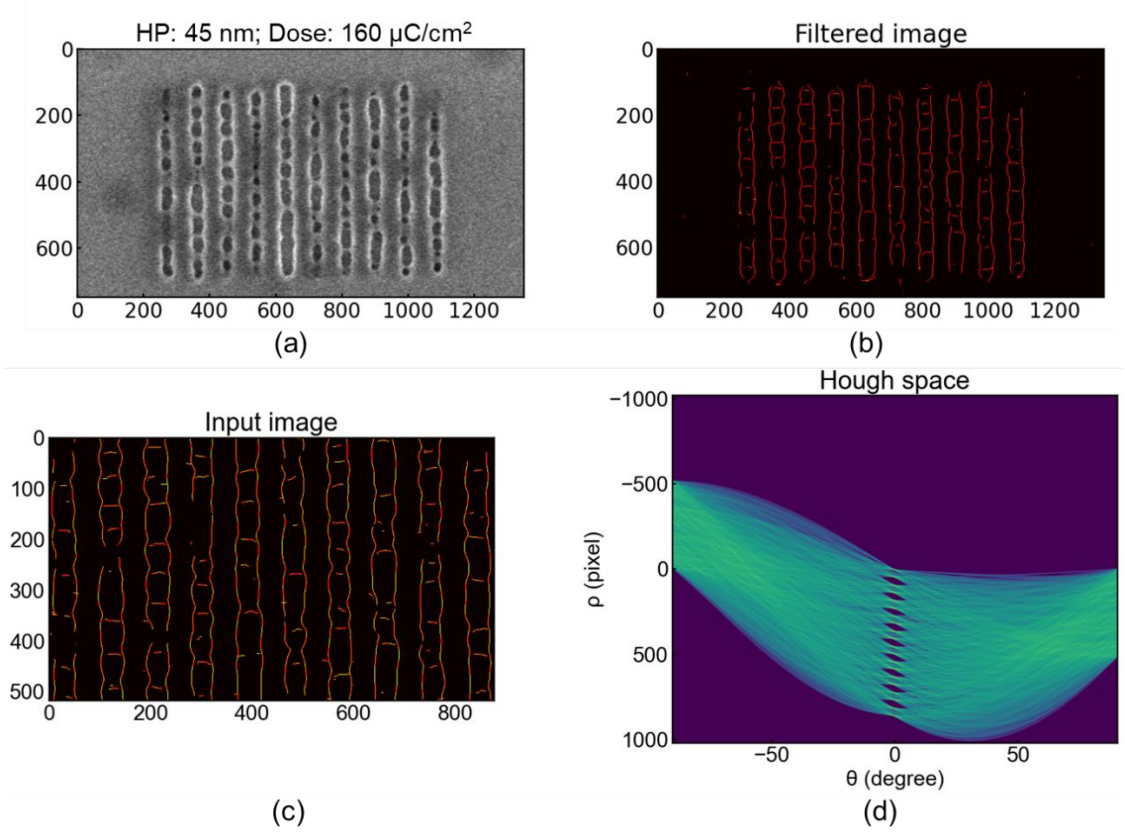

Figure 3-12 (a) SEM image of a resist L/S pattern with 45 nm HP and 160 μC/cm^2 exposure dose. (b) The filtered image resulting from the application of a LoG filter to image (a), in which the edges of pitches were shown in red. (c) A cropped version of (b), in which the residual blank area surrounding the image and the top and bottom edges of the pitches have been removed. (d) Hough space of the filtered image in (a). The Hough transformation maps the pixel coordinates of an image to a parameter space with the left-top as the origin, where the degree θ is represented on the horizontal axis and the distance ρ is on the vertical axis.

In a similar way, the pattern in Fig.3-12 was measured, which is the same image as the picture in Fig. 3-6(c). The LW and interval distance for Fig. 3-12(c) were measured to be 43 and 90 nm, respectively.

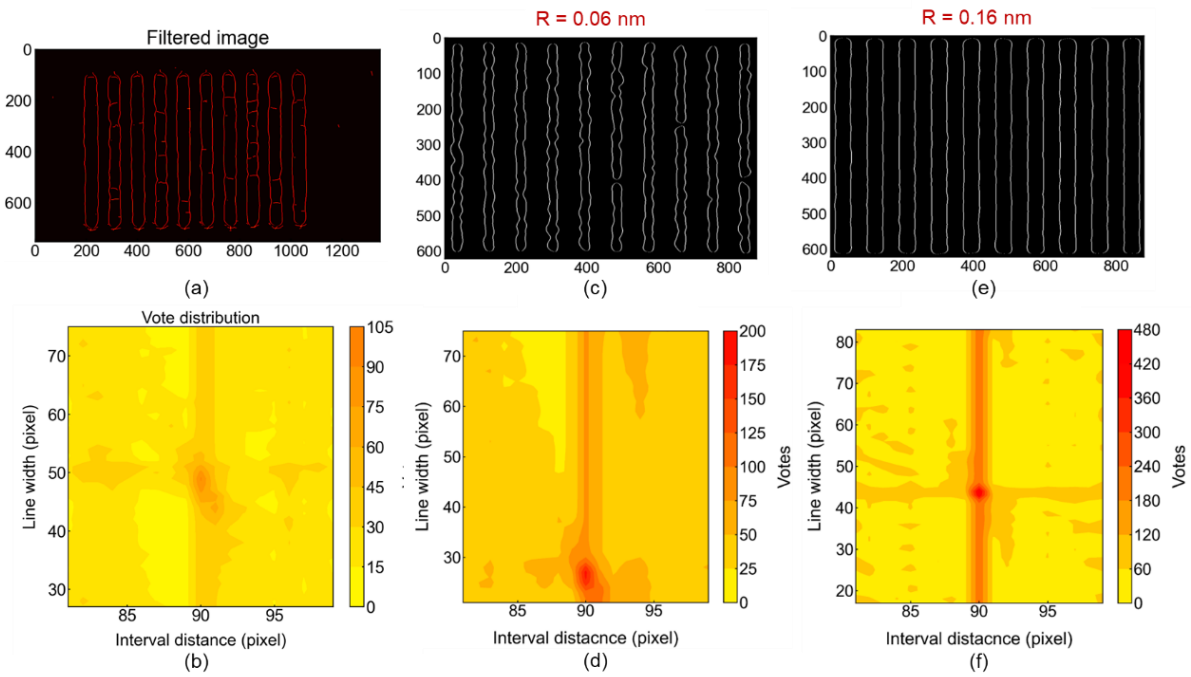

Figure 3-13 (a) Preprocessed image of Fig. 10(a). (b) Vote distribution corresponding to (a). (c) Prepocessed image of the latent image simulated with the effective reaction radius of 0.06 nm. (d) Vote distribution corresponding to (c). (e) Prepocessed image of the latent image simulated with the effective reaction radius of 0.16 nm. (f) Vote distribution corresponding to (e).

The resist patterns were simulated by a resist model, into which various chemical parameters described in Simulation section were incorporated. This approach made it possible to examine how the changes in these parameters affected the shape of the patterns, by comparing the simulation and experimental results. In this study, the effect of R_p on the resist pattern by simulating resist patterns with different values of R_p was investigated. Figures 3-13(c) and (e) show the simulation results of resist pattern edges in white pixels when the values of R_p were 0.06 and 0.16 nm, respectively. The resist patterns were calculated based on the distribution of the concentration of the protected units of the polymer. In order to analyze the LW, interval distance, and defectivities of these two patterns, they were subjected to Hough transform followed by the vote distribution analysis. The vote distributions of the simulated resist patterns are shown in Figs. 3-13(d) and (f).

Table 3-III. Evaluation results of SEM and simulated images.

Dose 192 $\mu C/cm^2$ *HP* 45 nm	*SEM*	R_p = 0.06 nm	R_p = 0.16 nm
Interval distance (nm)	90	90	90
LW (nm)	47	27	44
σ_{vote} *(nm)*	2.81	2.76	0.98
σ_{above_x} *(nm)*	0.61	0.60	0.43
σ_{below_x} *(nm)*	0.63	0.68	0.44
σ_{left_y} *(nm)*	2.80	2.72	1.12
σ_{right_y} *(nm)*	2.51	2.56	0.68
C_{below} - C_{above}	-0.52	-4.15	-1.15

Table 3-III shows that the interval distance remains geometrically stable regardless of changes in LW or σ. Simulation results demonstrated that when R_p was 0.16 nm, the simulated LW value approximately agrred with the actual LW (SEM image), which was measured to be 47 nm. When R_p was 0.06 nm, the LW of the pattern was smaller than the HP. This means the pattern was under-development. Conversely, when R_p was 0.06 nm, the simulated σ_{vote}, σ_{above_x}, σ_{below_x}, σ_{left_y} and σ_{right_y} were closer to the SEM image. For C_{below}-C_{above}, the value calculated with low R_p was far from the SEM result, while a higher R_p has a closer value. These results indicated that the defects inside of the lines [Fig. 3-13(a)] were reproduced by lower R_p and the defectivity of SEM lay between R_p values of 0.06 nm and 0.16 nm. Although the defectivity was partially reproduced through the simulation of sensitization and PEB processes, the LW was not able to be reproduced by this mechanism.

Based on experimental SEM data, it was observed that bridging can occur even when LW was larger than HP. On the other hand, the simulations based on the reaction machanism of CARs were not able to reproduce simultaneously LW

and defects. These observations indicate that factors beyond the concentration of protection units on the polymer's side chain have a significant impact on the fidelity of the latent pattern and cannot be ignored. Since the development kinetics parameters are not fully incorporated into the simulation system, the development process is considered to have a significant impact on the defect formation. The modeling of dissolution kinetics is necessary for a more accurate estimation of chemical information that can reproduce the defect formation.

3.6 Conclusion

An image recognition technique was utilized to establish a new measurement method for patterns with defects. Unlike the traditional methods that evaluate patterns pitch by pitch, by converting the filtered image into Hough space, the LW and the interval distance of the whole resist pattern can be determined. It was found that the number of votes was high when the interval distance was twice the HP, even when the LW changed. This approach allowed for the quantitative assessment of severely defected pattern, and is applicable to the deformed pattern with further analyzation towards their vote distribution.

To utilize the defectivity information, this method was employed to estimate the R_p of 54.6 mol% t-Boc-protected PHS, which ranged from 0.06 to 0.16 nm. However, the distribution of protecting unit concentration alone could not precisely reproduce the resist patterns, including both LW and the formation of defects simultaneously. Specifically, when the LW was consistent, the defects did not match, and vice versa. As a result, the study concluded that a dissolution mechanism was necessary to achieve more accurate simulation that closely aligned with the experimental findings for patterns with defects.

3.7 Reference

1) T. Itani, P. A. Gargini, P. P. Naulleau, and K. G. Ronse, Proc. SPIE **11147**, 1114701 (2019).

2) T. Kozawa, J. J. Santillan, and T. Itani, Jpn. J. Appl. Phys. **52**, 076502 (2013).

3) M. Harumoto, A. F. Santos, J. J. Santillan, T. Itani, and T. Kozawa, Jpn. J. Appl. Phys. **62**, 016503 (2023).

4) S. K. Sarkar, S. Das, V. M. B. Carballo, P. Leray, and S. Halder, J. Micro/Nanopatterning Mater. Metrol. **21**, 044901 (2022).

5) H. Fukuda, J. Appl. Phys. **132**, 064905 (2022).

6) Y. J. Choi, J. Vac. Sci. Technol. B **40**, 042602 (2022).

7) L. S. Melvin III, Jpn. J. Appl. Phys. **61**, SD1030 (2022).

8) K. Azumagawa and T. Kozawa, Jpn. J. Appl. Phys. **60**, SCCC02 (2021).

9) H. Ito, *Microlithography/Molecular Imprinting Advances in Polymer Science Series* (Springer, Heidelberg, 2005) Vol. 172, p. 37.T. Kozawa and S. Yoshitake, Jpn. J. Appl. Phys. **56**, 076501 (2017).

10) T. Kozawa and T. Tamura, Jpn. J. Appl. Phys. **56**, 116501 (2017).

11) T. Kozawa and S. Tagawa, Jpn. J. Appl. Phys. **49**, 030001 (2010).

12) K. Azumagawa and T. Kozawa, Jpn. J. Appl. Phys. **59**, 116505 (2020).

13) Y. Jin and T. Kozawa, Jpn. J. Appl. Phys. **61**, 066504 (2022).

14) R. O. Duda and P. E. Hart, "Use of Hough transformation to detect lines and curves in picture", CACM, **15**, pp.11-15 (1972).

15) C. A. Mack and G. F. Lorusso, J. Vac. Sci. Technol. B **37**, 062903 (2019).

16) G. F. Lorusso, V. Rutigliani, F. V. Roey, and C. A. Mack, Microelectronic Eng. **190**, 33 (2018).

17) T. Ohashi, T. Sekiguchi, A. Yamaguchi, J. Yanaka, and H. Kawada, J. Micro/Nanolith. MEMS MOEMS **14**, 034001 (2015).

18) H. Kawada, T. Kawasaki, J. Kakuta, M. Ikota, and T. Kondo, Proc. SPIE **10585**, 1058526 (2018).

19) K. Natsuda, T. Kozawa, K. Okamoto, and S. Tagawa, Jpn. J. Appl. Phys. **45**, L1256 (2006).

20) K. Natsuda, T. Kozawa, K. Okamoto, and S. Tagawa, Jpn. J. Appl. Phys. **46**, 7285 (2007).

21) T. Kozawa, Jpn. J. Appl. Phys. **51**, 086504 (2012).

22) T. Kozawa, Jpn. J. Appl. Phys. **54**, 096501 (2015).

23) T. Kozawa, Jpn. J. Appl. Phys. **54**, 056501 (2015).

24) N. Maeda, A. Konda, K. Okamoto, T. Kozawa, and T. Tamura, Jpn. J. Appl. Phys. **59**, 086501 (2020).

25) T. Fukuyama, T. Kozawa, S. Tagawa, R. Takasu, H. Yukawa, M. Sato, J. Onodera, I. Hirosawa, T. Koganesawa, and K. Horie, Appl. Phys. Express **1**, 065004 (2008).

26) T. Kozawa and S. Tagawa, Jpn. J. Appl. Phys. **50**, 030209 (2011).

27) H. Yamamoto, T. Kozawa, A. Nakano, K. Okamoto, Y. Yamamoto, T. Ando, M. Sato, H. Komano, and S. Tagawa, Jpn. J. Appl. Phys. **43**, L848 (2004).

28) Y. Ikari, K. Okamoto, A. Konda, T. Kozawa, and T. Tamura, Jpn. J. Appl. Phys. **59**, 086506 (2020).

29) Y. Yagi and M. Yachida, Int. J. Computer Vision **58**, 173 (2004).

30) K.Yamazawa, Y.Yagi, and M. Yachida, Proc. IAPR Int. Conf. on Pattern Recognition **3**, 487 (2000).

31) D. H. Ballard, Pattern Recognition **13**, 20111 (1981).

32) R. O. Duda, P. E. Commun. ACM **15**,11 (1972).

Chapter 4. Practical application

4.1 Introduction

New resists, such as metal-containing resists and negative-tone development (NTD) resists, are being developed to meet the demands for lower dose consumption and reduced pattern defects in EUV lithography. Organic developers are primarily used for these resists. On the other hand, standard aqueous developers have reached their limitations as the chemical properties of the resists evolved. These requirements make the exploration of new developer possibilities necessary, making the evaluation of developers critical to ensure optimal performance of the resist patterns. In Chapter 2, a simulation model was built to reproduce QCM charts, including frequency changes and impedance changes, to extract the features of developers. The impedance change, in particular, offers insights into the viscosity changes during the development process. To further understand the relationships among these feature values and how they affect the actual resist patterns, L/S patterns were drawn with electron beams (EB) at different doses and developed using various developers. This study utilized tetramethylammonium hydroxide (TMAH), butyltrimethylammonium hydroxide (BTMAH), ethyltrimethylammonium hydroxide (ETMAH), and propyltrimethylammonium hydroxide (PTMAH) as developers. In Chapter 3, an automatic evaluation method based on Hough transform was developed to analyze L/S pattern images captured by scanning electron microscope (SEM). This method was employed in the current study to extract the SEM image feature values. A machine learning method, clustering was used to classify the SEM images based on the SEM features. By comparing these feature values with the reproduced QCM chart data, which highlights the developers' properties, these analyses provided valuable insights into the effectiveness of different developers in processing the resists.

4.2 Methods

The primary method used in this chapter is regression analysis to investigate the correlation between developers and pattern defects. To establish the model, both features and targets are required. For the features, the electron beam (EB) dose and designed pattern pitches were included. Additionally, features of the developers were also incorporated. The developer features were derived from the parameters of the stratified polymer dissolution model, a simulation framework developed to reproduce the frequency and impedance change charts measured by QCM. For the target in the regression analysis, SEM images were analyzed using the Hough transform method, as also described in Chapter 3.

SEM images of L/S patterns were used in this chapter [Fig. 4-1(a)]. The L/S ratio was 1:3, and the patterns were drawn using electron beams with an accelerating voltage of 150 kV and a probe current of 8.0 pA. The exposure doses ranged from 310 to 427 μC/cm².The SEM images were first processed using a Laplacian of Gaussian (LoG) filter to enhance edge detection [Fig. 4-1(b)]. Pixels corresponding to line edges were extracted to measure pattern defects and roughness. The filtered images were then analyzed using the Hough transform method established in Chapter 3. Each pixel of the line edges was transformed into a vote in Hough space. By accumulating these votes and fitting their distribution [Fig. 4-1(d)] with Gaussian-based function, the stochastically generated defects or roughness on the line patterns were quantified into a single value, which is the standard deviation of the Gaussian function fitting plane denoted as σ_{vote} [Fig. 4-1(e)]. This quantified value was subsequently used as the target variable in regression analysis to investigate the relationship between developer features and pattern defects.

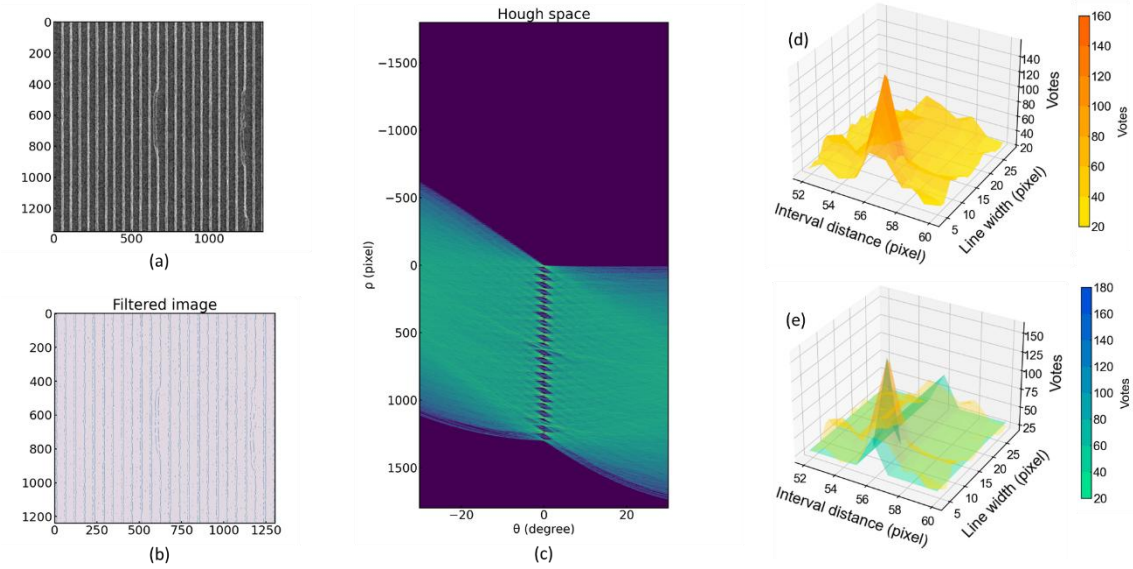

Figure 4-1 (a) SEM image of the L/S pattern. (b) Filtered SEM image obtained using a LoG filter. (c) Hough transform applied to (b) as input. (d) The orange-red plane illustrates the accumulation of votes in Hough space at $\theta = 0$, corresponding to the vertical direction of the filtered image. (e) The blue-green plane represents the fitting result.

For the simulation, polymer dissolution was modeled using SPDM established in chapter 2. The dynamics of the three components—polymer, water, and alkali—were simulated using the diffusion equation and the coordinate perpendicular to the QCM substrate surface. The calculation used a cell length of 5 nm.

The features and target variables described above were analyzed by the least squares and lasso regressions. 80% of the data was used for training and 20% of the data was used for testing. The error functions of least squares regression (E_{ls}), and lasso regression (E_{lasso}) are expressed in Eqs. (4-1) and (4-2), respectively

$$E_{\mathrm{ls}} = \sum_{n=1}^{N_{\mathrm{train}}} \left\{ y_{\mathrm{train},n} - f\left(x_{\mathrm{train},n}\right) \right\}^2 \tag{4-1}$$

$$E_{\mathrm{lasso}} = \sum_{n=1}^{N_{\mathrm{train}}} \left\{ y_{\mathrm{train},n} - f\left(x_{\mathrm{train},n}\right) \right\}^2 + \alpha \sum_{\mathrm{i}=1}^{m} |w_{\mathrm{i}}| \ , \tag{4-2}$$

where N_{train}, y_{train}, $x_{\mathrm{train,n}}$, and $f(x_{\mathrm{train,n}})$ are the number of training data, the n-th value of σ_{vote} used as a training data, the n-th variable set, and the value calculated

using the hypothesis function at the n-th variable set. The w_i are the feature weights included in the hypothesis function $f(x_{train,n})$ used as coefficients of terms composing the variable set. To suppress overfitting, the regularization term, are added to E_{ls} in Eq. (4-1). The hyperparameter α is used to adjust the weight of the Manhattan norm (l_1 norm) in Eq. (4-2). Normalization was used in this work to scale features. The feature values were scaled into new values using

$$X = \frac{x - x_{\min}}{x_{\max} - x_{\min}}, \tag{4-3}$$

where X, x, $x_{\min}$, and $x_{\max}$ are the scaled feature values, the original feature values, and the minimum and maximum values in the original feature values, respectively. The root mean square error (RMSE) was used as the evaluation function, which describes the distance between the predicted values and the target variables achieved from experiments. It is defined as

$$\mathrm{RMSE} = \sqrt{\frac{\sum_{n=1}^{N_{\mathrm{test}}}\{y_{\mathrm{test},n} - f(x_{\mathrm{test},n})\}^2}{N_{\mathrm{test}}}}, \tag{4-4}$$

where N_{test}, $y_{\mathrm{test},n}$, and $x_{\mathrm{test},n}$ are respectively the number of test data respectively the number of test data, the nth target variable (in this context, σ_{vote}) used as a test datum, and the nth explanatory variable set.

4.3 Results and discussion

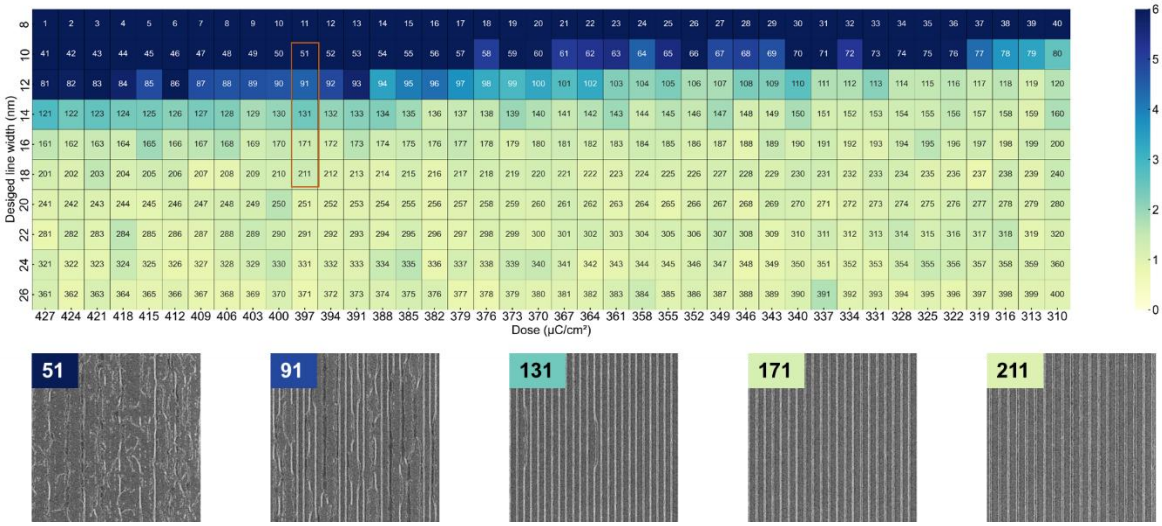

Figure 4-2 Images with varying exposure doses and designed line widths are labeled with numbers ranging from 1 to 400. The evaluation results are classified using color coding. Images with lower roughness (smaller σ_{vote}) are highlighted in lighter colors, while those with more severe defects are represented in darker colors. To validate the results, images numbered 51, 91, 131, 171, and 211 are displayed. Note that the σ_{vote} values presented in the table have been magnified by a factor of 200 from their original values.

The target variables (σ_{vote}) were obtained with the automatic evaluation of SEM images. The displayed SEM images present the capability of the evaluation. The magnified σ_{vote} of the images for the designed line width from 12 to 26 nm were used for the following regression analysis. This indicates that even SEM images with defects, such as image No. 91, can be utilized to provide valuable insights in discussions about the correlation between developers and patterns.

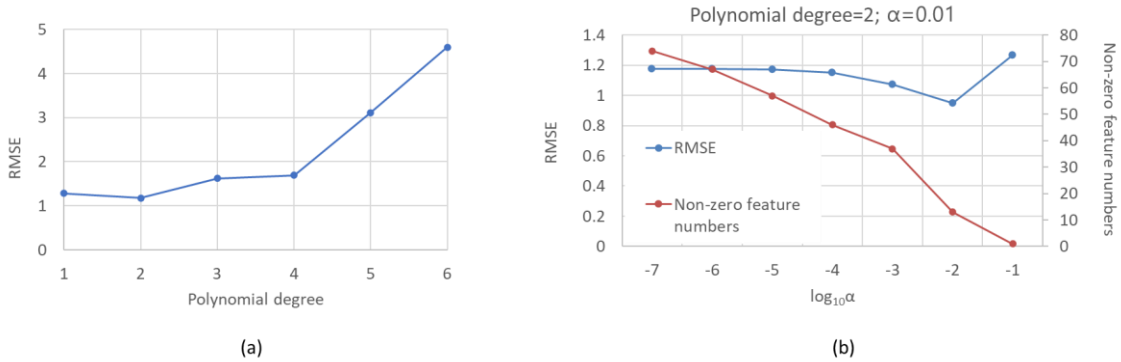

Figure 4-3 (a) RMSEs of validation set plotted against polynomial degree. (b) Dependences of the number of feature values and RMSE of validation set on hyperparameter α of lasso regression.

In the least squares regression, RMSEs of the training set at the 2nd polynomial degree were smallest, which was 1.176. Therefore, the 2nd polynomial degree was the most proper for the model. Based on these results, the regularization term was α added, which means the lasso regression model was tested. The difference in RMSE decreased when α decreased. On the other hand, the number of feature values increased while α decreased. To maintain a low RMSE and have fewer features at the same time, 10-2 was selected to be the best α value and the number of polynomial features was 13.

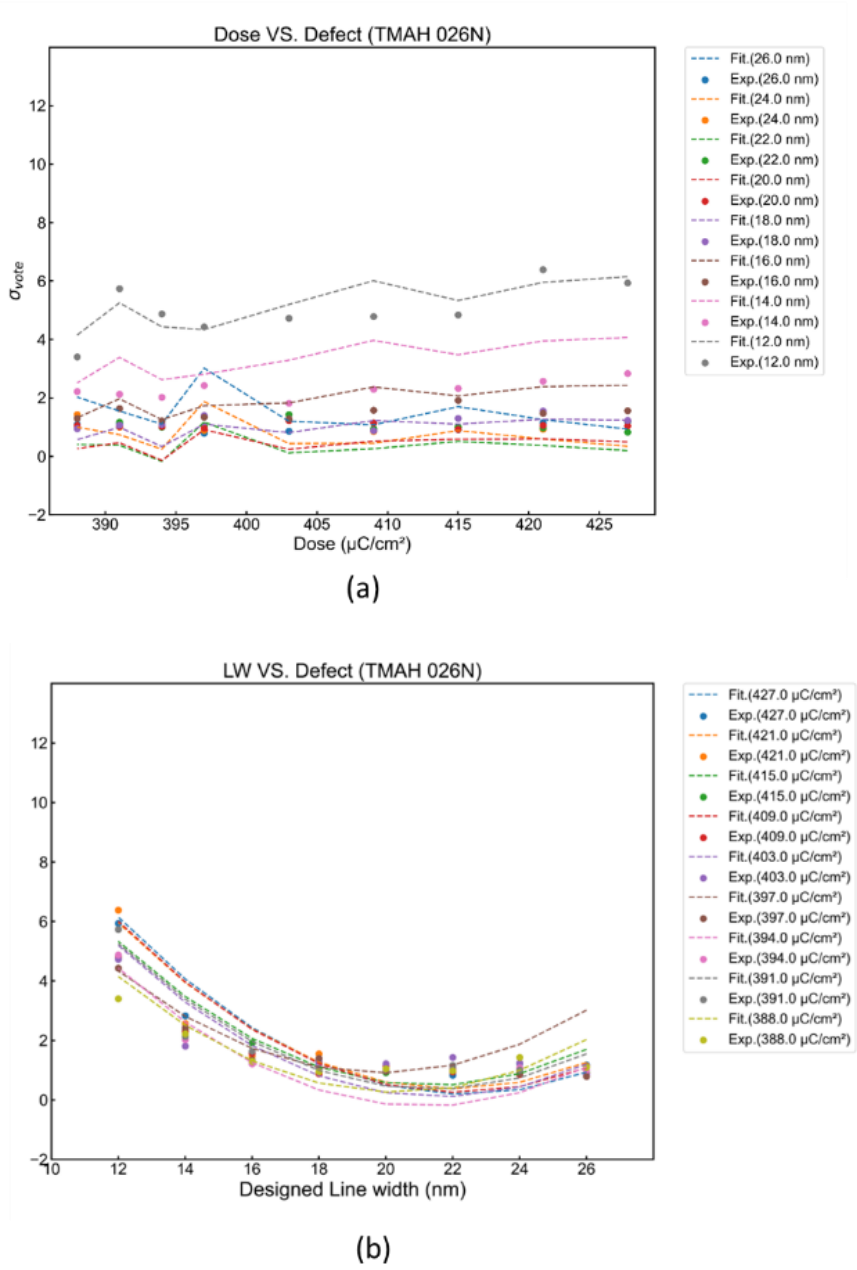

Figure 4-4 The fitting results of the lasso model. The experimental results and the predicted values are plotted in dots and dash lines, respectively. (a) σ_{vote} was plotted against the exposure dose. Different colors represent different designed line widths. (b) σ_{vote} was plotted against the designed line widths. Different colors represent different exposure dose.

The lasso regression model, demonstrated in Fig. 4-4, highlights the model's ability to account for defects. Further analysis revealed that the most influential features in the model were line width and dose. In terms of developer characteristics, the most significant factors were the extent to which residual polymers affected the dissolution rate and the speed at which the resist near the substrate.

4.4 Conclusion

This practical application introduces a novel quantitative method to explore the correlation between developers and resist patterns. The simulation of dissolution kinetics generates the feature variables, describing developers not through traditional chemical properties but by capturing the mutual interaction between the solute resist and the solvent developer.

Additionally, the evaluation of SEM images using the Hough transform method allows the inclusion of severely defected resist patterns in the analysis. To investigate the relationship between the feature and target variables, regression analysis was employed. This approach identified key parameters that could significantly influence the generation of defects.

Concluding Remarks

This doctoral dissertation presents a data-driven approach to investigate chemically amplified resists (CARs) and their compatible developers used in the lithography process. Machine learning serves as a powerful tool to analyze the correlations between material/process parameters and performance metrics. Accordingly, key variables related to materials and processes were systematically extracted and analyzed.

The lithographic process involving CARs includes spin coating, post-applied baking (PAB), exposure, post-exposure baking (PEB), and development. The resulting resist patterns were inspected using scanning electron microscopy (SEM). This study focused on analyzing PEB and development process parameters, as well as employing image recognition techniques on SEM inspection results.

Chapter 1 explores the effective reaction radius (R_p) of the deprotection reaction, a critical material descriptor that influences PEB time and line-edge roughness (LER) formation. A methodology was developed to estimate material parameters for CARs. The R_p of poly(4-hydroxystyrene) (PHS) with 54.6 mol% tert-butoxycarbonyl (*t*-Boc) protection was estimated using both experimental and simulation data. In addition, the dissolution threshold (C_{th}) for 2.38 wt% tetramethylammonium hydroxide (TMAH) developer was determined. Electron beam (EB) resist patterns under different HPs and doses conditions were fabricated and analyzed using image processing techniques. The acid reaction-diffusion model was employed to correlate the simulation results with experimental results, yielding an estimated R_p of 0.05–0.08 nm and an C_{th} of approximately 1.3–1.6 nm^{-3}. Bayesian optimization (BO) was conducted to decrease the iteration number.

Chapter 2 introduces the Stratified Polymer Dissolution Model (SPDM), a diffusion-based model that successfully replicated quartz crystal microbalance (QCM) data and provided physically meaningful descriptors for machine learning. The model captures the layered dissolution kinetics, showing that variation in the mass loss profile leads to significant differences in local viscosity near the dissolution front. This insight is critical to understanding developer–resist interactions. SPDM also quantifies key dissolution characteristics of various polymers and developers, enhancing the physical interpretability of the process. Experimental observations using dynamic light scattering (DLS) further identified

hydrodynamic radius (R_H) of the polymers at static state, offering insights into polymer dissolution kinetics.

Chapter 3 proposes a novel pattern analysis method using the Hough transform. Unlike conventional approaches that measure individual lines, this method enables automatic quantification of entire line-and-space (L/S) resist patterns. Defectivity indices of those severe defected patterns can also be extracted systematically. These evaluation metrics can then be used as target outputs for simulation model refinement and machine learning analysis to identify chemical factors affecting pattern fidelity. Another ML model, hierarchical classification was also tried to classify the line pattern and space pattern in an L/S pattern. This method is applicable for clear patterns with few defects.

Finally, the practical application demonstrated how the correlation was analyzed with ML method, regression analysis of correlation between different developers and final patterns. Note that the model is still under adjustment based on the new insights of the lithographic processes and materials.

Acknowledgments

These studies were partially supported by a Grant-in-Aid for JSPS Fellows (JSPS KAKENHI Grant No. 23KJ1531).

I would like to express my sincere gratitude to Tokyo Electron Kyushu Limited, Hitachi High-Tech Corporation, and the Yagi Laboratory at SANKEN, the University of Osaka, for their generous support. I also wish to thank the staff of the Honors Programs for Graduate Schools at the University of Osaka, whose efforts have made these valuable collaborations possible.

I sincerely express my heartfelt gratitude to my mentor, Professor Takahiro Kozawa, for his continuous guidance of my research and being generous with his time in teaching me not only academic knowledge including mathematics, physics, chemistry, computer science, etc., but also planning skills in doing research.

I am deeply grateful to Professor Shinya Furukawa and Professor Daisuke Kan for their insightful guidance and valuable contributions to my doctoral dissertation.

I would like to extend my gratitude to Assoc. Prof. Yusa Muroya for teaching me radiation knowledge and how to encode a simulation model. He also helped me out when I met trouble with my email system. I would like to extend my gratitude to SA Assoc. Prof. Eichi Nomura for his support in experiments and advice. He taught me a lot about scanning electron microscope. I would like to extend my gratitude to Asst. Prof. Kadzumasa Okamoto, who provided plenty of help in maintaining EUV exposure devices and shared his interest in animation. I would like to extend my gratitude to SA researcher Mr. Akihiro Konda for his plenty of help in teaching me experiments and the use of devices.

I deeply appreciate the secretary in Kozawa lab., Ms. Kinuko Watanabe, without her plenty of help, I could not work in a swift manner.

I would like to express my sincere appreciation to the doctoral students from industry for their support and encouragement. I am grateful to Dr. Satoshi Enomoto for guiding me on a tour of the Lawrence Berkeley National Laboratory. My thanks go to Dr. Masahiko Harumoto as well, for generously sharing their academic experience and recommending excellent restaurants during my stay in

California, US. I would also like to thank Dr. Yuko Tsutsui Ito for her valuable advice during my presentation discussions.

I gratefully acknowledge the graduate students, Mr. Kazuki Azumagawa and Mr. Kengo Ikeuchi for their help. Especially, Mr. Azumagawa taught me machine learning knowledge and Python language from the beginning of my research. Without his help, I could not publish papers fast. I would like to acknowledge my appreciation to my fellow researchers: Ms. Tomoe Otsuka, Mr. Naoki Tanaka, Ms. Hitomi Betsumiya and Ms. Yui Takata for the days we worked hard and the days we had fun together. Moreover, it was a great pleasure to publish papers together with Ms. Otsuka, Mr. Tanaka and Ms. Betsumiya. I wish all the best for their future career.

I would like to thank other students in Kozawa laboratory, Mr. Yutaro Iwashige, Mr. Jiahao Wang, Mr. Soichiro Nishimoto, Ms. Yoshika Tsuda, Mr. Kohei Hashimoto, Mr. Hikaru Kaneba, Mr. Shotaro Fuku, Mr. Takehiro Masuda, Ms. Sayaka Oshitani and Mr. Kihiro Furukawa for their help in running the laboratory, research and daily life.

I appreciate all my friends in the University of Osaka for their support and understanding, especially Ms. Yiling Xie. It was a great time playing board games, badminton and hiking together.

Last but not the least, I would like to thank my family for their constant devotion. Especially my father, Mr. Linan Jin, and my mother Ms. Beiyan Xu. I am proud of them.